Modelling the Propagation of Solar Energetic Particles Injected by a Shock-like Source using Test Particle Simulations

Adam Hutchinson

A thesis submitted in partial fulfilment
of the requirements for the degree of
Doctor of Philosophy

Jeremiah Horrocks Institute for Mathematics, Physics and Astronomy
University of Central Lancashire

June 2023

Declaration

Type of Award: Doctor of Philosophy

School: Natural Sciences

I declare that while registered as a candidate for the research degree, I have not been a registered candidate or enrolled student for another award of the University or other academic or professional institution.

I declare that no material contained in the thesis has been used in any other submission for an academic award and is solely my own work.

No proof-reading service was used in the compilation of this thesis.

Adam Hutchinson

June 2023

Abstract

Solar Energetic Particles (SEPs) are ions and electrons accelerated during flare and Coronal Mass Ejection (CME) events. SEP events increase the particle radiation that permeates the heliosphere and are harmful to spacecraft equipment as well as human health. For this reason, the study of energetic particle propagation is an area of vital importance in understanding the local radiation environment.

In this thesis we developed the first shock-like particle injection for a full-orbit test particle code and studied two distinct scenarios of SEP propagation. Firstly, we considered instantaneous injections of energetic protons at CME-driven shock heights. We modelled the particle back-precipitation to the solar surface to study whether protons injected from a CME shock can explain the γ-ray emission associated with Long Duration Gamma-Ray Flares (LDGRFs). We calculated precipitation fractions for each injection to determine the proportion of the injected population that could contribute to the γ-ray emission for a range of interplanetary scattering conditions (mean free path, $\lambda = 0.0025-1.0$ au). We estimated upper limits for the total precipitation fractions for eight LDGRF events and found that they were considerably smaller than the minimum requirements for back-precipitation from a CME-driven shock to be the dominant mechanism for γ-ray production during LDGRFs.

Secondly, we simulated a shock-like particle injection for a variety of injection functions to derive SEP intensity and anisotropy profiles at 1 au. It has been proposed by several studies that the long duration of SEP events at 1 au is due to temporally extended acceleration at an interplanetary shock. We compared SEP intensity profiles modelled from instantaneous and shock-like injections and found that the link between injection duration and event duration is very weak, unlike what is commonly assumed. In addition the variation of injection efficiency along the shock front was found to play a minor role in shaping intensity profiles for gradual SEP events. We modelled SEP propagation with and without including the effects of corotation, considering the shock-like injection and found that corotation plays a dominant role in the decay phase of SEP events. Corotation reduces the decay time constant, τ, significantly for both eastern and western events and it makes τ's dependence on the mean free path λ negligible, in contrast to results from 1D focussed transport models. The work presented in this thesis provides useful steps to model radiation within the inner heliosphere more accurately.

Contents

Acknowledgements

There have been many people who throughout the PhD have helped me either academically or otherwise.

I'd like to say a huge thank you to my supervisor, Silvia Dalla for her continued guidance and support and for pushing me (at times quite far) outside of my comfort zone. Silvia was the first lecturer I met when I started university and since then I have worked with her for both undergraduate projects and now the PhD. Throughout the ~ 5 years working together she has been amazing and has always been available to talk whenever I have had questions or needed guidance. I am sure I have been the cause of many empty green pens, and asked far too many questions, but I can say that it has been a pleasure to work together!

I would like to thank my second supervisor Timo Laitinen. Timo has been a huge help from useful discussions and providing feedback on the work, to enabling access to the Dirac HPC, to just being a friendly face. His input and assistance have been invaluable.

I am grateful to Charlotte Waterfall for her feedback on the papers as well as the other people of the Solar group, including Bill Swalwell, for listening to me on the odd occasion waffle on about whatever I was working on at the time in our group meetings.

I would like to thank Georgia de Nolfo, Alessandro Bruno and Jim Ryan for their patience and feedback on my work and the conversations we have had over the past few years, which I have thoroughly enjoyed and learnt a lot from.

I would also like to thank Aimilia Smyrli for the conversations we had near the Acropolis in Athens and for continuing to be inspiring.

I want to give a huge thank you to my dear friends Callum MacKinnon and Jordan Cole, who have done nothing short of kept me sane throughout this process with plenty of complaining, ridiculous conversations, takeaway nights, as well as providing their office space as a getaway when needed. It has been the greatest pleasure to go through this journey with you two and I couldn't have done it without you guys.

I grateful to Adam Fenton for all the tips and tricks he's mentioned over the PhD (which I have almost certainly forgotten) and all the small conversations that would break up the day. It was certainly entertaining to find someone more "done with the world" than I am.

I'd also like to thank Tim Mercer, who I worked with running the first-year lab module for 2 years. I enjoyed this process greatly and it was at times a great distraction from PhD work. Tim gave many useful bits of advice and during the covid pandemic was living proof that I could be more tired and stressed than I was at any given moment.

A la perchoine!

List of Figures

List of Tables

Acronyms

CDF Cumulative Distribution Function.

CME Coronal Mass Injection.

GC Guiding Centre.

GCR Galactic Cosmic Rays.

GLE Ground Level Enhancement.

HCS Heliospheric Current Sheet.

ICDF Inverse Cumulative Distribution Function.

IMF Interplanetary Magnetic Field.

IP Interplanetary.

ITS Inverse Transform Sampling.

LDGRFs Long Duration Gamma-Ray Flares.

PDF Probability Distribution Function.

SEP Solar Energetic Particle.

Chapter 1

Introduction

This thesis focusses on Solar Energetic Particles (SEP) and their propagation through interplanetary (IP) space. Here we will define what SEPs are, how they propagate through the heliosphere and why it is important to study them. The aims of the work and structure of the thesis are presented.

1.1 Solar Energetic Particles

Solar Energetic Particles (SEPs) are energetic particles that are thought to be accelerated via solar flare associated processes (e.g. by electric fields during magnetic reconnection events, see Klein & Dalla 2017) and via acceleration at Coronal Mass Ejection (CME)-driven shocks (e.g. Cane et al. 1988; Reames et al. 1997; Desai & Giacalone 2016). SEPs are observed by spacecraft in interplanetary (IP) space over a wide energy range, e.g. from KeV to GeV per nucleon for ions (e.g. Lario et al. 1998; Bruno et al. 2018), and they consist of electrons, protons and heavier ions (e.g. Cohen et al. 2021; Dresing et al. 2022).

The most energetic SEPs ($E_{ion} > 1$ GeV/nuc) are responsible for Ground Level Enhancement (GLE) events (e.g. Shea & Smart 2012). During these events the effects of relativistic particles impacting the Earth's atmosphere are observed at Earth's surface by neutron monitors across the globe (e.g. Ryan et al. 2000; Shea & Smart 2012). The high energy population of particles accelerated during solar events are of interest, not only because they cause GLE events, but also because they are thought to contribute to other high energy emissions on the Sun, such as >100 MeV γ-rays (e.g. Ryan et al. 2000; Share et al. 2018).

SEPs provide information on acceleration and propagation processes at the Sun and in the heliosphere. They are of interest to study also because they can cause harm to our technology, to humans in space and aboard aircraft at high altitudes, and are responsible for the evolving radiation conditions in the local space environment (e.g. Marsh et al. 2015, and references therein). There have been concerns about how large solar eruptions that trigger geomagnetic storms can damage important infrastructure on the ground, like electrical transformers (e.g. Cid et al. 2014). There have been occasions where geomagnetic storms caused by solar eruptive events have led to damages to electrical networks. For instance a blackout was caused for around 50000 customers in Sweden in 2003 and the famous Quebec electrical disruption in 1989 caused a blackout that lasted 9 hours (Cid et al. 2014; Swalwell 2018). To mitigate the risks associated with space weather and to better predict the hazards of space radiation studying SEP transport is vitally important, especially for developing accurate SEP forecasting models (e.g. Marsh et al. 2015).

1.2 Solar Energetic Particle Propagation

One approach to classifying and interpreting SEP events is the dual-class paradigm of "Gradual" and "Impulsive" events (e.g. Reames 1999), where particles are thought to be accelerated at a CME-driven shock in the corona and IP space or at the Sun during solar flares respectively.

Solar flares are localised enhancements in solar radiation across the entire electromagnetic spectrum. During these events particles can be accelerated to high energies and generate electromagnetic radiation. Some of the particles may escape the solar atmosphere and propagate along open magnetic field lines of IP space.

CMEs are eruptive events on the Sun where material is ejected when a flux rope in the corona becomes unstable. Typically, CMEs are closely associated with solar flares, especially for the most intense events.

CMEs vary in speed from a few hundred kilometres per second to very fast CMEs of nearly 3000 km/s (e.g. Reames et al. 1997; Winter et al. 2018). CMEs drive IP shocks where particle acceleration can take place (e.g. Reames et al. 1997; Desai & Giacalone 2016). Particles accelerated via this method can eventually escape the shock front and propagate in a similar way to flare accelerated populations. Particles accelerated at the shock have the possibility to propagate sunward and may even reach the solar surface.

Once the particles are accelerated/injected they will propagate out into the solar system and may be detected at near-Earth spacecraft at 1 au. Whether SEPs originate on the Sun or in the corona/IP space at CME-driven shocks, particles of the same species and energy will propagate in the same way (in the same magnetic conditions), although their origin may lead to different intensity profiles. Charged particles are guided by the Interplanetary Magnetic Field (IMF), gyrating around magnetic field lines, forming helical trajectories with the centre of gyration called the Guiding Centre (GC). In reality propagation effects such as drifts (Dalla et al. 2013) will lead to the motion of particle's GC away from the initial magnetic field line. Hence, SEP intensity profiles measured by spacecraft are a combination of effects: firstly the mechanism by which the SEPs are accelerated/injected (flare or CME-driven shock) and also by propagation effects that depend on the position and velocities of the particles. Figure 1.1 summarise the differences between events from CME-driven shock origin (so called gradual events) and from flare origin (so called impulsive events) according to the dual-class paradigm. As can be seen in Figure 1.1 the cyan helical trajectories of the particles are the same regardless of particle acceleration mechanism.

1.3 Long Duration Gamma-Ray Flares

Typically, during solar flares γ-ray emission is short-lived, usually lasting 10-100 seconds. However, during Long Duration Gamma-Ray Flares (LDGRFs) γ-ray emission lasts far beyond the impulsive phase of the flare, making typical explanations for their origin based on flare acceleration arguments, no longer sufficient (Pesce-Rollins et al. 2022). During these events γ-rays are produced for hours, up to $\sim$ 20 hours in the longest events (e.g. Winter et al. 2018).

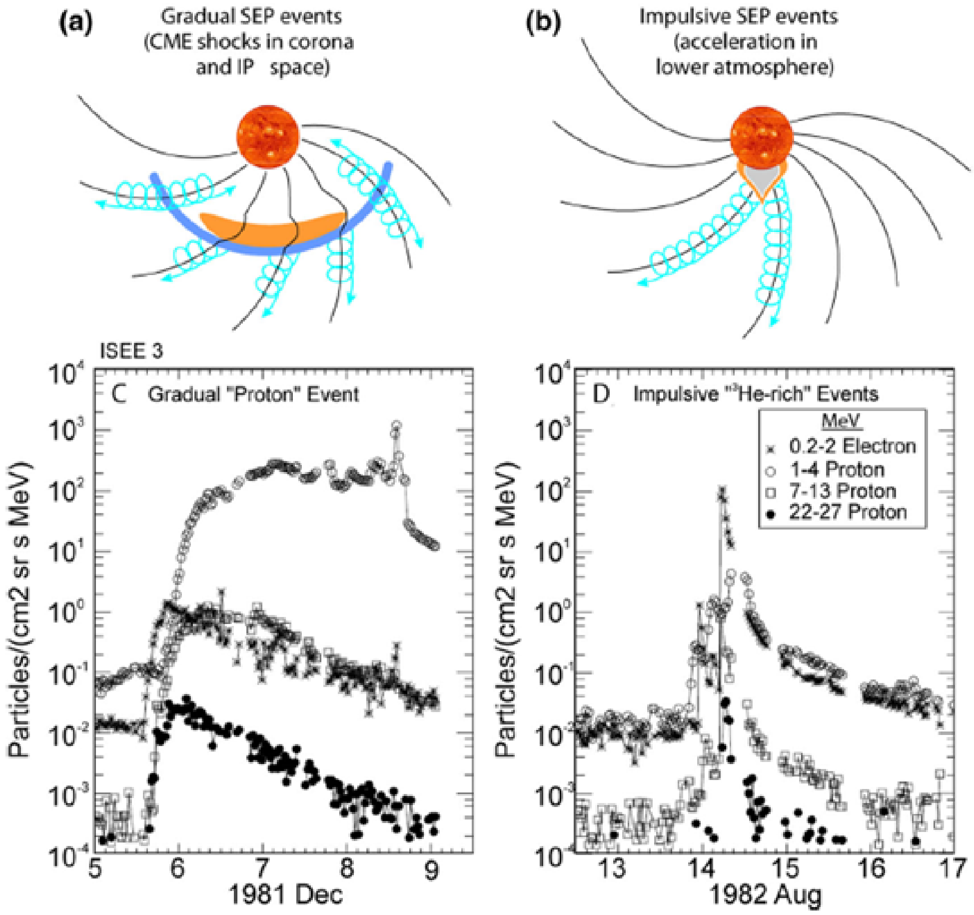

Figure 1.1: Schematics showing the dual class paradigm of so-called gradual (a) and impulsive (b) SEP events. Panels (c) and (d) show intensity profiles of typical gradual and impulsive events respectively. In panel (a) the orange shaded region is the CME-ejecta and the bold blue line denotes the CME-driven shock front. The cyan spiral lines represent particle trajectories along the magnetic field lines shown in black. [Image credit: Desai & Giacalone (2016)]

Two main hypotheses have been proposed to explain the production of prolonged γ-ray emission during LDGRFs. One of these is that high energy protons that are accelerated at a CME-driven shock back-propagate to the solar surface over extended times to produce the γ-ray emission (e.g. Share et al. 2018), a scenario that will be referenced to in the following as the CME-shock scenario for LDGRFs.

1.4 Corotation

The solar magnetic field extends out into the heliosphere within the solar wind. Due to the “frozen-in theorem” the magnetic field footpoint remains fixed on the solar surface. As the Sun rotates it winds up the IMF into an Archimedean spiral structure on average (the Parker spiral, e.g. Parker 1958). As the Sun rotates magnetic flux tubes rooted at the Sun co-rotate with it. This process is known as the corotation of magnetic flux tubes.

1.5 Full-orbit test particle simulations

To study SEP propagation we use 3D full-orbit test particle simulations throughout the work conducted over the PhD. These simulations follow individual “test particles” that are assumed to propagate into the heliosphere, unaffected by other particles, guided by the magnetic field. Here “full-orbit” refers to the fact that we model the full helical motion of the SEPs rather than focussing on just the GC position of the particle. These simulations allow us to trace exactly where the particles propagate to and test the aims detailed in the next section.

1.6 Aims/Objectives

The work conducted over the PhD investigates SEP propagation scenarios involving CME-driven shocks to better understand the spatial patterns and evolution of SEP radiation in the inner heliosphere.

In this thesis 3D full-orbit test particle simulations are used to study 1) SEPs propagating towards the Sun and 2) SEPs propagating outwards away from the Sun. In the first phase of the PhD, SEP propagation from CME-driven shock heights is modelled and particle numbers returning to the photosphere are recorded. The latter analysis aims to provide constraints on energetic proton back-precipitation, which has been suggested as the main contribution to generating gamma-rays during LDGRF events within the CME-shock scenario. Secondly, a new temporally extended shock-like injection for our test particle code is developed and we focus on the effects of this shock-like injection on intensity and anisotropy profiles at 0.3 and 1.0 au.

The main aims of the work are:

1. To model energetic proton back-precipitation onto the solar atmosphere over extended times from CME shock heights. Then comment on the validity of the CME-shock scenario in the production of sustained γ-ray emission during LDGRFs.

2. To develop a temporally and spatially extended particle injection for the full-orbit test particle code and investigate how altering shock/injection parameters affects time-intensity and anisotropy profiles for observers at 0.3 and 1.0 au.

3. To investigate the role of corotation on intensity profiles for an extended shock-like injection, and any implications on east-west asymmetries in the intensity profiles.

The comparison of 0.3 au and 1 au profiles is particularly timely given the new SEP measurements by *Solar Orbiter* and *Parker Solar Probe*.

1.7 Structure of the thesis

In chapter 2 we provide a background to SEPs, their sources, models of their propagation and outline key details of the scenarios we investigated in the results chapters. In chapter 3 we focus on the role of CME-driven shocks as sources of SEPs, describe models of CME-sources and outline the role of CMEs in LDGRFs. In chapter 4 we describe the full-orbit test particle code and mention key features added over the PhD (such as the development of a temporally-extended shock-like injection). We discuss the results obtained for the investigation into the CME-shock acceleration scenario for producing γ-rays during LDGRFs in chapter 5. In chapter 6 we present intensity and anisotropy profiles at 0.3 and 1.0 au, considering different CME-shock parameters. In chapter 7 we discuss the effects of considering/neglecting corotation on intensity profiles at 1.0 au. Finally, in chapter 8 we provide the conclusions obtained from this work and discuss the implications of our results to the wider scientific community.

Chapter 2

Solar energetic particles and associated phenomena

In the previous chapter we introduced SEPs and why it useful to study their propagation through IP space. In this chapter we focus on providing a background to SEPs, their sources, and models of their propagation. We also give a background to LDGRFs.

2.1 SEP sources

SEP events are enhancements in energetic ions and electrons in the IP medium, observed in association with solar flares and CMEs. These events have been split into two classes, "gradual" and "impulsive", where particle acceleration is thought to dominantly occur at a CME-driven shock for the former, and in a solar flare for the latter (e.g. Desai & Giacalone 2016; Reames et al. 1996; Reames et al. 1997; Klein & Dalla 2017).

A distinction between impulsive and gradual SEP events was noted in the elemental abundances. During impulsive events substantial increases in ^{3}He/^{4}He and Fe/O occurred, implying different particle acceleration mechanisms compared to gradual ones (Reames et al. 1996; Reames 1999). On the other hand gradual events were not found to be ^{3}He or heavy ion rich and to have a composition similar to the solar wind.

Gradual events are often found to have a long duration (e.g. several days) and wide longitudinal extents in the heliosphere (e.g. $> 80°$), as evidenced by multi-spacecraft observations (e.g. Desai & Giacalone 2016, and references therein. See Figure 1.1). On the other hand, impulsive events have shorter durations and were initially thought to extend to a narrow range of longitudes.

2.1.1 Impulsive events and solar flares

Type III radio bursts are generated by electrons streaming along open magnetic field lines. These electron populations are clearly associated with flare acceleration, typically by the hard X-ray emission present at the footpoints of the flare loop on the solar disc. A schematic showing this is visible in Figure 2.1 as well as other characteristic flare emissions (Klein & Dalla 2017). Coupled with the fact that impulsive (so-called Helium-rich) events were observed by spacecraft with good magnetic connection to the AR, had large electron intensities, and associated Type III radio emission, these impulsive event populations are considered to originate at the flare site (Reames et al. 1996, and references therein).

Although no particle acceleration was modelled in the work in this thesis, it is useful to briefly mention the mechanisms that can produce SEPs during flares. There are a number of possible particle acceleration mechanisms during flares. These include direct electric field acceleration (Dalla & Browning 2005), acceleration due to collapsing magnetic traps (Somov & Bogachev 2003; Giuliani et al. 2005; Grady & Neukirch 2009) and stochastic acceleration (Miller 1998).

While SEPs observed over large longitudinal ranges were initially associated with gradual SEP events, it has been shown that impulsive events can also span large longitudinal extents (Wiedenbeck et al. 2013). Gómez-Herrero et al. (2015) in their study of the 3rd November 2011 SEP event provided alternatives to SEP acceleration at a CME-driven shock for explaining the large longitudinal extent of these multi-spacecraft SEP events. These included longitudinal transport in the corona, cross-field transport in IP space, and deviations from the ideal Parker spiral IMF structure. The exact mechanism that allows SEP populations to span large longitudinal extents during impulsive events is still a topic for debate and, as highlighted by Gómez-Herrero et al. (2015), can be due to one or combinations of many different mechanisms.

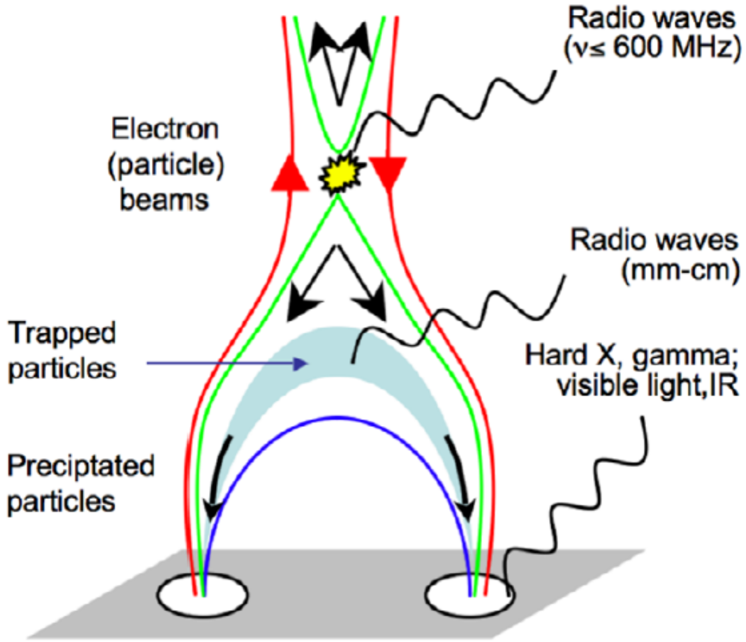

Figure 2.1: Schematic diagram of particle populations and related emissions during a flare [Image credit: Klein & Dalla (2017)].

2.1.2 Gradual events and CMEs

During large gradual SEP events, particle acceleration is thought to occur at CME-driven shock fronts as they propagate throughout the corona and IP space (e.g. Reames 1999; Desai & Giacalone 2016, see Figure 1.1). The characteristic long duration decays measured by spacecraft at 1 au are assumed to arise from acceleration at the shock that is extended in time (Cane 1988; Reames et al. 1997; Desai & Giacalone 2016). Possible mechanisms for SEP acceleration at CME-driven shocks include shock drift acceleration and diffusive shock acceleration (Kallenrode 2003; Meyer-Vernet 2007; Klein & Dalla 2017).

One observed feature of SEP intensity profiles is the characteristic ordering by longitude of the observer's magnetic footpoint relative to the associated AR. This is shown in Figure 2.2 displaying intensity profiles for four observers with different longitudinal connection to the source AR (Figure 15 from Cane et al. 1988). Eastern

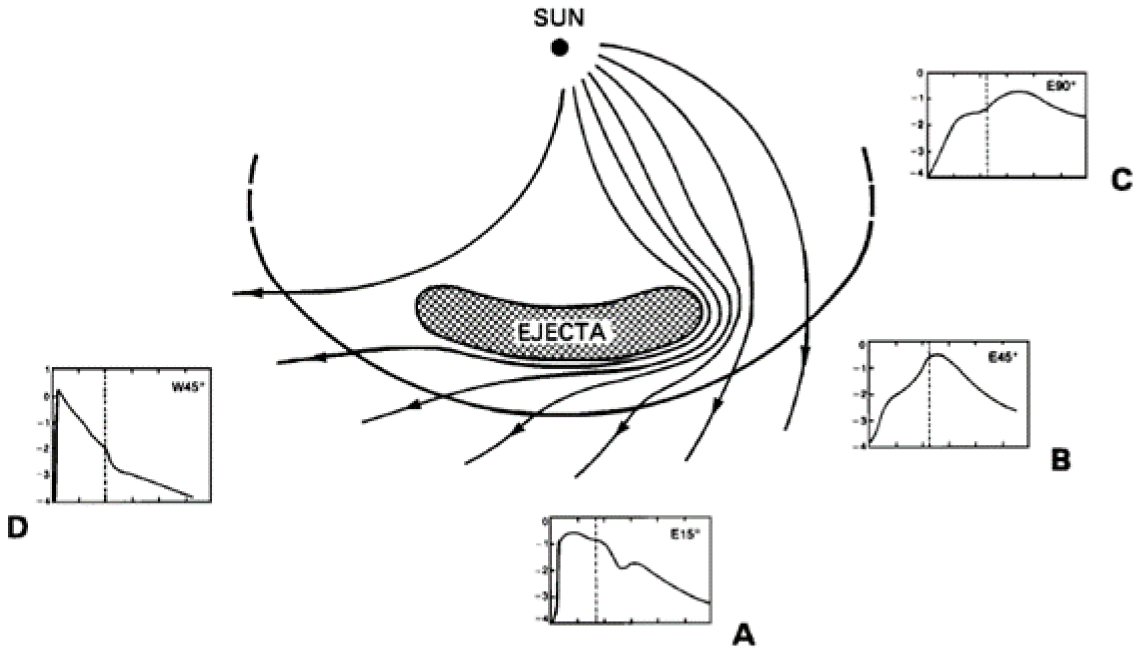

Figure 2.2: Intensity profiles for observers with different longitudinal connections to the shock source. Solid black lines with arrows represent magnetic field lines that wrap around the CME-ejecta (hashed section). [Image credit: Cane et al. (1988)]

events with respect to the observer have slow, prolonged rise times to peak intensity (observers B and C), whereas western events with respect to the observer have a much more rapid rise to peak intensity (observer A). Cane et al. (1988) analysed intensity profiles for 235 SEP events and interpreted this in terms of magnetic connection to different portions of a CME-driven shock. The authors highlight that magnetic connection to the shock for long periods of time, even after the shock has propagated beyond 1 au, could explain the long duration of the SEP event.

2.2 SEP propagation

2.2.1 Interplanetary magnetic field

The IMF guides SEPs as they propagate in IP space. On average the IMF is thought to have an Archimedian spiral structure known as the Parker spiral. This can be seen in Figure 2.3, where the shape of the Parker spiral IMF is given by,

$$\phi - \phi_0 = \frac{\Omega(r - r_0)}{v_{sw}} \tag{2.1}$$

where r is radial distance in a heliocentric coordinate system, r_0 is the radial distance where the solar wind flow becomes radial, Ω is the sidereal solar rotation rate, ϕ is heliographic longitude, ϕ_0 is the longitude at r_0, and v_{sw} is the solar wind speed. Note that this equation is only valid in the equatorial plane.

The Parker spiral magnetic field lines guide the propagation of SEPs away from the Sun. In addition, the IMF is turbulent and particle trajectories are altered by the interaction with the turbulence. There are two ways in which particles are influenced by the interactions with magnetic turbulence: parallel scattering (also known as pitch angle scattering) and perpendicular transport.

As a result of the interaction with turbulent structures the particle's trajectory can be altered. This process can be described as pitch angle scattering, responsible for changes in the pitch angle (the angle between the particle's velocity vector and the magnetic field direction) of the particle and primarily affects how quickly particles propagate parallel to the magnetic field lines.

Perpendicular transport occurs as magnetic turbulence causes the IMF lines to deviate from the nominal Parker spiral through a process known as magnetic field line meandering (e.g. Laitinen et al. 2016). This results in perceived motion of the particles perpendicular to the average IMF and is considered as one contributor to the perpendicular transport of SEPs. The effects of magnetic turbulence can be

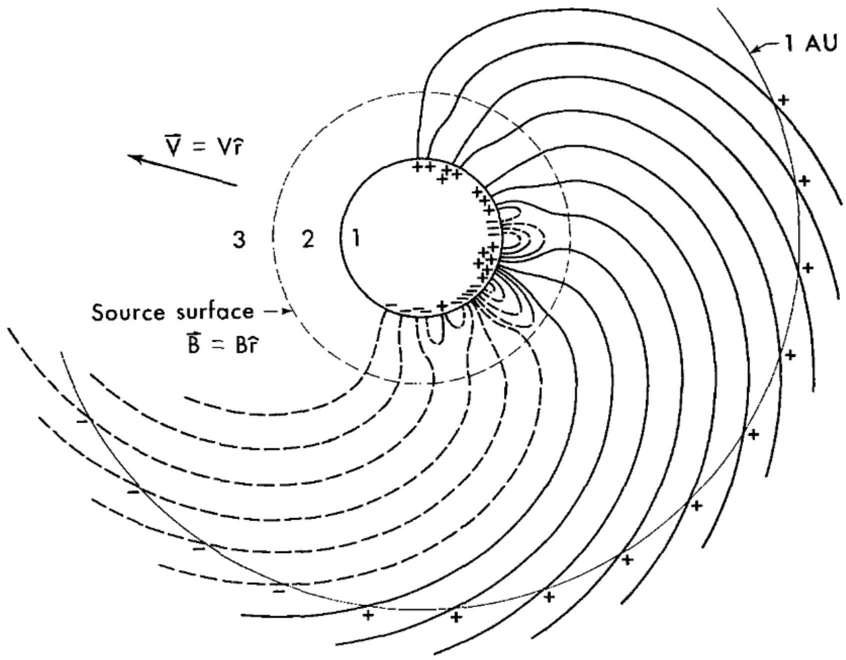

Figure 2.3: The Parker spiral IMF. Within the dashed line representing the source surface the magnetic field is a more complicated structure consisting of open field and closed loops in the corona and a "canopy" near the photosphere (Seckel et al. 1991, 1992) [Image credit: Schatten et al. (1969)].

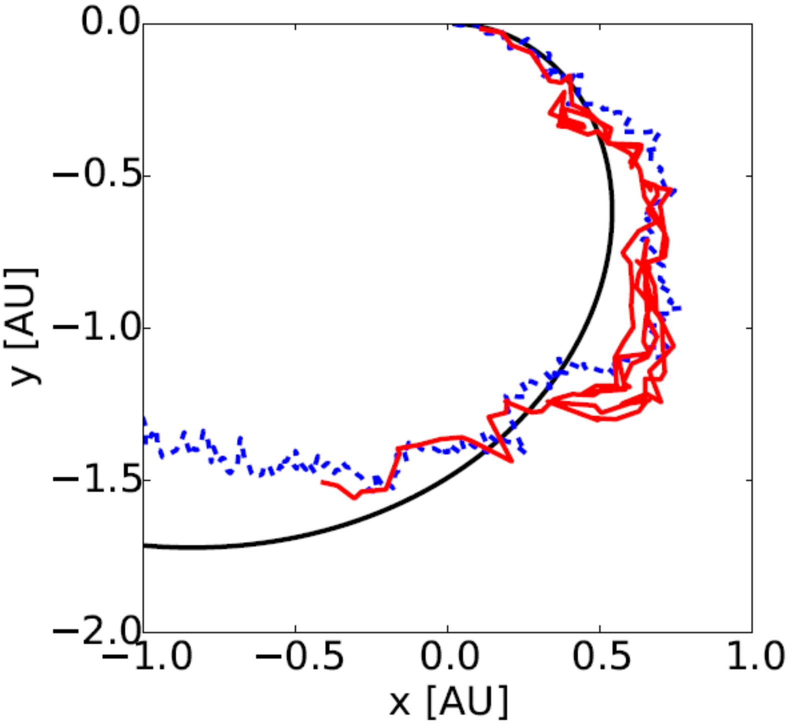

Figure 2.4: Modelled trajectory of a 10 MeV proton injected at the origin (red line). The black solid line is the Parker spiral IMF and the blue dashed line represents the meandering field due to magnetic turbulence. [Image credit: Laitinen et al. (2016)]

seen in Figure 2.4, where a modelled proton trajectory (shown in red) deviates from the nominal Parker spiral (black curve) due to field line meandering, where the blue dashed curved shows an IMF magnetic field line that includes the effects of magnetic turbulence (Laitinen et al. 2016).

2.2.2 Adiabatic deceleration

Adiabatic deceleration occurs as SEPs propagate outwards with the expanding solar wind (e.g. Dalla et al. 2015). Over time, particle-turbulence interactions occur which can be described as scattering off scattering centres that propagate outward. In some collisions an energy gain results and in some energy loss, but overall due to the expansion of the solar wind the net effect is an energy loss.

This process is analogous to what happens in an expanding ideal gas, leading to a temperature decrease. Whereas with an ideal gas thermal energy losses occur due to particle-particle interactions, here thermal energy is dissipated due to particle-turbulence interactions.

Particles detected by a spacecraft in a given energy band could have originally been injected at larger energies and decelerated due to adiabatic deceleration (Mason et al. 2012).

2.2.3 Models of SEP propagation

There are many approaches to modelling SEP propagation. A common approach is kinetic modelling where partial differential equations are solved to determine f, the distribution function of the SEPs (e.g. Lario et al. 1998; Wang et al. 2012; Kocharov et al. 2015; Afanasiev et al. 2018). The effects of magnetic turbulence have been modelled as diffusion of the SEP population both in terms of spatial location and particle velocities, relating to perpendicular and pitch angle scattering (e.g. Wang et al. 2012). These models consider parallel and perpendicular diffusion coefficients which alter the strength of the parallel and perpendicular scattering in the model. Generally, SEP transport equations include a focussing term, a term describing convection with the solar wind, diffusion terms, a source term, and in some cases a term describing adiabatic deceleration.

Traditionally, SEP propagation has been modelled using 1D focussed transport models, where particles are tied to and propagate along the IMF lines they are initially injected on (e.g. Bieber et al. 1994; Kallenrode & Wibberenz 1997). Particles that start, for example, with a pitch angle close to 90° near the Sun will become increasingly more field aligned (pitch angle approaching 0° for an antisunward IMF direction) due to focussing that results from particles propagating outward through

IP space where the magnetic field strength decreases as $1/r^2$. The focussing arises due to the magnetic moment of the particles remaining an adiabatic invariant and similarly causes particles propagating sunward into regions of increasing magnetic field strength to be reflected (a process called magnetic mirroring, e.g. Kallenrode 2003; Klein et al. 2018). The focussing term describes the evolution of the particle's pitch angle as a function of the distance along the magnetic field line. However in many cases focussed transport equations do not account for particle motion perpendicular to the magnetic field either from turbulence (Laitinen et al. 2016) or from other effects intrinsic to the system such as drift effects (Dalla et al. 2013).

Alternative to focussed transport models, full-orbit test particle simulations of SEP propagation calculate individual particle trajectories throughout the heliosphere by solving the particle's equation of motion. These types of simulations are intrinsically 3D. Previously, they have been used to study propagation through the IMF for the case of instantaneous particle injections close to the Sun (e.g. Marsh et al. 2015; Battarbee et al. 2018; Dalla et al. 2020; Waterfall et al. 2022). These simulations have included drift motions of the particles and more complex IP structures such as the Heliospheric Current Sheet (HCS) (e.g. Dalla et al. 2013; Battarbee et al. 2018; Waterfall et al. 2022).

2.3 Long duration gamma-ray flares

During solar flares, sudden increases in radiation in a variety of wavelengths are detected. The production of solar γ-rays over extended durations, including times when flare emission in other wavelengths is no longer present, has been observed for decades during events called LDGRFs (Ryan 2000, and references therein). In recent years, however, new data at photon energies > 100 MeV from the *Fermi* Large Area Telescope (LAT) have shown that these LDGRFs are not as rare as previously thought, reigniting debate over their origin (Ajello et al. 2014; Pesce-Rollins et al.

2015; Ackermann et al. 2017; Kahler et al. 2018; Klein et al. 2018; Omodei et al. 2018; Share et al. 2018; de Nolfo et al. 2019, and references therein). In these events, γ-rays are thought to be generated when >300 MeV protons and >200 MeV/nuc α particles collide with plasma near the solar surface (1 $R_\odot$) to produce neutral pions that subsequently decay to γ-rays (e.g. Share et al. 2018, and references therein).

The detection of LDGRFs implies that highly energetic protons and α particles strike the photosphere over extended time periods, of the order of hours and up to about 20 hours. A number of possible theories have been put forward to explain the phenomenon. The main two are: a) trapping of flare-accelerated ions within large coronal loops, with the possibility of time-extended acceleration within them (Mandzhavidze & Ramaty 1992; Ryan & Lee 1991), and b) time-extended acceleration at a propagating CME-driven shock followed by back-precipitation onto the solar atmosphere (Cliver et al. 1993). It is worth noting that the spatial resolution of current equipment (such as the LAT) is not good enough to discern whether γ-ray emission takes place in a compact region or whether it is spatially extended (Pesce-Rollins et al. 2022). The detection of γ-rays from "behind-the-limb" events (such as the 1st September 2014 event, see Jin et al. 2018), where the flaring AR is behind the visible disc of the Sun, appears to imply that the γ-ray emission region is very large or occurs at large altitudes in the corona (Pesce-Rollins et al. 2022). However, coronal densities are not sufficient for neutral pion production.

An ongoing problem for the scenario where a flare-accelerated population become trapped in large scale coronal loops is that the conditions for such a trapping process to sustain the release of particles to the photosphere for the timescales of LDGRFs are unclear (Pesce-Rollins et al. 2022). Some studies have argued that flare acceleration over long timescales is not the source mechanism of LDGRFs. For instance, Kahler et al. (2018) used observations of the reconnection rates of flare ribbons and determined that the reconnection episodes do not take place long enough to explain the time-extended γ-ray emission. Klein et al. (2018) have shown that typical signatures of flare acceleration are not present over long durations in these events. At present, the generally favoured mechanism within the scientific community for γ-ray production during LDGRFs is acceleration at a CME-driven shock followed by particle back-precipitation onto the solar atmosphere. In the following we will refer to it as the CME scenario for LDGRFs. In chapter 5 test particle simulations will be used to investigate this scenario.

2.4 Corotation and its effect on impulsive SEP events

As the IMF corotates with Sun there is a systematic westward motion of the IMF lines (in the solar rotation direction), which guide SEP propagation. A number of studies have commented on the effects of corotation for instantaneous particle injection at the Sun (Dröge et al. 2010; Giacalone & Jokipii 2012; Marsh et al. 2015).

Dröge et al. (2010) simulated impulsive SEP events by considering an instantaneous particle injection from a small solar region. They considered SEP propagation described by a focussed transport equation that includes adiabatic motion of SEPs parallel to the mean magnetic field direction and pitch angle scattering due to the magnetic turbulence. They computed the spatial distributions of ~ 100 keV electrons and 4 MeV protons and determined intensity-time profiles, considering different types of scattering conditions. Importantly for the work presented in this thesis, Dröge et al. (2010) consider how the intensity profiles are impacted by corotation (for an instantaneous injection near the Sun). As can be seen in Figure 2.5 (their Figure 8) for instantaneous injections corotation can cut short the intensity profiles as the particle-filled flux tubes corotate away from the observer.

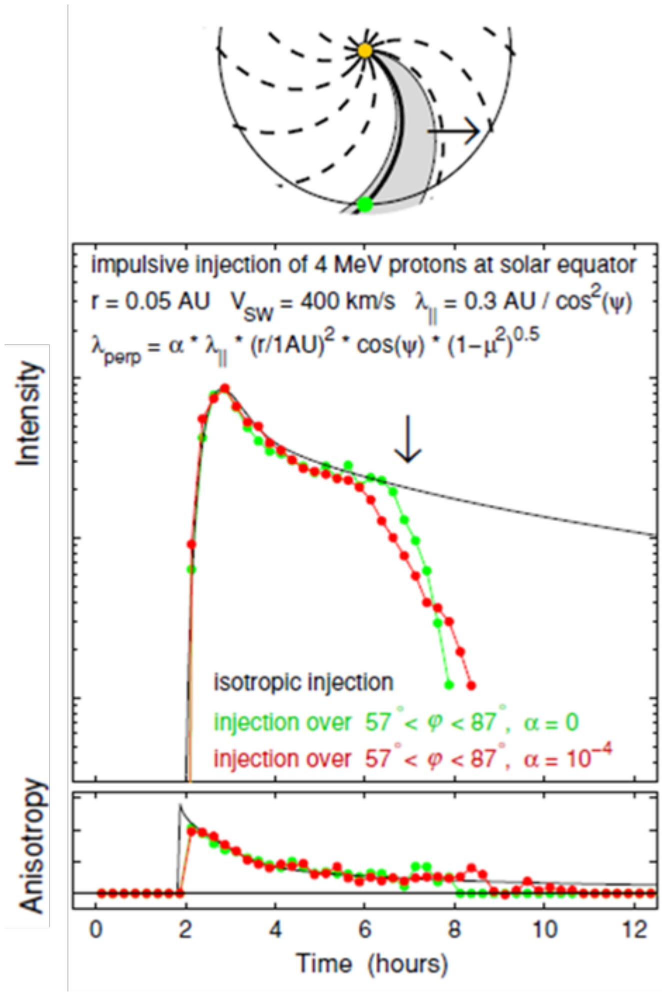

Figure 2.5: Effect of corotation for an impulsive SEP event from Dröge et al. (2010). Top: Schematic showing spatial extent of particles injected near the Sun (shaded region). Bottom: Intensity and anisotropy profiles determined at the observer that is located 4° from the boundary of the injection region, shown in the above panel. In the intensity and anisotropy profiles the solid black lines show the 1D prediction with the same parameters. The observer loses connection to the populated flux tube due to corotation in ~ 7 hours. [Image credit: Dröge et al. (2010)].

Giacalone & Jokipii (2012) modelled instantaneous injections near the Sun and utilised a model of diffusive transport where they consider the corotation of magnetic flux tubes. They inject ^{3}He with a power law spectrum of energies between 1 MeV/nuc and 1 GeV/nuc and derive intensity profiles for $1-2$ MeV/nuc ^{3}He at 1 au. They find that due to scattering the instantaneous injection could lead to an event that lasts around a few days at 1 au. They note that considering smaller mean free paths (increased number of scattering events) would likely increase the duration of the event. The authors note that even without perpendicular transport, scattering leads to a longitudinal spread in the SEPs due to the long timescales of radial propagation and the corotation of magnetic flux tubes. Giacalone & Jokipii (2012) varied the ratio of perpendicular to parallel diffusion coefficients (proportional to the parallel mean free path), effectively altering the rate of perpendicular diffusion. They find that spacecraft separated by up to 180° in longitude can observe particles from the same instantaneous injection from a point source near the Sun when considering reasonable ratio of perpendicular to parallel diffusion coefficients ($\gtrsim 0.005$). This study clearly shows that propagation effects of SEPs perpendicular to the IMF can have a significant impact on the spatial distribution of SEPs, in contrast to 1D focussed transport models where particles remain tied to the original IMF line that they are injected on (Bieber et al. 1994).

Marsh et al. (2015) presented the *SPARX* space weather forecasting model, based on the same test particle model that is used in this thesis. They considered instantaneous particle injections near the Sun. *SPARX* uses a database of model runs to quickly build intensity profiles, considering flare location and peak flux as input parameters. The authors conclude that corotation plays a role in determining the longitudinal extent of an SEP event, similarly to Giacalone & Jokipii (2012), but conclude that it is not significant enough to explain the rapid spread of SEP populations measured in multi-spacecraft events (e.g. Gómez-Herrero et al. 2015).

Despite the studies described in this section, corotation is generally ignored in the analysis of SEP events, particularly for gradual events. It remains unclear how shock-injected populations are affected by the corotation of the magnetic flux tubes. The role of corotation on events associated with a shock-like injection will be discussed in chapter 7.

Chapter 3

CMEs as energetic particle sources

In the previous chapter we introduced SEP sources, SEP propagation and models of the propagation process. In this chapter we focus on CMEs as possible sources of SEPs, describe models of SEPs from CME-sources, and outline the role that CME-driven shocks are thought to play during LDGRFs.

3.1 Models of gradual SEP events

Within the assumption that gradual SEP events are the result of energisation at a CME-driven shock, several properties of their intensity profiles have been linked to properties of shock acceleration. Reames et al. (1997) associated the long duration of gradual events with continued acceleration at the shock propagating through IP space. In addition the dependence of the overall shape of SEP intensity profiles on the location of the associated solar AR, (east-west effect, Cane 1988, ; see also Figure 2.2) has been attributed to the longitudinal variation of acceleration efficiency across the shock front (e.g. Tylka & Lee 2006; Zank et al. 2006).

A number of models have studied SEP acceleration/injection at CME-driven shocks with the purpose of deriving observables at 1 au, for comparison with observations. Several studies have modelled shock-like injections and the subsequent propagation of SEPs using particle transport equations (e.g. Kallenrode & Wibberenz 1997; Lario et al. 1998; Wang et al. 2012; Qin et al. 2013).

Kallenrode & Wibberenz (1997) used a black box shock model, and solved the 1D focussed transport equation to produce intensity and anisotropy profiles for a variety of particle injection and propagation parameters. In their model they consider that the shock acceleration efficiency varies across the shock front, with largest efficiency at the nose of the shock (as is the consensus within the scientific community, e.g. Reames et al. 1996, and references therein) and decreasing efficiency toward the flanks. They conclude that the intensity and anisotropy profiles observed by spacecraft are essentially determined by the temporal and spatial variation in shock acceleration efficiency and the capacity for SEPs to escape the shock front.

Lario et al. (1998) modelled SEP events with a transport equation that considered solar wind convection and adiabatic deceleration, and used an MHD model to derive the shock propagation. They fit particle flux and anisotropy profiles for four particle events and found that the efficiency of the shock as a particle accelerator decreases rapidly with distance from the Sun for proton energies greater than ~ 2 MeV.

Wang et al. (2012) modelled intensity and anisotropy profiles from a $70°$ wide shock, considering the same relation for the spatial variation of shock acceleration/injection efficiency as Kallenrode & Wibberenz (1997). The authors primarily focussed on how the inclusion/exclusion of perpendicular diffusion affects the intensity profiles for observers at 1 au. They concluded that with perpendicular diffusion spacecraft can observe particles before establishing magnetic connection to the shock source and after losing connection to the shock. They also highlight that due to adiabatic cooling particles lose energy as they transport and so particles detected in the same energy band over an event may have been injected at different energies, which has implications on the measured energy spectrum. The authors also mention that when the shock acceleration efficiency is constant with respect to radial position of the shock and longitude across the shock front, perpendicular diffusion leads to slower decay phases. However, when a power law dependence of the shock efficiency with respect to radial distance is considered, the difference between intensity profiles with and without perpendicular diffusion becomes smaller. This occurs because as shock efficiency decreases the loss of particles from the flux tube becomes more significant relative to the gain of particles from perpendicular diffusion. They note for small power law indices that perpendicular diffusion can lead to faster decays.

Qin et al. (2013) studied the effect of perpendicular diffusion on 5 MeV protons originating from a shock-like injection. They reproduced the reservoir phenomenon, where after long durations (days) the decay phases of multiple observers' intensity-time profiles at multiple longitudinal locations tend toward the same value (see He 2021). From their simulations they determine that they can more accurately reproduce the reservoir phenomenon when particle injection occurs close to the Sun, allowing perpendicular diffusion to take effect.

3.2 Geometry of CME-shock acceleration

In the interpretation of gradual SEP events in terms of CME-shock acceleration, several parameters/properties have been found to be of particular importance, as described in the following sections.

3.2.1 Magnetic connection to a shock-source

A spacecraft's magnetic connection to a CME-driven shock may vary depending on the spacecraft's longitudinal and latitudinal location: for example an observer may be connected to the nose of the shock or to the flanks. Over time as the shock propagates outward the distance of the observer to the shock varies and the shock region that the observer connects to also varies.

Some authors stress the importance of magnetic connection of the observer to the shock source using models (e.g. Heras et al. 1994). Heras et al. (1994) investigated a number of events observed by the *ISEE 3* spacecraft in the 35-1000 keV energy range that occurred over the period August 1978 to December 1980. The events were chosen via a specific set of criteria: 1. the particle event was associated with an IP shock detected at *ISEE 3*, 2. an increase in the 35-56 keV proton channel was detected at the shock passage, 3. the anisotropy was greater than or equal to 0.5 at some point in the event, 4. the IMF direction observed during the event was steady (so Parker spiral IMF can be assumed), 5. the onset of the event is isolated (i.e. not overlapped by a previous event), 6. apart from the solar source of the event there are no other flares that could contribute to the observed particle flux and anisotropy. These rather strict sampling conditions meant that only a very specific scenario is considered by the authors, where the shock passes directly over the observing spacecraft. The authors sought to explain the intensity and anisotropy profiles of the events by creating a simple model of a spherical shock and considering the magnetic connection along a Parker spiral IMF to an observing spacecraft. It is worth noting that the authors do not account for particle propagation effects and so are effectively assuming 1D focussed transport, whereby the particles are tied to the IMF lines that they are initially accelerated on. They introduce the term "cobpoint": for a given observer the cobpoint is the location on the shock front to which the observer is magnetically connected at a given time. Using the assumption of the spherical shock and a Parker spiral IMF Heras et al. (1994) derived the radial distance at which the observer-shock connection is established, r_c, as:

$$r_c = 1 - \frac{v_{sw}}{\Omega}\left(\phi_s + \frac{\Delta\phi_s}{2}\right) \tag{3.1}$$

where Ω is the solar rotation rate, v_{sw} is the solar wind velocity, ϕ_s is the longitude on the Sun of the shock origin, and $\Delta\phi_s$ is the angular width of the shock. Note that Equation 3.1 considers a number of assumptions, namely that observers are located at 1 au and that all distances and velocities are in units of au (or au/s for velocities). Equation 3.1 was used to plot the solid and dashed lines in Figure 3.1, which displays how the longituidnal connection to the spacecraft is thought to change as the shock propagates to larger radial distances.

Heras et al. (1995) studied three low energy (35-1600 keV proton) SEP events that were thought to originate (at least in part) from a CME-driven shock. They used a compound model whereby they use MHD simulations to study the shock's parameter evolution and they consider a 1D focussed-diffusion particle transport

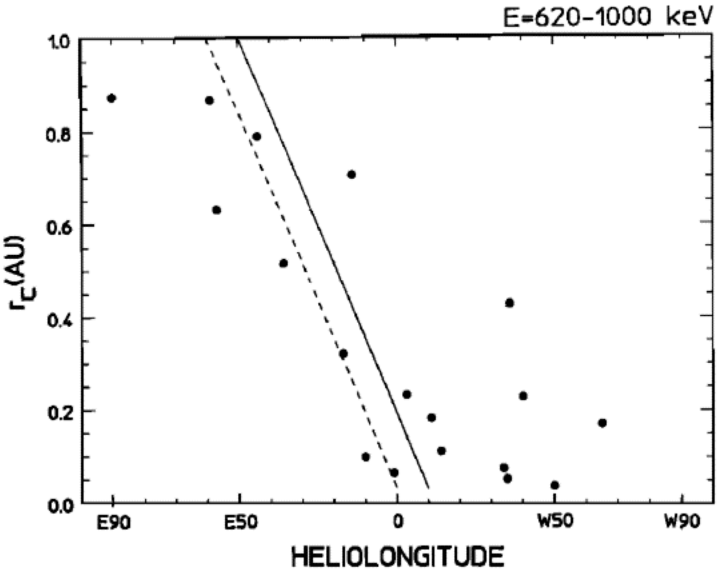

Figure 3.1: The heliocentric radial distance of the shock at the point where magnetic connection along the Parker spiral IMF to *ISEE 3* occurs versus the heliolongitudes on the Sun of the IMF line (calculated from the anisotropy increase onset of the 620 - 1000 keV range). The solid and dashed lines are the values obtained from assuming two spherical shocks, propagating with constant velocity, with angular widths of 100° and 120° respectively. [Image credit: Heras et al. (1994)]

model. They choose these events due to the relative position of the observing spacecraft and the parent AR (one western event, one eastern event and one close to the central meridian). One result that Heras et al. (1995) stress is the importance of the connection times of the observer to the shock. They mention that magnetic connection is established at later time for events that occur in the east, which corresponds to larger radial distances. They conclude that this implies that shock-accelerated particles are observed over longer time frames for western events, due to the increased duration of magnetic connection to the observer.

3.2.2 SEP injection efficiency across the shock front

The efficiency of particle acceleration is thought to vary across the shock front. This, in combination with the geometry of the observer relative to the shock front (and hence the cobpoint position), has been used to explain the general shape of intensity profiles (e.g. Kallenrode & Wibberenz 1997; Lario et al. 1998; Tylka & Lee 2006). Both Kallenrode & Wibberenz (1997) and Lario et al. (1998) consider shocks where particle injection efficiency exponentially decays from the shock centre toward the flanks of the shock.

Tylka & Lee (2006) argue that the evolution of shock normal angle with time for a given observer and the compound seed populations accelerated from the corona and from flares can be used to explain the differences in composition in large SEP events that depend on energy. Due to the geometry of the shock and the shape of Parker spiral magnetic field lines the shock normal at the cobpoint varies with time as the shock propagates outward. For an observer that sees the solar event as western the shock is initially quasi-parallel at the cobpoint. As time progresses, the shock at the cobpoint becomes quasi-perpendicular, due to the cobpoint moving eastward along the shock front toward the flank. Different acceleration mechanisms occur at quasi-parallel and quasi-perpendicular shock fronts (as summarised by Klein &

Dalla 2017).

3.3 CME-shock acceleration and LDGRFs

Share et al. (2018) and Winter et al. (2018) analysed the association of LDGRFs with soft-X-ray flares, CMEs and near-Earth SEP events and concluded that their most likely origin is back-precipitation after acceleration at a CME-driven shock. We refer to this in the following as the CME shock scenario. Jin et al. (2018) studied the 2014-September-01 behind-the-limb LDGRF event, performing a detailed analysis of the CME-driven shock up to the time when it reached ~ 10 $R_\odot$, focussing on the evolution of its parameters and magnetic connectivity. They find that the compression ratio of their simulated shock displays a similar evolution to the observed γ-ray profile for the first ~ 20 minutes of the event. On the other hand, a study of a variety of electromagnetic emissions for the same event led Grechnev et al. (2018) to favour γ-ray production via flare-accelerated protons that remain trapped in large flare loops, explaining the first ~ 20 minutes of the *Fermi* and hard X-ray observations.

The back-precipitation scenario has been studied by modelling both the shock acceleration and propagation to the solar surface of the energetic protons. Kocharov et al. (2015) concluded that the mechanism is a viable explanation for LDGRFs but pointed out that only about 1% of the particles accelerated at the shock back-precipitate to the required height. Afanasiev et al. (2018) used a model with strong scattering in the region behind the shock to show that a number of protons sufficient to produce the observed gamma-ray emission (or in some cases considerably more) propagate to the solar surface. Jin et al. (2018) suggested that scattering associated with turbulence would facilitate particle back-precipitation. Kouloumvakos et al. (2020) presented a study of the 2017 September 10 event in which they modelled the parameters of the associated CME-driven shock. They conclude that the evolution of the shock and its orientation can explain the time history of the γ-ray emission observed by *Fermi* LAT, providing further evidence for the CME-driven shock scenario.

3.3.1 Complications with the CME-shock scenario

Hudson (2018) and Klein et al. (2018) pointed out that magnetic mirroring is a major obstacle for proton back-propagation from a CME-driven shock to heliocentric distances $r \sim 1\,\mathrm{R}_\odot$, where γ-ray emission takes place. Due to the solar wind expansion and associated $1/r^2$ dependence of the magnetic field magnitude, in the absence of scattering only particles in a very narrow range of pitch angles (the so-called loss cone) are able to avoid reflection as they move towards the Sun. An open question is how this picture is modified by scattering associated with magnetic field turbulence.

de Nolfo et al. (2019) analysed 1 au SEP data from the Payload for Antimatter Matter Exploration and Light-nuclei Astrophysics (*PAMELA*) space experiment, the Geostationary Operational Environmental Satellites (*GOES*) and the twin Solar TErrestrial RElations Observatory (*STEREO*) spacecraft to reconstruct the SEP spatial distribution, accounting for both longitudinal and latitudinal magnetic connectivity, to derive the overall number of protons at 1 au, N_{SEP}, for 14 events associated with LDGRFs. They compared N_{SEP} with the number of interacting γ-ray-producing protons at the Sun, N_{LDGRF}, as inferred from *Fermi*/LAT data by Share et al. (2018). They found no correlation between the two populations and showed that in several events $N_{LDGRF} \gtrsim N_{SEP}$, implying that back-precipitation of a very large fraction of the energetic particles would be required to explain the events within the CME shock acceleration scenario.

Particles accelerated at a CME-driven shock would need to traverse three distinct magnetic field regions in order to back-precipitate: IP space characterised by a magnetic field that can be approximated as a Parker spiral; the corona, with a complex magnetic field configuration consisting of open and closed magnetic field, and the near photosphere region, typically described as a 'canopy' (Seckel et al. 1991).

The highest-energy particles are thought to be accelerated around the shock nose, where the shock is strongest and fastest, while its compression ratio and speed decrease quickly at the flanks resulting in a reduced acceleration efficiency (e.g. Cane 1988; Reames 2009; Hu et al. 2017). However, other studies have suggested that the shock flanks may contribute (e.g. Kahler 2016). In general, the position on the shock where the highest-energy particles are accelerated may vary with time and may be strongly influenced by local conditions including the magnetic-field configuration (e.g. Afanasiev et al. 2018; Kong et al. 2019). We study the CME-shock scenario for LDGRFs in chapter 5.

Chapter 4

Test-particle simulations of SEPs with a shock-like source

In this chapter we discuss the full-orbit test particle code, how it works and what adaptations were made so we could model the scenarios we investigated over the PhD.

4.1 The full-orbit test particle code

We model SEP propagation using a full-orbit test particle code written in Fortran90 (sometimes referred to as the Fortran code). The code was originally developed by Dalla & Browning (2005) to investigate particle acceleration at magnetic reconnection sites on the Sun. The Fortran code has been used to investigate many different aspects of SEP propagation, from its use in forecasting SEP events via the *SPARX* model to investigating Ground Level Enhancements (GLEs) and other scenarios (e.g. Battarbee et al. 2018; Dalla et al. 2013, 2020; Marsh et al. 2013, 2015; Hutchinson et al. 2022; Waterfall et al. 2022).

Full-orbit test particle simulations inject a number of individual "test particles" and determine the trajectory of each particle individually. Unlike other approaches, like GC simulations, our code is a "full-orbit" code, meaning that we consider the full gyration of the charged particles as they propagate through the IMF. There are assumptions associated with using this approach, namely that the individual particle's trajectories are not affected by the presence of other particles, they do not influence the fields, and only depend on forces from the magnetic and electric fields. This means that we can consider a single particle's trajectory at a time. There are 4 main phases of the simulation: particle injection and initial conditions, propagation, scattering, and output, which we explain further in the following sections.

4.1.1 Scattering events

We account for particle interactions with magnetic turbulence by considering pitch angle scattering events. We utilise an ad-hoc scattering method (see Marsh et al. 2013; Dalla et al. 2020) where the particle's velocity vector is randomly reoriented to another location on the sphere in velocity space, thereby changing the particle's pitch angle. The scattering events are Poisson distributed, with an average scattering time of $t_{scat} = \lambda/v$ where v is the particle's velocity (Marsh et al. 2013) and are random for each particle. Scattering takes place within the solar wind frame.

During scattering events the particles GC can be displaced by up to two Larmor radii, leading to SEPs spreading perpendicular to the IMF by a small amount. Figure 4.1 shows this process. In the figure the positively charged particle is following the blue dashed trajectory with a velocity of $\mathbf{v_1}$ and a GC, GC_1. The particle then experiences a pitch angle scattering event where its velocity vector is flipped 180°. This causes the maximum perpendicular displacement of the GC from GC_1 to GC_2 of two Larmor radii, represented by the red arrow. Now the particle will travel along the green dashed trajectory with velocity $\mathbf{v_2}$.

The displacement of the GC during scattering events is a finite Larmor radius effect and it is not related to the perpendicular diffusion considered in some other studies (e.g. Wang et al. 2012; Qin et al. 2013; Zhang et al. 2009). There is no process to account for perpendicular diffusion within the code at the current time. It will be the subject of future studies.

4.2 Particle injection/ Initial conditions

The initial conditions $\mathbf{x_0}$, $\mathbf{p_0}$ for integration of Equations 4.1 - 4.2, as well as the mass and charge, need to be specified for all particles in the population. This requires specifying particle species, injection location, initial velocity/momentum. In

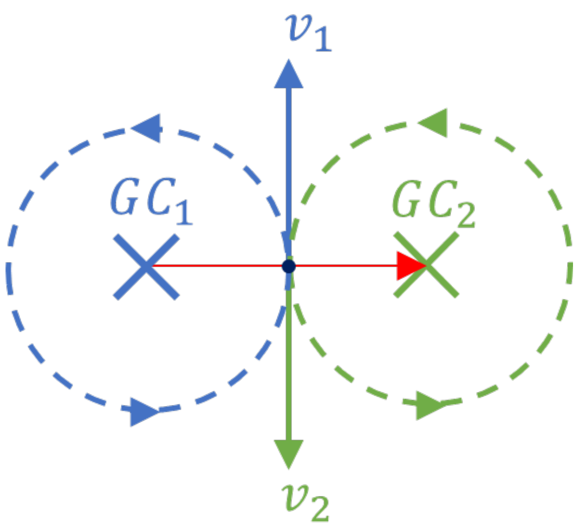

Figure 4.1: Displacement of a particle's GC due to pitch angle scattering (also referred to as a finite Larmor radius effect). The positively charged particle (dark blue circle) has initial velocity $\mathbf{v_1}$ and GC, GC_1 and would continue to follow the blue dashed trajectory around magnetic field pointing into the page. After the pitch angle scattering event the particle has velocity $\mathbf{v_2}$ and GC, GC_2 and will follow the green dashed trajectory. The red arrow represents the change in GC location associated with a 180° flip in velocity due to a pitch angle scattering event, corresponding to a shift of two Larmor radii.

Variable	Description	Typical value
E_0	Particle initial kinetic energy (monoenergetic)	5 MeV
δ_0	Latitudinal centre of the injection region	0°
ϕ_0	Longitudinal centre of the injection region	0°
v_{sw}	Solar wind speed	500 km/s
r_0	Radial position of the injection region	2 $R_\odot$
N_p	Total number of particles injected	1×10^6

Table 4.1: Initial conditions required to produce an instantaneous injection in the test particle code and their typical values.

this work we consider monoenergetic populations with a specified initial distribution in velocity space. Previously, our code has used an instantaneous injection method, where all particles are injected at the same heliocentric radial distance at the same time. Particles were randomly distributed within an injection area corresponding to an angular width defined by the user. The required inputs into the code for the previously used instantaneous injections are displayed in Table 4.1. This instantaneous injection method was useful for considering flare-accelerated SEP populations due to its impulsive nature. The angular width of the injection has typically been kept small to mimic a localised acceleration of SEPs (e.g. Dalla et al. 2013, 2020; Marsh et al. 2013, 2015; Waterfall et al. 2022). Initially, the velocity distribution of the particles was hemispheric, corresponding to anti-sunward propagating particles. We have adapted this for the scenario of a CME-driven shock to now inject particles with a fully isotropic velocity distribution, consistent with typical diffusive shock acceleration theories (Baring 1997; Desai & Giacalone 2016). This was a very important adaptation when considering the proton back-precipitation scenario, as particles propagating sunward play a major role as well as scattered anti-sunward particles. When injecting an isotropic distribution of particle velocities a uniform distribution in the cosine of pitch angle is required, which can be seen in Figure 4.2

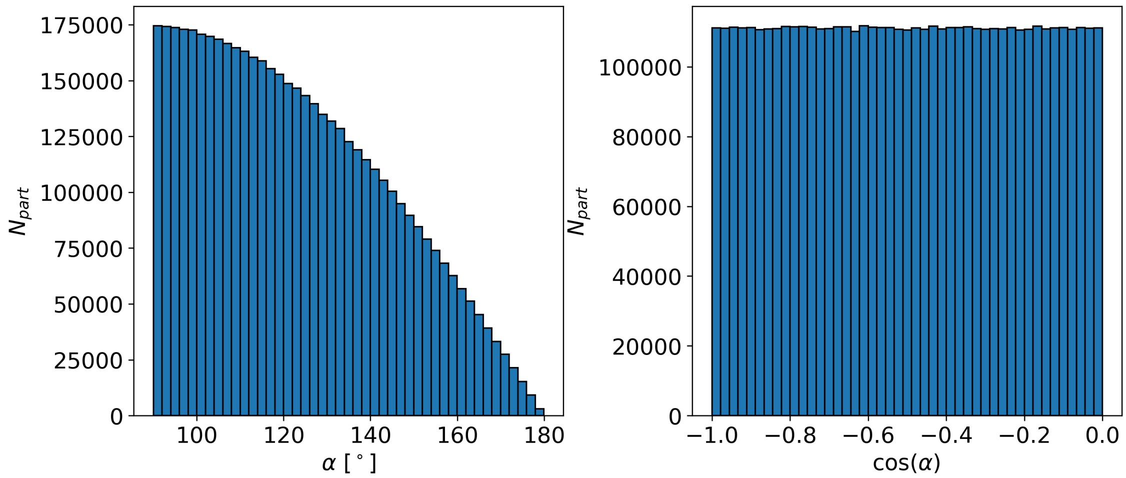

Figure 4.2: Pitch angle distribution from a hemispheric sunward injection consisting of 5 million protons (left). Cosine of left panel pitch angle distribution (right).

for a hemispheric injection. The reason why the distribution must be uniform in the cosine of pitch angle is that lines of constant longitude converge near the poles in a spherical coordinate system and so for a uniformly distributed population on a surface of a sphere fewer particles must be injected at the poles of the distribution (in this case closer to $\alpha = 180°$).

4.2.1 Particle propagation

To propagate the SEPs each particle's equation of motion is numerically integrated to determine the particle trajectory. The particle's equation of motion is given by,

$$\frac{d\mathbf{p}}{dt} = q\left(\mathbf{E} + \frac{1}{c}\frac{\mathbf{p}}{m_0\gamma} \times \mathbf{B}\right) \tag{4.1}$$

where $\mathbf{p}$ is the particle momentum, t is time, c is the speed of light, q is the charge of the particle, m_0 is the particle rest mass, γ is the Lorentz factor and $\mathbf{E}$ (see Equation 4.5) and $\mathbf{B}$ (see Equation 4.3) are the electric and magnetic fields respectively. Here the Gaussian system of units is used as is customary in the study of high energy charged particle transport. Equation 4.1 together with the equation:

$$\frac{d\mathbf{x}}{dt} = \frac{\mathbf{p}}{\gamma m_0} \tag{4.2}$$

where $\mathbf{x}$ is the particle position, forms a set of 6 differential equations. The test particle code integrates Equations 4.1 - 4.2 to derive the particle trajectory $\mathbf{x}(t)$, $\mathbf{p}(t)$. The integration method used is the Bulirsch-Stoer method, which is an iterative method that continues to iterate until the error on the integration value is below a given threshold. This enables us to ensure that the uncertainty on the position of the particle is kept small. Typically, the uncertainty on each integration is less than 10^{-9} $R_\odot$ in each spatial variable. We have altered this value to determine which value of the tolerance is most suitable, considering 10^{-8} $R_\odot$ and 10^{-10} $R_\odot$. There was a negligible change in the simulation outcome (the number of particles reaching the solar surface), so we chose to use 10^{-9} $R_\odot$ as the tolerance for the integration for all simulations. For each particle within the simulation the equation of motion (Equation 4.1) is integrated from the injection time until the first scattering time (or the next spec output time - see section 4.4), whichever is sooner. After the particle's velocity has been scattered, integration resumes until the next scattering event (or spec output time) and the same is repeated up until the final time of the simulation.

4.2.2 Interplanetary Magnetic Field

We consider in all of our simulations a unipolar Parker spiral IMF (typically with positive polarity, ie. field lines pointing anti-sunward). We use a spherical coordinate system (r, θ, ϕ) where r is the radial distance from the centre of the Sun, θ is heliographic colatitude and ϕ is heliographic longitude, with corresponding unit vectors $\hat{\mathbf{e}}_\mathbf{r}$, $\hat{\mathbf{e}}_\theta$, $\hat{\mathbf{e}}_\phi$. The Parker spiral IMF is given by,

$$\mathbf{B} = \frac{B_0 r_0^2}{r^2}\hat{\mathbf{e}}_\mathbf{r} - \frac{B_0 r_0^2 \Omega \sin\theta}{v_{sw} r}\hat{\mathbf{e}}_\phi, \tag{4.3}$$

where $\hat{\mathbf{e}}_\mathbf{r}$ and $\hat{\mathbf{e}}_\phi$ are unit vectors in the radial and aziumuthal (longitudinal) directions respectively, B_0 is the magnetic field strength at a fixed reference radial distance r_0, Ω is the sidereal solar rotation rate, and v_{sw} is the solar wind speed.

In the code it is possible to include a Heliospheric Current Sheet (HCS) and two polarities, however in this first investigation of a CME-shock-like injection the HCS has not been considered. The HCS morphology changes dramatically from event to event, therefore it is sensible to exclude it in this study to ensure the results can be applied as a general case, and because interaction of a CME with the HCS would need to be modelled. Ideally, when investigating specific events an event-specific HCS should be included, constructed from source surface maps (e.g. Battarbee et al. 2018; Waterfall et al. 2022).

4.2.3 Electric field and corotation

A number of drift effects are present within the test particle code, which are intrinsic to the model, i.e. they arise naturally due to the magnetic field (Equation 4.3) having a gradient and curvature (Dalla et al. 2013). Corotation naturally occurs in our test particle code with the inclusion of the solar wind electric field in the equation of motion of the particle (see Equation 4.1). By setting the electric field to zero we remove the effects of corotation, allowing us to easily compare the effects that corotation has on the outputs of the simulations.

The solar wind electric field as would be observed in a frame in which the solar wind moves with velocity $\mathbf{v_{sw}}$, is given by:

$$\mathbf{E} = \frac{-\mathbf{v_{sw}} \times \mathbf{B}}{c} \tag{4.4}$$

where $\mathbf{B}$ is the magnetic field and c is the speed of light.

For the unipolar Parker spiral magnetic field considered in this work (Equation 4.3) and assuming the solar wind to be purely radial and uniform across the solar surface, Equation 4.4 takes the form:

$$\mathbf{E} = -\frac{B_0\, r_0^2\, \Omega\, \sin\theta}{c\, r}\hat{\mathbf{e}}_\theta. \tag{4.5}$$

The electric field drift for particles travelling through orthogonal electric and magnetic fields is given by:

$$\mathbf{v_d} = \frac{c\,\mathbf{E} \times \mathbf{B}}{B^2} \tag{4.6}$$

where $\mathbf{v_d}$ is the $\mathbf{E} \times \mathbf{B}$ drift velocity.

Using Equations 4.3, 4.5, 4.6 we calculate that for our simulations the particles' $\mathbf{E} \times \mathbf{B}$ drift velocity in a local Parker spiral coordinate system (Burns & Halpern 1968; Kelly et al. 2012; Dalla et al. 2013) takes the form:

$$\mathbf{v_d} = \frac{v_{sw} r}{(r^2 + a^2)^{1/2}} \hat{\mathbf{e}}_{\phi'} \tag{4.7}$$

where $\hat{\mathbf{e}}_{\phi'}$ is the unit vector in a local Parker spiral coordinate system which points in the direction of solar rotation (perpendicular to the Parker spiral IMF) and a is a function of colatitude defined as:

$$a = \frac{v_{sw}}{\Omega \sin\theta}. \tag{4.8}$$

Hence, only motion in the direction of solar rotation (the $\hat{\mathbf{e}}_{\phi'}$ direction) perpendicular to the IMF lines occurs. This motion is independent of particle properties, such as speed, charge and mass, and describes the corotation of particles with the IMF lines as the Sun rotates, corresponding to drift of $\sim 14.2°$ per day westward (Dalla et al. 2013).

4.3 Shock-like injection

Up to the present time within the scientific literature there was no full-orbit test particle model capable of describing a continuous particle injection by a CME-driven shock as it propagates into IP space. We developed, for the first time, a description that produces a temporally extended shock-like injection for our full-orbit test particle code. It is a simplified description aiming to capture the geometry and temporal evolution of the particle injection. The details of how the injection is specified are described below.

We have developed a particle injection model that approximates a temporally extended injection from a propagating shock-like source (referred to in the following as the shock). We chose to describe the CME front via a cone model for its simplicity, similar to that of Heras et al. (1994) and Kallenrode & Wibberenz (1997). Our model consists of a shock-like injection region with constant angular width in longitude and latitude: the injection is spatially extended across the shock front and temporally extended, i.e. occurring over timescales of days as the shock propagates radially outward. A visual depiction of the shock surface at four different times is displayed in Figure 4.3, where the coloured surfaces correspond to shock positions when $t = 8$ hr (blue), 16 hr (green), 32 hr (orange) and 48 hr (red) for a shock speed of $v_{sh} = 1500$ km/s. Our simplified description accounts for the geometric characteristics of the shock injection and its evolution with time, but it does not model acceleration nor the evolution of the shock as an MHD structure. Ideally, our test particle code would make use of a MHD code to provide accurate evolution of particle injection parameters at the evolving CME-driven shock front. However, it was not feasible to undertake this due to the time constraints of the PhD. We note that the shock has negligible thickness within the model.

Features of the shock's downstream region are not modelled. This is often characterised by a complicated magnetic configuration, due to the presence of a flux rope (e.g. Zurbuchen & Richardson 2006) and non-Parker magnetic field lines (see e.g. Lario et al. 1998, Figure 1).

The shock is assumed to propagate with a constant speed, v_{sh}, and maintain the same angular width in longitude and latitude as it propagates. Particle injection is assumed to continue as the shock propagates through the corona and interplanetary space, taking place over $r \in [r_{min}, r_{max}]$, where r_{min} and r_{max} are the minimum

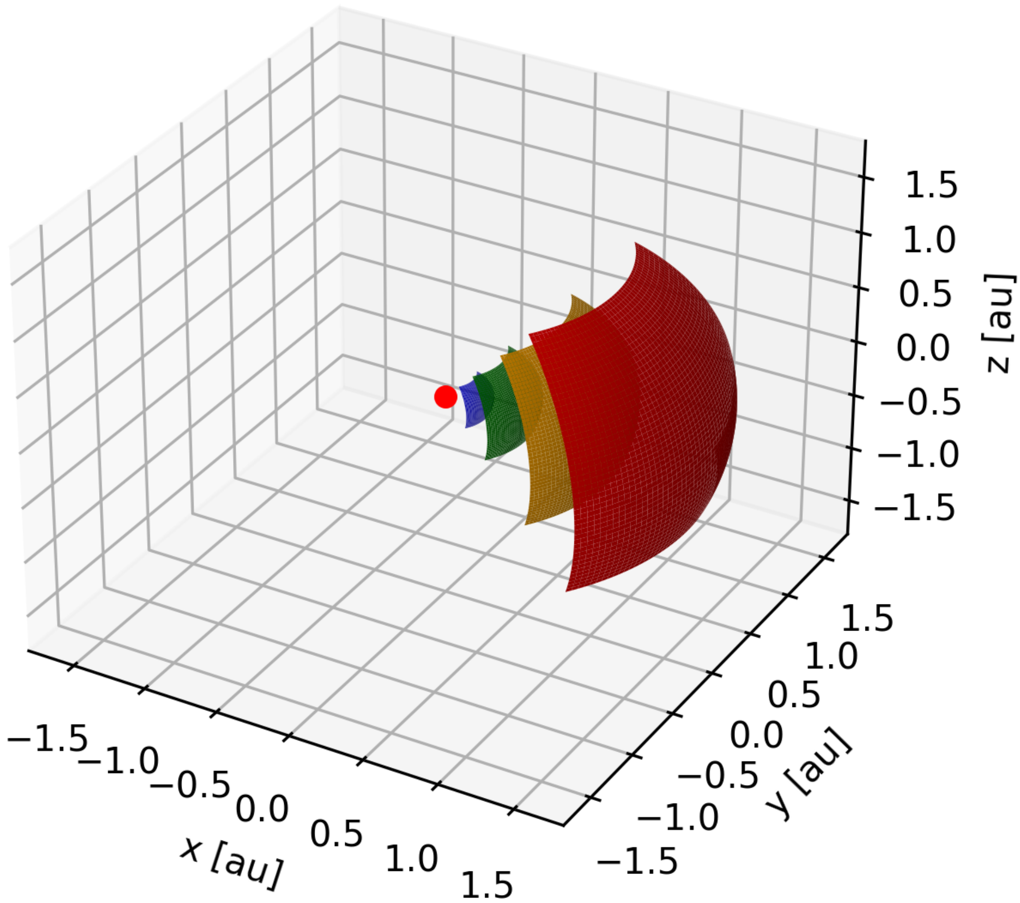

Figure 4.3: The shock-like injection surface at four different injection times: 8 hr (blue), 16 hr (green), 32 hr (orange), and 48 hr (red) after the initial time (t = 0 hr).

and maximum particle injection radii. We choose $r_{min} = 1.2\,\mathrm{R}_\odot$, the median shock formation height as determined by Gopalswamy et al. (2013b).

The shock in the model acts only as a particle source and does not interact with or modify the IMF, which is assumed to be a Parker spiral (Equation 4.3). Particles are injected with an isotropic velocity distribution from the shock surface throughout its propagation, consistent with theories of diffusive shock acceleration (Baring 1997; Desai & Giacalone 2016). The shock is effectively transparent to particles, meaning any particle that returns to the shock position during its propagation does not interact with it and travels straight through, without change to its trajectory.

Table 4.2 summarises the shock parameters and gives the typical values used in our simulations unless otherwise stated. We define $w_{sh,\phi}$ as the longitudinal width of the shock, $w_{sh,\theta}$ as the colatitudinal width, and δ_{cent} as the latitude of the centre of the shock (where $\delta = 90^\circ - \theta$ is latitude). In the majority of our simulations we choose $w_{sh,\phi} = w_{sh,\theta} = 70^\circ$, a purely radial shock speed $v_{sh} = 1500$ km/s, and we assume that particle acceleration/injection takes place over a period of two days, resulting in $r_{max} = 372\ \mathrm{R}_\odot$ (= 1.73 au). The shock is centred at $\phi_{cent} = 0^\circ$ and latitude, $\delta_{cent} = 15^\circ$, so as to represent the typical CME latitudes, corresponding to the positions of the activity belts on the solar disc.

4.3.1 Injection functions and normalisations

We introduce a function $S(r, \theta, \phi)$ describing the number of particles per unit volume injected by the shock at position $(r,\ \theta,\ \phi)$, in the spherical coordinate system introduced in Section 4.2.2, so that

$$\int d^3\mathbf{r}\, S(r, \theta, \phi) = N_p \tag{4.9}$$

with N_p the total number of particles and $d^3\mathbf{r}$ the unit volume. Here the dependence on time is folded into the radial dependence via $r = v_{sh}\, t$.

Variable	Description	Value
v_{sh}	Radial velocity of the shock	1500 km/s
$w_{sh,\phi}$	Longitudinal width of the shock	70°
$w_{sh,\theta}$	Latitudinal height of the shock	70°
δ_{cent}	Latitude of shock centre	15°
ϕ_{cent}	Longitude of shock centre	0°
σ_ϕ	Longitudinal σ of injection efficiency [a]	17.5°
σ_θ	Latitudinal σ of injection efficiency [a]	17.5°
r_{min}	Minimum radial injection position	1.2 $R_\odot$
r_{max}	Maximum radial injection position	1.73 au
r_{peak}	Radial position of peak injection [b]	5 $R_\odot$
N_p	Total number of protons injected	1×10^6

[a]Only used for Gaussian $\Phi(\phi)$ and $\Theta(\theta)$ [b]Only used for Weibull function injection in r

Table 4.2: Parameters of shock-like injection in our test particle simulations. Columns are from left to right: variable name, parameter description and typical value used.

We assume that S is separable (similar to the method of Kallenrode & Wibberenz 1997), so that;

$$S(r,\theta,\phi) = N_p \, \frac{R(r)}{r^2} \, \frac{\Theta(\theta)}{\sin\theta} \, \Phi(\phi) \tag{4.10}$$

where $R(r)$, $\Phi(\phi)$, $\Theta(\theta)$ are the radial, longitudinal and colatitudinal injection functions, satisfying the normalisation conditions:

$$\int dr \; R(r) = 1 \tag{4.11}$$

$$\int d\theta \; \Theta(\theta) = 1 \tag{4.12}$$

$$\int d\phi \; \Phi(\phi) = 1 \tag{4.13}$$

Radial injection function

The way in which the particle injection efficiency varies with radial distance is not well understood. However, the highest energy particles responsible for GLEs are thought to be accelerated close to the Sun (Reames 2009; Gopalswamy et al. 2013a). It is also thought that lower energy particles can be accelerated at larger radial distances (evidenced by energetic storm particle events, e.g. Desai & Giacalone 2016; Wijsen et al. 2022, and references therein). Hence, the radial injection function of the shock is energy dependent. While the code is capable of injecting a particle population with a spectrum in energies for simplicity, in this work we use a monoenergetic proton population.

In our model we consider a number of radial injection functions to study their effect on SEP profiles at 1 au. The simplest radial injection function is $R(r) = const$, the uniform case, where the shock injects the same number of particles as r increases. The normalisation condition for the uniform case gives:

$$R(r) = \frac{1}{(r_{max} - r_{min})}. \tag{4.14}$$

We note that as the shock propagates to larger radial positions with fixed angular width the surface area of the shock increases as r^2. Therefore for uniform $R(r)$ (Equation 4.14) the number of particles injected per unit area of the shock, $Q(r)$, decreases with r like $1/r^2$ (see Figure 4.4 bottom panel).

We also consider a non-uniform injection given by the modified Weibull function (previously used to describe SEP profiles by Kahler & Ling 2018). Normalised over our injection range this is given by,

$$R(r) = \frac{(-\alpha/\beta)(r/\beta)^{\alpha-1}\exp(-(r/\beta)^{\alpha})}{\exp\left(-(r_{max}/\beta)^{\alpha}\right) - \exp\left(-(r_{min}/\beta)^{\alpha}\right)}, \tag{4.15}$$

where α ($\alpha < 0$) and β are parameters that determine the shape of the function, specifically the rise and decay rates and the position of the peak. In our work we choose $r_{peak} = 5\ \mathrm{R}_\odot$, which results in a fast rise phase near the Sun and a decay phase beyond 5 $\mathrm{R}_\odot$. For a chosen α value we calculate β using the following expression,

$$\beta = \left(\frac{\alpha\, r_{peak}^{\alpha}}{\alpha - 1} \right)^{1/\alpha} \tag{4.16}$$

to ensure that the peak injection is fixed at 5 $\mathrm{R}_\odot$. Therefore, by altering alpha we can change the injection function's rise and decay phases. As α approaches zero, the injection becomes increasingly like a delta function at the peak radial distance. The decay phase becomes more rapid and we may accidentally shorten the possible injection radial distance range if not chosen carefully. As α becomes increasingly negative, the peak in the distribution becomes less pronounced and the decay phase remains very high until the maximum injection location. After considering a range of possible α values, we chose $\alpha = -0.2$ as it provided a clear peak injection while still retaining a significant decay phase that would not shorten the injection. This corresponds to $\beta = 38880.0\ \mathrm{R}_\odot$.

The Weibull function is plotted in orange in Figure 4.4 (top panel).

To study the case of constant injection per unit area of the shock, we also consider a radial injection function proportional to r^2, This function is described by,

$$R(r) = \frac{3r^2}{(r_{max}^3 - r_{min}^3)}. \tag{4.17}$$

The general equation that describes the number of injected particles per unit area of the shock is,

$$Q(r) = \frac{R(r)\, N_p}{A(r)} \tag{4.18}$$

where $A(r)$ is the surface area of the shock front at a given radial position, given by,

$$A(r) = 2\, r^2\, w_{sh,\phi}\ \cos(\delta_{cent})\ \sin(w_{sh,\theta}/2). \tag{4.19}$$

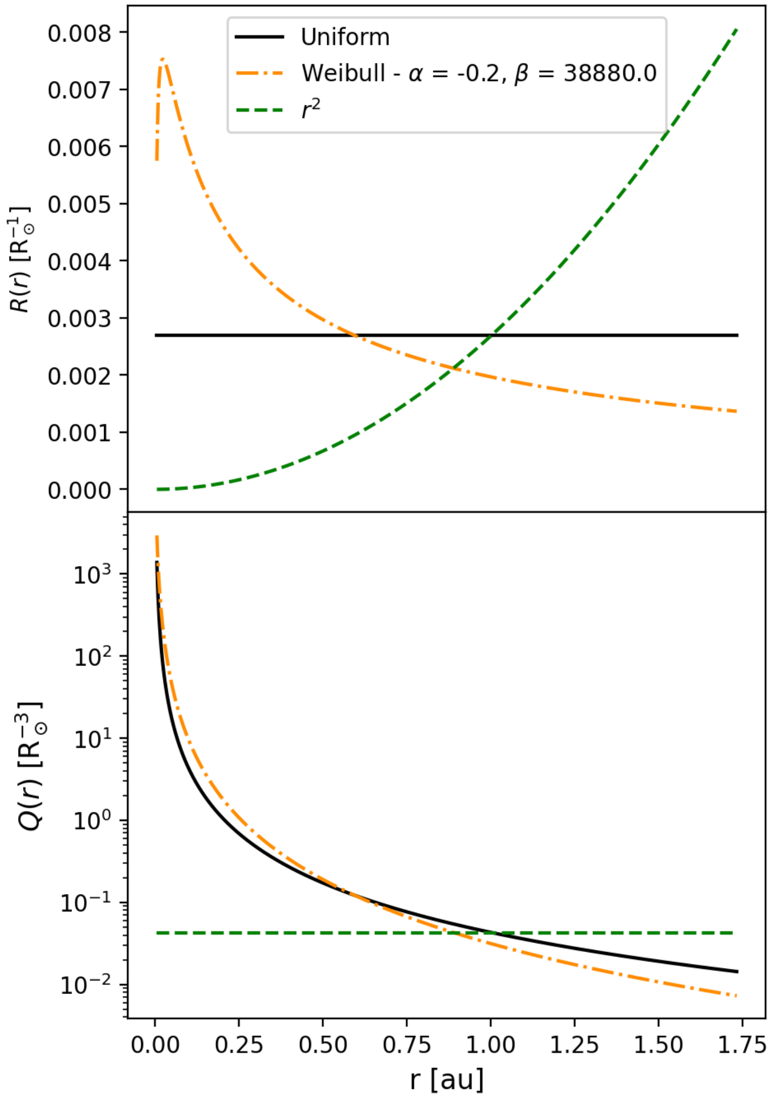

Figure 4.4: Radial injection function, $R(r)$ versus r (top) and the number of particles injected per unit area of the shock, $Q(r)$ versus r (bottom).

Figure 4.4 (top) displays all radial injection functions, $R(r)$ versus radial shock position and Figure 4.4 (bottom) displays the corresponding $Q(r)$.

Longitudinal/latitudinal injection functions

We consider two types of injection efficiency with respect to longitudinal and latitudinal position across the shock front. The first is uniform injection efficiency across the shock front, described by the normalised expressions:

$$\Phi(\phi) = \frac{1}{w_{sh,\phi}} \tag{4.20}$$

$$\Theta(\theta) = \frac{1}{2\cos(\delta_{cent})\sin(w_{sh,\theta}/2)} \tag{4.21}$$

The second longitudinal and latitudinal injection function is a Gaussian centred about the shock nose. Typically we consider standard deviations of σ_ϕ (σ_θ) = $w_{sh,\phi}/4$ ($w_{sh,\theta}/4$). The two injection functions are displayed in Figure 4.5 for the longitudinal injection efficiency.

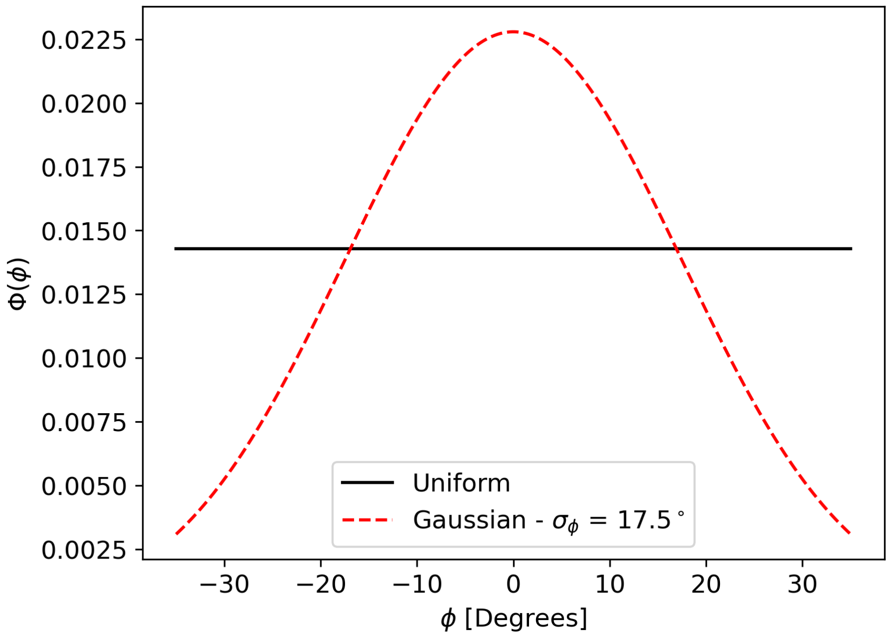

Figure 4.5: Longitudinal injection function, $\Phi(\phi)$ for the shock-like injection.

Method for generating initial positions according to injection functions

Within the test particle model, we considered a population of N_p protons with initial conditions distributed according to the specified injection functions. The methodology used to generate the initial conditions was Inverse Transform Sampling (ITS).

The distribution specified by the injection function must be randomly sampled so that our finite number of test particles accurately represents the injection function.

Assuming that the Probability Distribution Function (PDF), $P(x)$ (injection function) is analytically integrable, the method works by integrating the PDF to obtain the Cumulative Distribution Function (CDF), $F(x) = \int P(x)dx$. The CDF is a monotonically increasing function that starts at 0 at the minimum integration value and increases to 1.0 at the maximum integration value.

To determine a random number according to the PDF we need to find the inverse of the CDF to gain the Inverse Cumulative Distribution Function (ICDF), $F(\xi) = F^{-1}(x)$. The ICDF then relates the value for the variable of the original PDF (x) to a value between 0 and 1.0, ξ, corresponding to the cumulative likelihood of being located by that value of x, i.e. for a random number between 0 and 1 there is a distinct value of x that is returned by the ICDF.

Therefore, to determine a random injection position for a particle we can simply pass a uniform random number between 0 and 1 to the desired function's ICDF and it will output a radial distance of injection.

For our simulations we integrate over the radial distance range covered by the shock. By normalising the PDF over the radial distance range of the CME-driven shock [r_{min}, r_{max}], we constrain the radial distance range for the CDF. Hence, the probability of a particle being injected over the distance range [r_{min}, r_{max}] is set to 1.

The ITS method was used to generate particle initial positions according to the specified injection function. This process was vital in determining the injection radial positions for the Weibull and r^2 injection functions.

For example, for the modified Weibull function (Equation 4.15), the CDF is given by,

$$CDF = F(r) = \frac{\exp\left(-(r/\beta)^{\alpha}\right)}{norm}. \tag{4.22}$$

where $norm$ is a normalisation constant, given by,

$$norm = \exp\left(-(r_{max}/\beta)^{\alpha}\right) - \exp\left(-(r_{min}/\beta)^{\alpha}\right). \tag{4.23}$$

Then to obtain the ICDF we need to find the inverse of Equation 4.22. The ICDF for the Weibull function is given by,

$$ICDF = F^{-1}(r) = F(\xi) = \beta\left(-\ln\left(\xi\, norm + \exp\left(-(r_{min}/\beta)^{\alpha}\right)\right)^{\frac{1}{\alpha}}\right) \tag{4.24}$$

where ξ is a random number between 0 and 1. Hence, we can pass a uniformly random number between 0 and 1 to this ICDF to generate an accurate random sample of the modified Weibull function injection.

4.4 Data output

Data is output from the test particle simulation in two ways. Either particle data are written to files at set time steps ("spec" files) or particle data are written to files when particles cross a fixed radial distance (cross files), for example 1 au. A combination of both of these methods enables us to to follow the SEP population over the whole simulation (using spec files) but retains high resolution around the fixed radial distance defined to obtain cross files.

Over the course of the PhD modifications to the test particle code were made to allow efficient simulations to be run when considering particles close to the Sun. Typically, the cross boundary is set to 1 au (since we usually care about the SEP populations that reach the Earth). Here we created a second boundary at 1 $R_{\odot}$ to carefully monitor the number of protons that reach the solar surface. We also added additional conditions so that protons were recorded only if they passed this boundary from larger radial distances and we stopped propagating these particles once they were recorded via the cross method. This meant that once particles reached the solar surface they could not be counted again and were effectively “absorbed” in the solar atmosphere, emulating the process during LDGRFs. This “proton absorption” condition was vitally important to our work as it enabled us to run simulations with large particle numbers (10^7 particles). This condition, in combination with the use of the *Dirac* supercomputer, meant that we could run large simulations to gain good statistics without requiring large amounts of computing time on our internal systems.

Chapter 5

Precipitation fractions during LDGRF events

In the previous chapter we described the full-orbit test particle code and how it works. In this chapter we use the code to investigate energetic proton back-precipitation from CME shock heights using instantaneous injections. The results of this chapter were published in Hutchinson et al. (2022).

5.1 Modelling particle back-precipitation

We modelled the propagation of energetic protons towards the solar surface using the full-orbit test particle code with a Parker spiral field given by Equation 4.3. Equation 4.3 is known to be a good approximation down to $r \sim 2.5$ R$_\odot$ (the nominal source surface), below which more complex coronal and photospheric magnetic field are present (Owens & Forsyth 2013). In these simulations we considered a unipolar field with positive magnetic polarity (i.e. outward pointing) using the same parameters as in Marsh et al. (2013), which assumes a constant solar wind speed of $v_{sw} = 500$ km s^{-1}. Hence pitch angles in the range of $90° < \alpha \leq 180°$ correspond to sunwards propagating particles.

We simulated a 300 MeV mono-energetic proton population, instantaneously injected into a $8° \times 8°$ region, in longitude and latitude, centred on $0° \times 0°$ at a user specified radial height (the injection radius, r_i) from the centre of the Sun. We note that acceleration at the shock was not modelled and the shock was transparent to propagating particles, such that propagating particles' trajectories are not affected if they return to the position of the shock. The protons' positions within the injection region are random and the population was isotropic in velocity space at the initial time. We used a small injection region that models only a small portion of the shock. However, this small region placed at different heights can model different parts of the shock thereby allowing descriptions of different possible acceleration sites to be considered (i.e. acceleration at the flanks of the shock or nearer the nose depending on the radial height of the injection region).

Each simulation propagated particles through the magnetic field considering a constant λ. To investigate the possible shock source scenario, we ran a number of simulations that model the propagation of protons over 24 hours and involved injection regions located at radial positions in the range $r_i = 5$ R$_\odot$ to $r_i = 70$ R$_\odot$ and scattering conditions in the range $\lambda = 0.0025$ au to $\lambda = 1.0$ au. All simulations injected ten million protons.

A full test particle model of back-propagation from CME shock heights to the solar surface would require a model of the IMF, the coronal field (via a potential field source surface or MHD model) and the magnetic field close to the photosphere. Analysis of shock heights at times of γ-ray emission for LDGRF events (Section 5.4) reveals that, within the CME shock scenario, a very large part of the back-precipitation of energetic particles takes place when the source is in IP space. For this reason, in this initial investigation we focussed on the role of the IMF and we considered the Parker spiral as a first approximation. We note that the actual IMF may differ from the nominal Parker spiral and it is known that in some relativistic solar particle events earlier CMEs altered the spiral structure (e.g. Masson et al. 2012).

Where protons interact on the Sun to produce γ-rays is dependent on the local plasma density. It is generally considered that the protons would interact in the lower chromosphere or upper photosphere (Share et al. 2018; Winter et al. 2018). However, there have been studies that assumed the protons would interact at greater depths, such as the Seckel et al. (1991) study which assumed they would interact at a depth of 500 km below photosphere. In this work we have neglected this range of interaction heights as they were negligible when compared with the vast IP distances that the protons must propagate through and we assume that pion production takes place at ~ 1 R$_\odot$. The test particle code records the time and the associated particle parameters when a particle crosses the 1 R$_\odot$ boundary from larger distances. Particles that cross this boundary were regarded as absorbed and were no longer propagated. We also assumed that all particles that reach 1 $R_\odot$ go on to produce γ-rays.

5.1.1 Scatter-free mirror point radius

As charged particles propagate towards the Sun into a region of greater magnetic field strength, their pitch angle is shifted towards 90° due to the magnetic mirror effect. The particle's motion is slowed in the direction parallel to the magnetic field line and the component of velocity perpendicular to the field, $v_\perp$, increases. At the mirror point the component of velocity parallel to the field, $v_\parallel$, goes to zero and the direction of motion reverses.

For a Parker spiral magnetic field, (see Equation 4.3) and scatter-free particle propagation, it is possible to derive an expression for the radial position of the mirror point, r_{mp}, analytically given by (Hutchinson 2019),

$$r_{mp} = \frac{B_0}{B_i}\, r_0 \sin\alpha_i \left[\frac{r_0^2 \sin^2\alpha_i}{2\,a^2} + \sqrt{\frac{r_0^4 \sin^4\alpha_i}{4\,a^4} + \frac{B_i^2}{B_0^2}} \right]^{1/2}, \tag{5.1}$$

where B_i is the magnetic field strength at the starting location of the particle, at radial distance r_i, α_i is the initial pitch angle, and a is a function of initial colatitude (see Equation 4.8).

We note that all terms in Equation 5.1 involving the strength of the magnetic field are ratios at two different radial positions. Hence the mirror point radius under scatter-free conditions is independent of the magnetic field strength and depends only on the B_i/B_0 ratio.

5.1.2 Mirror point radius in the presence of scattering

The mirroring process as derived from our test particle code can be seen in Figure 5.1, where the radial distance (r, top panels), heliographic longitude (ϕ, middle panels) and the pitch angle (α, bottom panels) are displayed for the first 5 minutes of propagation for particles in two different simulations. The left panels are for a proton that propagated scatter-free and the right panels are for a proton with a scattering mean free path of $\lambda = 0.1$ au. In both simulations each proton was injected at $r_i = 20$ R$_\odot$. Scattering produces an abrupt change in trajectory by reassigning the velocity vector of the particle, altering the pitch angle (at $t \sim 3.5$ minutes and $t \sim 4$ minutes in the right panels of Figure 5.1). The changes in longitudinal position (measured in a stationary frame not corotating with the Sun) of the proton are due to drifts that occur as the proton propagates through the IMF (Dalla et al. 2013), the corotation of the system and a small curvature of the Parker Spiral. Adiabatic deceleration was negligible over the timescales depicted in Figure 5.1.

To study the effect of scattering on the mirror point radius, we simulated the propagation of a population of 300 MeV protons with mean free path $\lambda = 0.1$ au. For each proton injected into the simulation the mirror point was determined by identifying the minimum radial distance the particle reached. Figure 5.2 shows the mirror point radius, r_{mp} versus initial pitch angle α_i for the cases $r_i = 10$, 20 and 30 R$_\odot$. For clarity, only a subset of data points were plotted for each simulation. The purple, orange and green dashed lines give the scatter-free analytical value of r_{mp}, according to Equation 5.1. A number of data points were found to lie along these lines, corresponding to protons that did not scatter in the simulation, validating our code and methodology for deriving r_{mp}. The blue dashed line at 1 R$_\odot$ displays the height in the solar atmosphere that the protons must reach to go on to generate γ-rays. Data points not along the curved dashed lines correspond to protons that experienced scattering.

In Figure 5.2 there were a number of data points at or below the 1R$_\odot$ blue dashed line; these protons would be candidates to go on to produce γ-rays. It is clear from

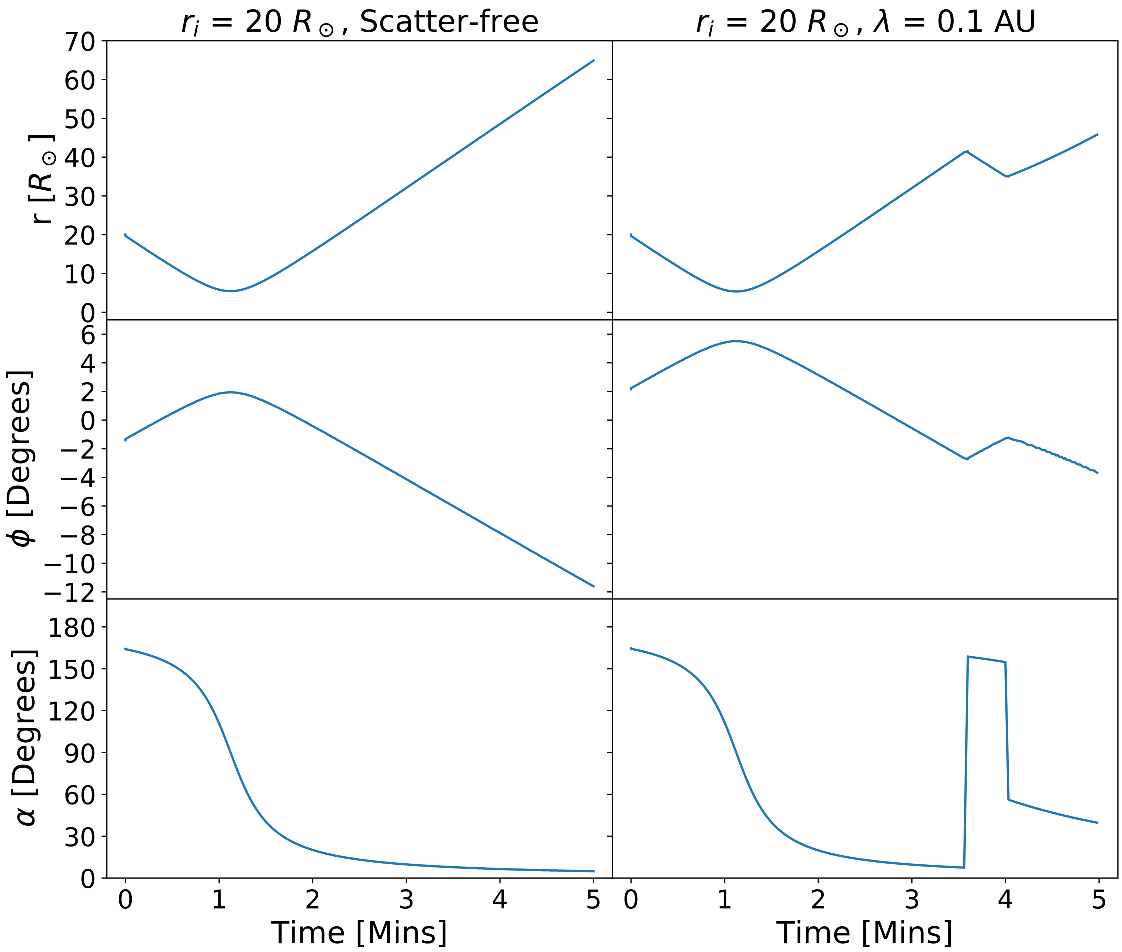

Figure 5.1: Radial position (r), heliographic longitude (ϕ) and pitch angle (α) of a 300 MeV proton for the first 5 minutes of propagation under two different scattering conditions. The left column is for a scatter-free simulation, and the right column is for a proton from a simulation with a scattering mean free path of $\lambda = 0.1$ au. Both simulations had injection at $r_i = 20\,\mathrm{R}_\odot$. Two scattering events occur in the right hand side panels at ~ 3.5 and ~ 4 minutes.

Figure 5.2 that they are a small fraction of the population. In the scatter-free case only particles in the loss cone (α_i close to 180°) reach the solar surface, while for the scattering case particles across the pitch angle distribution can reach it if scattered favourably.

Figure 5.2 shows that scattering allows the possibility for protons to propagate deeper into the solar atmosphere than they would have in scatter-free conditions (indicated by the points below the corresponding dashed line). These protons' velocity vectors have been scattered such that their pitch angles have shifted towards 180° (i.e. more field aligned). However, there were also a number of points above the scatter-free prediction, where pitch angles were shifted close to 90° (or the particle was reflected by the scattering event), resulting in the proton mirroring further from the solar surface than it would have under scatter-free conditions. The question of whether scattering primarily helps or hinders protons in their back-precipitation to the photosphere is addressed in Section 5.2.2.

5.2 Precipitation from instantaneous injection at a given injection height

For a simulation in which N particles were injected at height r_i, we define the instantaneous precipitation fraction P as the percentage of the injected population that reached r_p, $P{=}N_p/N\ \times 100$, where N_p is the number of protons that successfully precipitate. Unless otherwise specified, we study precipitation to $r_p = 1\ \mathrm{R}_\odot$. In our simulations we assume the velocity distribution to be isotropic at the location of injection. Table 5.1 gives values of N_p and P for our simulations.

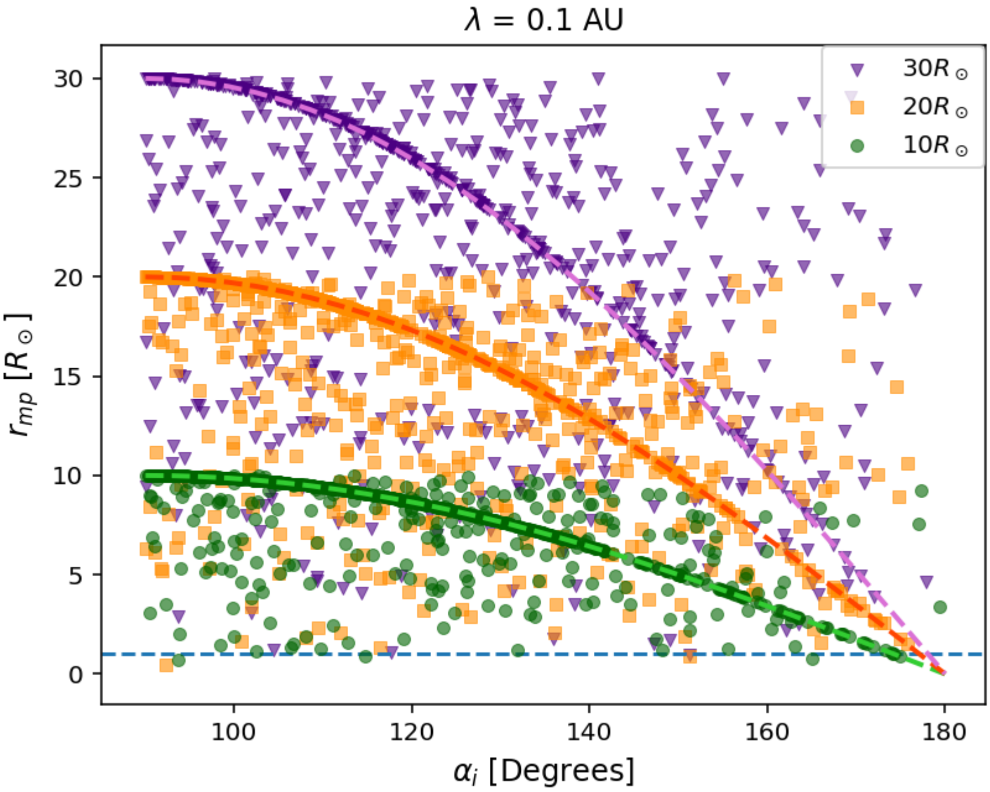

Figure 5.2: Mirror point radius, r_{mp}, versus particle initial pitch angle, α_i for simulations with injections at 10 R$_\odot$ (*green circles*), 20 R$_\odot$ (*orange squares*) and 30 R$_\odot$ (*purple triangles*) with $\lambda = 0.1$ au. The green, orange, and purple dashed lines show the analytical, scatter-free mirror point radius, given by Equation 5.1. The horizontal blue dashed line denotes the required depth in the solar atmosphere the protons must reach to generate γ-rays (1 R$_\odot$).

5.2.1 Scatter-free precipitation fraction

We first considered precipitation in the scatter-free case. In general, for an isotropic particle population propagating in a magnetic field increasing monotonically between r_i and r_p, the precipitation fraction is given by

$$P_{sf} = \frac{1}{2}\left[1 - \sqrt{1 - \frac{B_i}{B_p}}\right] \times 100 \quad (\%), \tag{5.2}$$

where B_i is the magnetic field strength at the position of injection and B_p is the magnetic field strength at the precipitation radius.

Close to the Sun the Parker spiral magnetic field can be approximated as a purely radial field (as given by Equation 4.3 with $\Omega = 0$). In this case for an isotropic proton population Equation 5.2 becomes

$$P_{sf} = \frac{1}{2}\left[1 - \sqrt{1 - \left(\frac{r_p}{r_i}\right)^2}\right] \times 100 \quad (\%), \tag{5.3}$$

where r_i is the radius of injection. Considering $r_i = 20$ R$_\odot$ and $r_p = 1$ R$_\odot$ Equation 5.3 yields $P_{sf} = 0.063\%$.

For a Parker spiral magnetic field (Equation 4.3), not necessarily close to the Sun, Equation 5.2 gives

$$P_{psf} = \frac{1}{2}\left(1 - \left[1 - \sqrt{\frac{r_i^{-4} + (ar_i)^{-2}}{r_p^{-4} + (ar_p)^{-2}}}\right]^{\frac{1}{2}}\right) \times 100 \quad (\%). \tag{5.4}$$

Considering $r_i = 20$ R$_\odot$ and $r_p = 1$ R$_\odot$ Equation 5.4 also yields $P_{psf} = 0.063\%$. We carried out scatter-free simulations with $r_i = 20$ R$_\odot$ using our model and obtained an instantaneous precipitation fraction $P = 0.062\%$ (Table 5.1) in good agreement with the analytical value.

5.2.2 Precipitation fraction in the presence of scattering

We carried out simulations with $N = 10$ million protons propagating over 24 hours in a variety of scattering conditions and derived instantaneous precipitation fractions to $r_p = 1.0$ R$_\odot$. Figure 5.3 shows P versus the scattering mean free path, λ, for injection at $r_i = 20$ R$_\odot$ (*left panel*) and $r_i = 70$ R$_\odot$ (*right panel*).

The results show that increasing the amount of scattering does help precipitation, however, in the $r_i = 70$ R$_\odot$ case it is also evident that the efficiency of precipitation decreases at very small values of λ after a peak value is reached. By running a

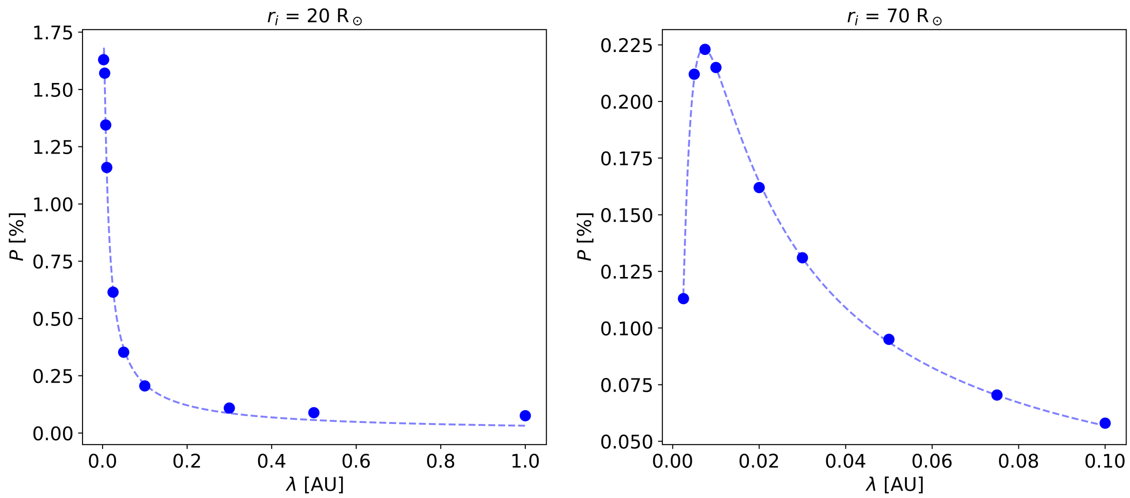

Figure 5.3: Instantaneous precipitation fraction (P) versus scattering mean free path (λ). Left panel: Instantaneous precipitation fraction (P) versus scattering mean free path λ from simulations with durations of 24 hours, where protons were injected at a height of r_i = 20 R$_\odot$, and λ ranges from λ = 0.0025 au to λ = 1.0 au. The solar wind speed is v_{sw}= 500 km s^{-1}. Right panel: P versus λ for injections at 70 R$_\odot$. Scattering mean free paths range from λ = 0.0025 au to λ = 0.1 au. Both panels were fitted with curves of the form of Equation 5.5 with the left panel having constants; a = 0.0318 au, b = 0.8287 and c = 0.0027 au, and the right panel having constants; a = 0.0094 au, b = 0.8054 and c = 0.0058 au.

simulation at very small mean free path for r_i = 20 R$_\odot$ we verified that a peak in the P profile at low λ is present also in this case.

We find that a function of the form

$$P(\lambda) = \frac{a}{\lambda^b}\ \exp\left(-\frac{c}{\lambda}\right), \tag{5.5}$$

where a, b and c are positive constants, provides a good fit to the simulation points (*blue dashed lines*).

The peak in precipitation fraction results from the fact that when the scattering becomes very strong, outward convection with the solar wind overcomes the positive effects of enhanced scattering. As confirmation of this interpretation, a function similar to Equation 5.5 can be obtained from solution of a transport equation including focussing, diffusion and convection, in the strong scattering limit (Earl 1974). From a test-particle model point of view, the peak corresponds to conditions that maximise the chances of particles scattering into the loss cone and remaining in it long enough to reach the precipitation radius. Any more scattering taking place ejects the particles from the loss cone too fast.

The position of the peak depends on injection height and solar wind speed. At larger r_i the peak is reached at a larger λ because scattering effects have more time to play a part. We found from our simulations that P depends weakly on the solar wind speed, increasing with decreasing v_{sw}, when all other parameters were kept constant. The value of λ at which P reaches a peak decreases for decreasing v_{sw}.

For r_i= 70 $R_\odot$ (*right panel*) P reaches a peak value of $P \sim 0.22\%$ at $\lambda \sim 0.0072$ au. In the case $r_i = 20$ $R_\odot$ (*left panel*), the fit indicates that the peak in precipitation fraction would be $P \sim 1.69\%$ at $\lambda = 0.0032$ au.

For medium/high values of λ (low scattering) there is a tendency for protons to precipitate soon after injection. For the high λ case this is especially important as the protons that precipitate early represent a very large percentage of the total number of successfully precipitating protons. We define F_{10min} as the percentage of the total precipitating protons over the full simulation (24 hours), N_p, that precipitate in the first 10 minutes. The last column in Table 5.1 gives F_{10min} for our simulations. For a simulation with $r_i = 20$ $R_\odot$ and $\lambda = 0.1$ au $F_{10min} \sim 69\%$. For the same injection location, when $\lambda = 0.01$ au, this drops dramatically to $F_{10min} \sim 25\%$. However, a greater number of protons than the $\lambda = 0.1$ au simulation reach the solar surface over the first 10 minutes for $\lambda = 0.01$ au because precipitation is more efficient. As expected, more turbulent magnetic fields lead to smaller F_{10min} values as protons are slowed due to more frequent scattering events. Simulations with injections close to the solar surface have high F_{10min} values, for instance $F_{10min} \sim 96\%$ for a simulation with, $r_i = 5$ R$_\odot$, $\lambda = 0.1$ au. This percentage decreases with increasing radial position of the injection region (see Table 5.1).

In addition to modelling back-precipitation to $r_p = 1$ R$_\odot$ we also ran simulations with protons propagating to $r_p = 2.5$ R$_\odot$, corresponding to the height of the source surface, from where a model of coronal and photospheric magnetic fields would need to be used to obtain a more precise estimate of precipitation fractions to the photosphere. Precipitation fractions to the source surface were found to be about 5 times larger compared to those shown in Figure 5.3.

To estimate the uncertainty on the values of precipitation fractions we utilised a bootstrapping method. We obtain one value of the precipitation fraction from each simulation, each considering $N = 10,000,000$ protons. We wrote code to create a large number (1000) of subsets of our original population of significant size (100000 particles) by randomly sampling the data set with replacement. Since the original population is large it is very unlikely that the same set will be repeated. For each subset a precipitation fraction is calculated, so that a distribution of P values is created. The standard deviation of this distribution is used as a measure of the uncertainty. The standard deviation was found to be smaller than the size of the symbols in Figure 5.3 and subsequent figures.

5.2.3 Dependence of P on injection height

Having studied the dependence of P on the scattering conditions, we focussed on a specific mean free path value, $\lambda = 0.1$ au and investigate the radial dependence of P with injection height. Figure 5.4 shows P versus r_i, characterised by a sharp decline with increasing injection height, due to the stronger magnetic mirror effect. Scattering results were compared with the scatter-free curve (*blue line*).

The simulation points can be fit by

$$P(r_i) = 31.084 \left(1 - \left[1 - \sqrt{\frac{(r_i^{-2.990} + a^{-2} r_i^{0.035})}{(r_p^{-4} + (ar_p)^{-2})}}\right]^{1/2}\right), \quad (\%) \tag{5.6}$$

where r_i is in solar radii. Note that Equation 5.6 implicitly includes two constants of unity that have units of $\mathrm{R}_\odot^{-1.010}$ and $\mathrm{R}_\odot^{-2.035}$ that multiply the r_i terms in the numerator of the fraction. These constants are required to maintain $P(r_i)$ as a dimensionless quantity. The exponents of the r_i terms, as well as the coefficient (31.084), have been determined using a least squares fitting routine in python to the green data points in Figure 5.4. As the shock-source propagates from 5 to 70 $\mathrm{R}_\odot$ the precipitation fraction from our simulations drops from 1.450% to 0.058%. This corresponds to a drop in the number of protons reaching the solar surface by a factor of $\sim$ 25 assuming a radial injection function that is constant with r_i.

Equation 5.6 is a proxy for the temporal evolution of the instantaneous precipitation fraction. Depending on its speed, each CME-driven shock will cover the range of radial distances in Figure 5.4 over timescales that are unique to that event. Hence, the shock-height versus time curve determines the temporal evolution of the instantaneous precipitation fraction.

5.3 Evaluation of emission region features

In Figure 5.5 the locations where the protons crossed the 1 $\mathrm{R}_\odot$ boundary are displayed for two particle energies (300 MeV (top panels) and 1 GeV (bottom panels)) and scattering mean free paths of $\lambda = 0.1$ au (panels a and c) and $\lambda = 0.01$ au (panels b and d) in a coordinate system corotating with the Sun. The red square is the region of the photosphere directly connected to the injection region. All simulations had injections located at $r_i = 20$ $\mathrm{R}_\odot$.

In Figure 5.5 panels a) and c) there is a systematic drift of the crossing position southwards with time. The same trend is seen in Figure 5.5 panels b) and d).

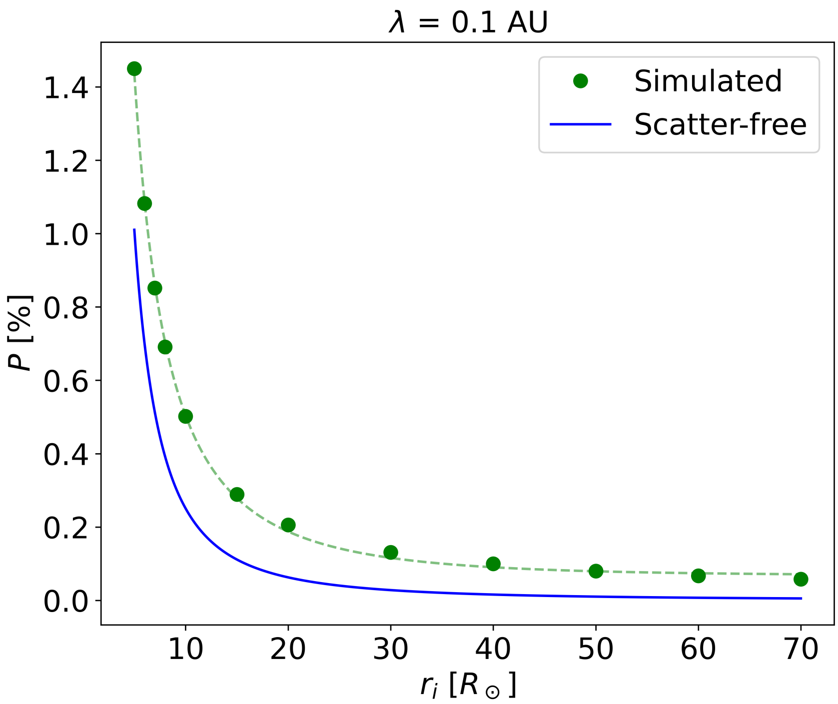

Figure 5.4: Instantaneous precipitation fraction (P) versus radial location of injection (r_i) for scattering described by a mean free path $\lambda = 0.1$ au. The points have been fitted with the line described by Equation 5.6, and the blue curve represents scatter-free precipitation according to Equation 5.4.

r_i [R$_\odot$]	λ [au]	N_p	P [%]	F_{10min} [%]
5	0.1	144978	1.450	95.6
6	0.1	108200	1.082	94.2
7	0.1	85170	0.852	92.4
8	0.1	69082	0.691	90.8
10	0.1	50222	0.502	87.2
15	0.1	28900	0.289	78.2
20	0.1	20614	0.206	69.2
25	0.1	15294	0.153	59.6
30	0.1	13086	0.131	52.5
40	0.1	9950	0.100	39.9
50	0.1	8048	0.080	28.2
60	0.1	6647	0.066	19.0
70	0.1	5798	0.058	12.7
20	0.0025	162987	1.630	2.0
20	0.0050	157126	1.571	10.0
20	0.0075	134501	1.345	17.8
20	0.01	115851	1.159	24.5
20	0.025	61459	0.614	45.8
20	0.05	35324	0.353	58.7
20	0.3	10891	0.109	82.7
20	0.5	8903	0.089	87.2
20	1.0	7514	0.075	93.5
20	Scatter-Free	6224	0.062	100.0
70	0.0025	11317	0.113	0.0
70	0.0050	21234	0.212	0.0
70	0.0075	22318	0.223	0.0
70	0.01	21548	0.215	0.0
70	0.02	16219	0.162	0.1
70	0.03	13130	0.131	0.9
70	0.05	9481	0.095	4.0
70	0.075	7061	0.070	8.2

Table 5.1: Instantaneous precipitation fractions for our simulations. Columns are: (From left to right) The radial height of the shock at particle injection (r_i), the parallel scattering mean free path (λ), the number of precipitating protons that reach 1 R$_\odot$ over the full 24 hour simulation (N_p), the instantaneous precipitation fraction (P), and the percentage of the precipitating protons that reach the solar surface in the first 10 minutes after injection (F_{10min}). All simulations injected a 300 MeV mono-energetic proton population consisting of N = 10 million protons into an $8° \times 8°$ injection region.

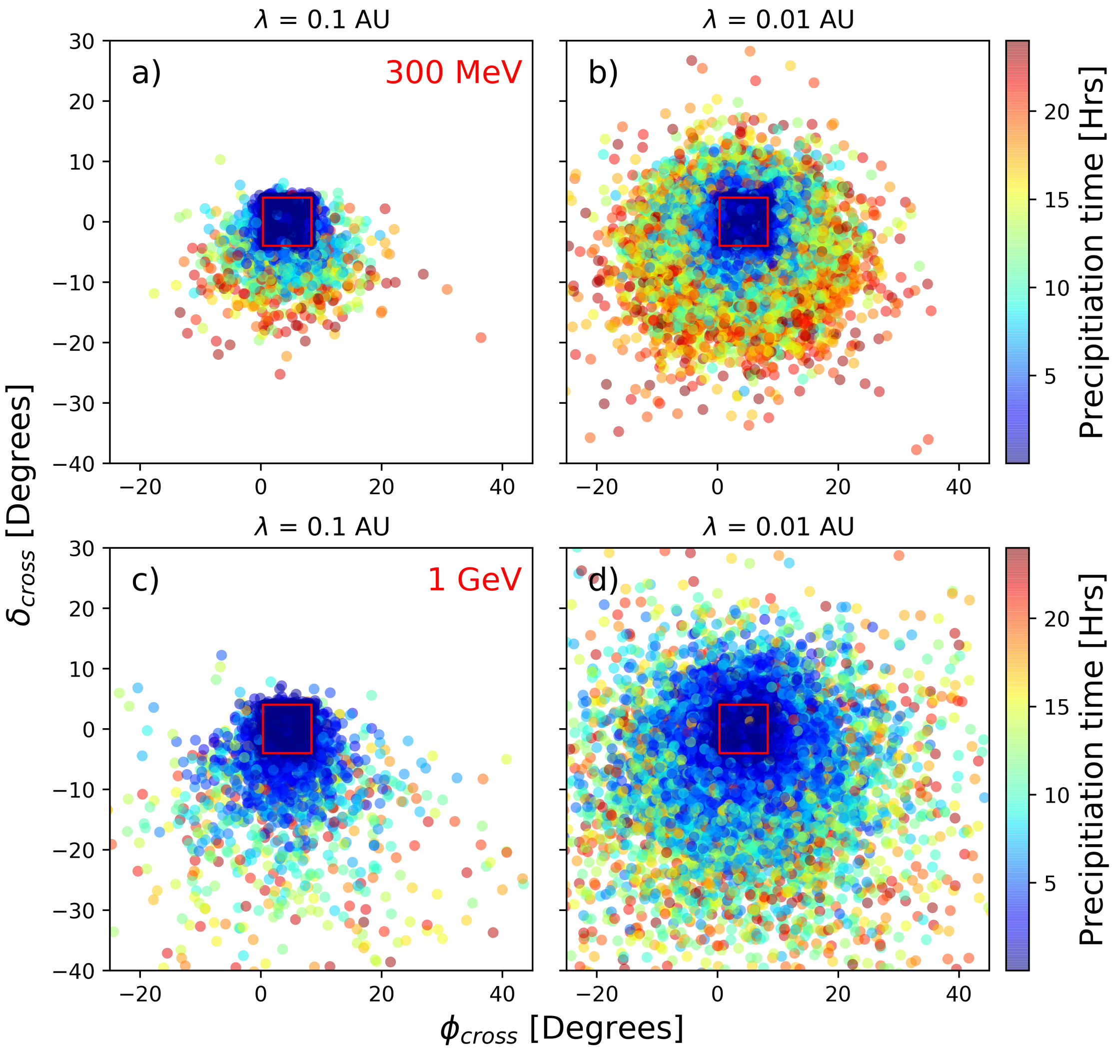

Figure 5.5: Heliographic latitude (δ_{cross}) and longitude (ϕ_{cross}) of the locations where energetic protons reach the solar surface for simulations with; an 8° × 8° injection region (centred at 0°, 0°) at r_i = 20 R$_\odot$ and λ= 0.1 au (panels a and c) and 0.01 au (panels b and d). Panels a) and b) are for a 300 MeV mono-energetic proton population, while c) and d) are for a 1 GeV population. The red box denotes the region on the solar surface that maps to the injection region. All panels are displaying -40 to 30 degrees in latitude and -25 to 45 degrees in longitude. The crossing positions of the 1 GeV simulations extend beyond these limits with particles in the λ = 0.01 au simulation crossing 1 R$_\odot$ between -82.5 to 97.6 degrees in longitude and between -79.1 and 67.3 degrees in latitude.

However, some crossings were also observed northwards of the emission region. The southward drift is due to gradient and curvature drifts associated with the Parker spiral magnetic field (Dalla et al. 2013). For our magnetic polarity this leads to a southward drift; however, in the opposite magnetic polarity these drifts would be northwards. In addition, finite Larmor radius effects associated with scattering events produce motion of the guiding centre perpendicular to the magnetic field. The finite Larmor radius effects were more prominent in the $\lambda = 0.01$ au panels and they were the cause of the northward displacement. We note that the finite Larmor radius effects do not have a preferential direction unlike the drifts. They were expected to be more prominent in the more magnetically turbulent simulations as the proton can shift up to 2 Larmor radii per scattering event and there were more scattering events in these simulations.

The longitudinal and latitudinal positions of the protons reiterate that they do not propagate solely along the Parker spiral lines they were initially accelerated on. Therefore, drifts and finite Larmor radius effects are not negligible when determining if protons from the shock are responsible for the observed position of the γ-ray emission region on the solar disc, especially in the high scattering case. Importantly, magnetic connection to the shock should be treated as a guide and not a representative trajectory of these energetic particles. Higher-energy protons show stronger deviations from their original Parker spiral field lines, even for earlier precipitating protons, due to the increase in drifts and finite Larmor radius effects with increasing particle energy. This is clear when comparing panels c) and d) with panels a) and b) in Figure 5.5.

When considering injections at larger radial distances we found that, as expected, the emission region moves westwards. This occurs as the CME-driven shock propagates to larger radial distances it injects particles onto Parker spiral lines with footpoints located increasingly westwards on the photosphere.

We note that we have only considered a unipolar Parker spiral magnetic field. Positions on the solar disc are likely to be altered by the more complex coronal magnetic field structure.

5.4 Shock heights during LDGRF events

We now apply the results of our simulations to a set of eight specific LDGRF events: the subset of events from the Winter et al. (2018) study with a >2 hour duration. These events are listed and discussed further in section 5.5 (see Table 5.2). They were associated with CMEs with plane-of-the-sky speeds ranging from 950 to 2684 km s^{-1} based on the Coordinated Data Analysis Workshops (CDAW [1]) catalogue of observations by the Large Angle and Spectrometric Coronagraph (LASCO) on board the Solar and Heliospheric Observatory (SOHO).

For each of the eight LDGRF events we estimate the position of the shock at the time of peak and end γ-ray emission, using CME data and a series of approximations. We assumed that the shock height and speed coincide with those of the associated CME and that all parts of the shock propagate radially. We used the linear fit in the CDAW catalogue to determine height versus time for $r < 30\ \mathrm{R}_\odot$. At larger distances we used the empirical expression of Gopalswamy et al. (2001) to describe the shock's acceleration (or deceleration), a_{sh}, during the propagation to 1 AU:

$$a_{sh} = 2.193 \,-\, 0.0054\, v_{sh}, \tag{5.7}$$

where a_{sh} is in m s^{-2} and v_{sh} is the shock speed in km s^{-1}. According to this equation shocks faster than ~ 406 km s^{-1} decelerate. All the shocks listed in Table 5.2 were significantly faster than this and so decelerate during their propagation. To obtain the peak times of the γ-ray emission we used data from Table 3 of Share et al. (2018) and the corresponding plots in their Appendix C, and for the end times

[1] https://cdaw.gsfc.nasa.gov/CME_list/halo/

we used data from Table 1 of Winter et al. (2018).

For the eight LDGRF events the shock positions at the peak and end times of the γ-ray emission were plotted in Figure 5.6 as circles and squares respectively. Here the shaded wedges span 500 km s^{-1} increments in constant shock speed from 500 to 3000 km s^{-1}. For the 2012 March 7 event, which was associated with two fast CMEs erupting in rapid succession, data points for both (with speeds of 2684 km s^{-1} and 1825 km s^{-1}, respectively) were plotted. While the absence of interplanetary type III radio emissions during the second, much slower CME suggests that it was unlikely to be associated with the SEP event at 1 au (see Richardson et al. 2014), a direct contribution to particle acceleration cannot be ruled out, so both CMEs were considered.

Figure 5.6 shows that if the CME-driven shock was the source of the γ-ray emission in the LDGRF events, back-precipitation from large distances needs to have taken place. The median position of the shock at the end time is $\sim$ 71 R$_\odot$ (including both shocks that originated on 2012 March 7). For the 2012 March 7 event the two associated shocks were located at $\sim$ 242 R$_\odot$ and $\sim$ 155 R$_\odot$ at the end time of the γ-ray emission, which lasted for 19.5 hours.

5.5 Total precipitation fraction

In this Section we combine our simulation results for the instantaneous precipitation fraction as a function of r_i (as summarised in Figure 5.4) with the information on shock height versus time for LDGRF events to obtain an upper limit estimate, $\overline{P}$, of the total precipitation fraction in the events, within the CME shock scenario. We calculate $\overline{P}$ as

$$\overline{P} = \frac{\displaystyle\int_{r_{ini}}^{r_{fin}} N(r_i)P(r_i)\,dr_i}{\displaystyle\int_{r_{ini}}^{r_{fin}} N(r_i)\,dr_i} \quad (\times 100\,\%), \tag{5.8}$$

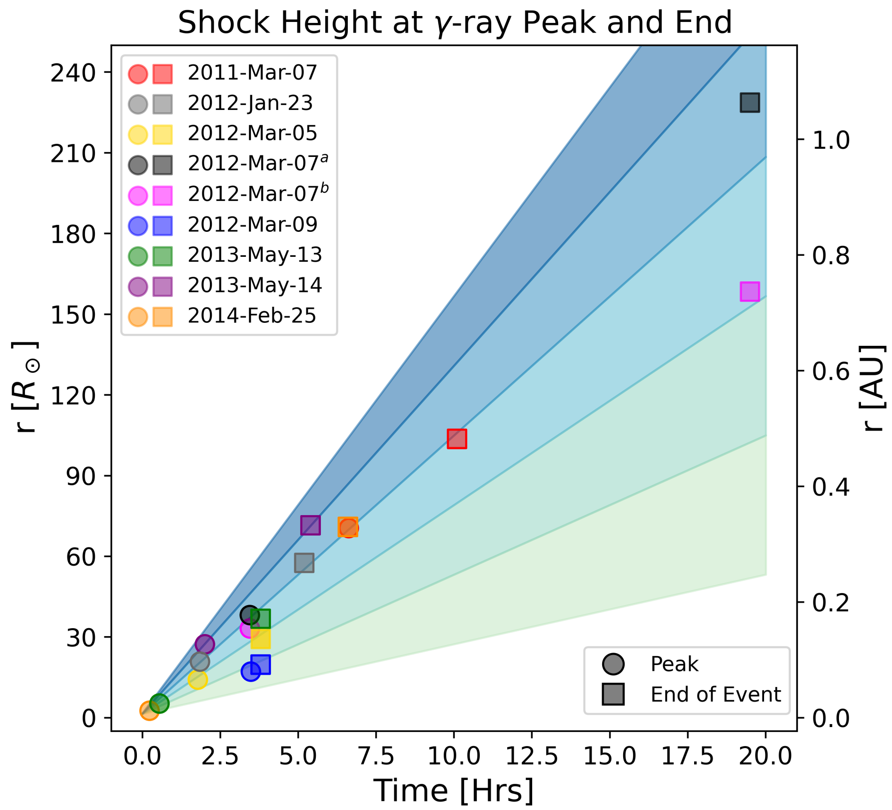

Figure 5.6: Radial distance, r, from the centre of the Sun of CME-driven shocks associated with LDGRFs at the peak times (*circles*) and end times (*squares*) of detected γ-ray emission. Constant deceleration is assumed during propagation, as given by Equation 5.7, and initial plane-of-the-sky speeds were taken from the SOHO/LASCO CME catalogue. Each shaded wedge spans 500 km s^{-1} increments in radial shock speed between 500 and 3000 km s^{-1}. For the 2012 March 7 event we show two sets of radial positions for two different CME-driven shocks that day: 2012-Mar-07^a is the earlier, faster CME with a speed of 2684 km s^{-1} and 2012-Mar-07^b is the second, slower CME with a speed 1825 km s^{-1}.

where $P(r_i)$ describes the radial evolution of the instantaneous precipitation fraction (Equation 5.6), $N(r_i)$ the number of injected particles as a function of radial distance (injection function), r_{ini} the radial position of the shock when particle acceleration begins, and r_{fin} the position when particle acceleration ends. Hence, $\overline{P}$ is the ratio of the total number of precipitating and injected protons over the event.

For $P(r_i)$ we make use of the fit of the curve in Figure 5.4 (Equation 5.6), corresponding to scattering conditions described by $\lambda = 0.1$ au, (i.e. strong scattering). We used a simple model for the injection function given by

$$N(r_i) = \left(\frac{A}{(r_i - r_{ini})}\right)^B \exp\left(-\frac{C}{(r_i - r_{ini})}\right), \tag{5.9}$$

where A, B and C are positive constants. This functional form describes a fast rise phase to peak injection, then a turnover and subsequent slow decay, describing the fact that energetic particles are more efficiently accelerated when the shock is closer the Sun. In particular, in the scatter-free hypothesis and the CME shock acceleration scenario the highest-energy particles associated with Ground Level Enhancements are thought to typically be released at shock heights of 2-4 $R_\odot$ (Reames 2009; Gopalswamy et al. 2013a).

To calculate $\overline{P}$ we need to specify r_{ini} and r_{fin} in Equation 5.8. Conservatively, we assume that particle acceleration begins at the radial position of the formation of the shock. Gopalswamy et al. (2013b) determined the median shock formation height of 1.20 $R_\odot$, which we considered as a possible estimate for r_{ini}. We estimate r_{fin} by calculating the shock position at the time when the γ-ray emission ends (based on the observed durations). The values of r_{fin} for the LDGRF events are shown in column 4 in Table 5.2 and plotted in Figure 5.6.

5.5.1 Influence of injection function on precipitation

Figure 5.7 shows the effect of injection function shape on $\overline{P}$. Here $N(r_i)$ for different values of A, B and C and a fixed radial position of peak injection, $r_{peak} = 5.0$ $R_\odot$ are shown. The injection functions are normalised so that the total number of injected particles was the same for different curves. The right panel of Figure 5.7 displays the corresponding total precipitation fractions, determined using Equation 5.8, where

Date	v_{sh} [km s^{-1}]	C2 t [UT]	D [hr]	r_{fin} [R$_\odot$]	$\overline{P}$ ($r_{ini} = 1.20R_\odot$) [%]
2011-Mar-07	2125	20:00:05	10.1	103.6	0.603
2012-Jan-23	2175	04:00:05	5.2	57.5	0.667
2012-Mar-05	1531	04:00:05	3.6	29.2	0.800
2012-Mar-07^a	2684	00:24:06	19.5	228.6	0.555
2012-Mar-07^b	1825	01:30:24	19.5	158.4	0.574
2012-Mar-09	950	04:26:09	3.8	19.7	0.932
2013-May-13	1850	16:07:55	3.8	36.7	0.745
2013-May-14	2625	01:25:51	5.4	71.5	0.640
2014-Feb-25	2147	01:25:50	6.6	70.9	0.640

Table 5.2: Total precipitation fractions over the full duration of the eight LDGRF events plotted in Figure 5.6. Columns are: (From left to right) The date of the LDGRF event, the speed of the shock associated with the CME (v_{sh}), the time of CME first appearance in the LASCO C2 field of view; obtained from the SOHO/LASCO CME catalogue, the duration of the detected γ-ray emission from the *Fermi* LAT instrument (D); obtained from Table 1 of Winter et al. (2018), the position of the shock at the end time of detected γ-ray emission of the event (r_{fin}); determined using Equation 5.7, and the total precipitation fraction ($\overline{P}$) over the propagation of the shock from r_{ini} (1.20 R$_\odot$, the median shock formation height as determined by Gopalswamy et al. 2013b) to r_{fin}; determined using Equation 5.8. The total precipitation fraction considers the fact that the instantaneous precipitation fraction decreases with the radial dependence as shown in Figure 5.4 and assumes that the scattering can be described by $\lambda = 0.1$ au. There were two CMEs associated with the 2012 March 7 event, consequently 2 shocks were formed. CME *a* entered the LASCO C2 field of view at 00:24:06 UT and was associated with a X5.4 flare; the second CME, *b*, entered the LASCO C2 field of view at 01:30:24 UT and was linked to a X1.3 flare.

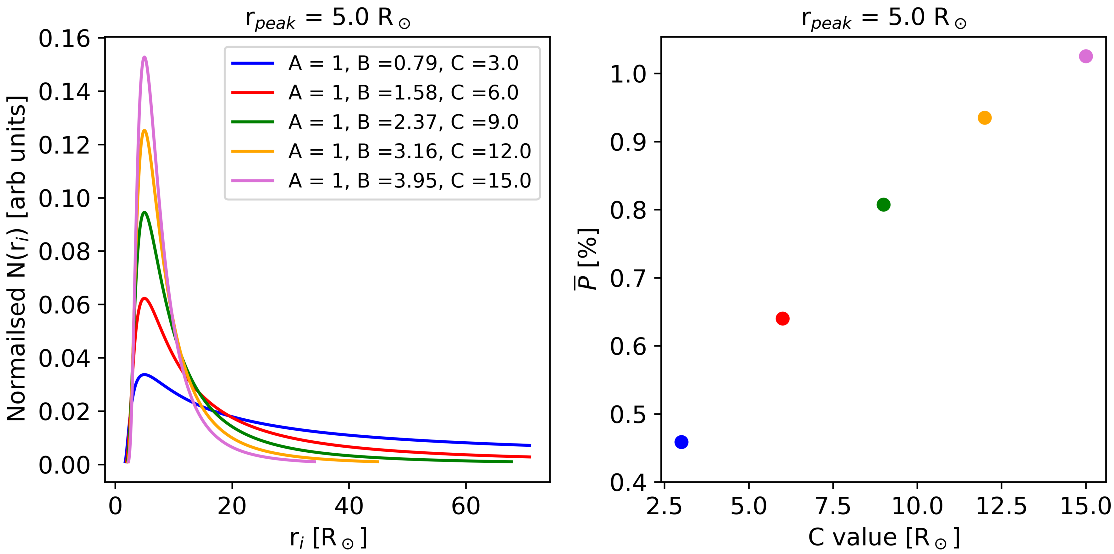

Figure 5.7: Normalised injection functions (*left panel*) with peak injection at 5.0 R$_\odot$ and differing decay rates versus the radial position of the shock, r_i. Only values of $N(r_i) > 0.001$ were plotted for clarity. The corresponding total precipitation fraction ($\overline{P}$, *right panel*) versus the value of the constant C. Each coloured point in the right panel represents $\overline{P}$ for the same coloured curve in the left panel, calculated using $r_{ini} = 1.20$ and $r_{fin} = 70.91$ R$_\odot$, for $\lambda = 0.1$ au.

each coloured point represents the $\overline{P}$ of the same coloured curve in the left panel. Here we used $r_{ini} = 1.20$ R$_\odot$ and $r_{fin} = 70.91$ R$_\odot$, the latter being the median end time position of the shocks of Table 5.2.

We note that for a delta function injection the total precipitation fraction is the same as the instantaneous precipitation fraction given by Equation 5.6. It is clear from Figure 5.4 that the further from the Sun particles are injected the harder it is for them to back-precipitate. Therefore, the more sunwards the injection function is skewed the larger the total precipitation fraction is (i.e. peak injection occurring closer to the Sun leads to higher $\overline{P}$ and extended injections reduce $\overline{P}$). This is identifiable by comparing the blue and pink/purple injection functions and their corresponding $\overline{P}$ in Figure 5.7. The blue and pink/purple injection functions in the left panel have total precipitation fractions of 0.459% and 1.025%, respectively. The extended decay phase of the blue curve skews the injection further from the Sun where the efficiency of the back-precipitation is low, resulting in the lower total precipitation fraction.

Figure 5.7 shows that for large total precipitation fractions a prompt injection close to the solar surface is required. However, this will result in shorter durations of γ-ray emission. Conversely, injections extended over large radial distances will provide longer durations of γ-ray emission at the expense of the total precipitation fraction. Therefore, large precipitation fractions and long durations of γ-ray emission cannot be reconciled using the CME-driven shock acceleration scenario.

5.5.2 Total precipitation fraction for eight LDGRF events

We calculated $\overline{P}$ from Equation 5.8 using an injection described by Equation 5.9 with $A = 1.0$ R$_\odot$, $B = 1.58$ and $C = 6.0$ R$_\odot$, corresponding to the red curve in Figure 5.7. These values were chosen as large C values led to injections that were effectively shortened in r as the majority of the population is injected near the peak and experiences rapid decay afterwards (such as the pink/purple curve in Figure 5.7). The low C injections (like the blue curve in Figure 5.7) did not have a significant enough peak and had a decay that lasted for much longer than required. Note that B was calculated using the value of C and r_{peak} using the relation $B = C/(r_{peak} - r_{ini})$. We used the same r_{peak} and r_{ini} values and so the value of B is tied directly to the value of C. The parameter A was set to 1.0, another value could have been used but the effects of this would have been undone during normalisation of the distribution. The injection was normalised such that the same number of particles were considered for each injection. The values for $\overline{P}$ we obtained are displayed in the final column of Table 5.2, corresponding to $r_{ini} = 1.20$ R$_\odot$, for the eight LDGRF events. These values are small, ranging from $\overline{P} \sim 0.56\%$

to $\sim 0.93\%$, with the smallest $\overline{P}$ values associated with the events with the fastest shocks or longest durations. As indicated by Figure 5.7 if the injection was more prompt (like the pink/purple curve in Figure 5.7) then larger $\overline{P}$ values are possible. Similarly, if the injection was more sunwards-skewed the $\overline{P}$ values would increase further. We considered the effect of an injection with $r_{peak} = 3.0$ R$_\odot$, keeping all parameters the same, and $\overline{P}$ increased to ~ 2 %.

The total precipitation fraction of the event, $\overline{P}$, becomes smaller if acceleration at the CME shock continues over larger distances, as can be seen from Table 5.2 considering the events with the largest values of r_{fin}. Typically these are the events with very long durations, very fast shocks or both. Looking at the two shocks associated with the 2012 March 7 event one can see that having a slower shock over the same duration will lead to an increased $\overline{P}$. We note that if the proton acceleration occurs at the flanks of the shock this would increase the $\overline{P}$ as they remain closer to the solar surface than the shock nose. However, higher-energy particles are believed to be more efficiently accelerated over a small shock region around the nose (Zank et al. 2006; Hu et al. 2017).

5.6 Time profiles of proton back-precipitation

The test particle simulations described in Section 5.2 have considered injection at a single radial position, rather than a moving shock. To derive information about how precipitation evolves over time, we also carried out a test-particle simulation with moving shock-like injection, as described in chapter 4. We considered a shock with radial speed of 2684 km s^{-1} at 1.2 R$_\odot$ that injects particles over the radial distance range 1.2 - 228.6 R$_\odot$ and follows the injection function given in Equation 5.9 with $A = 1.0$ R$_\odot$, $B = 1.58$ and $C = 6.0$ R$_\odot$. This injection approximates the injection for the fastest shock in the 2012 March 7 event, with the acceleration of energetic protons occurring over 19.5 hours. We assume constant shock deceleration

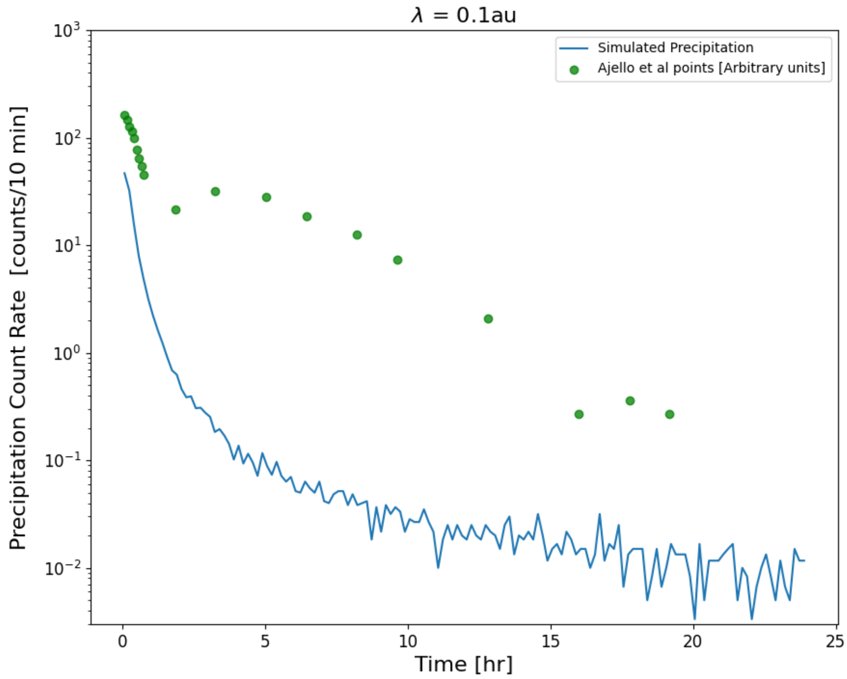

Figure 5.8: Precipitation count rate versus time from a simulation with injection from a moving shock-like source with the same speed as the fastest 2012 March 7 shock (*blue line*), at 10 minute resolution. The radial profile of particle injection is given by Equation 5.9 with A = 1.0 R$_\odot$, B = 1.58 and C = 6.0 R$_\odot$. Green data points show the time evolution of the γ-ray emission, from Ajello et al. (2014).

as described in Section 5.4.

The time profile of precipitation can be seen in Figure 5.8. Data points from Fermi/LAT showing the time evolution of the γ-ray emission are also shown. It can be seen that even for an extended injection, in the simulations the majority of back-precipitation takes place early. The rapid decay in precipitation highlights the significant challenge that magnetic mirroring poses to back-precipitating protons.

As can be seen from Figure 5.8, the precipitation drops by over two orders of magnitude within ~5 hours, even though injection continues for many hours beyond this. According to the γ-ray profile for the 2012-03-07 event (Ajello et al. 2014), the detected γ-ray emission drops by only $\sim$2 orders of magnitude over the 19.5 hour duration of the LDGRF event. Our simulation considers the fastest shock associated with the 2012-03-07 LDGRF event. We also considered the contribution from the slower second shock (not displayed in Figure 5.8), where we find that it decays much faster than the decay of the observed γ-ray profile. Figure 5.8 is very similar to the figure in Hutchinson et al. (2022), but the modelled line has a less fast decay due to an error connected with the time normalisation in the code, which has been corrected in Figure 5.8. The differences between the figure in Hutchinson et al. (2022) and Figure 5.8 are minimal, and do not alter the main conclusions. From the simulation of Figure 5.8 a total precipitation fraction of $\overline{P} = 0.743\%$ is obtained, similar to the value from the analytical expression (Equation 5.8) shown in Table 5.2 for the 2012-03-07a event.

5.7 Discussion and conclusions

Energetic (>300 MeV) proton back-propagation from CME heights down to the solar surface is strongly impeded by magnetic mirroring. In this chapter we investigated whether scattering associated with turbulence may aid back-precipitation to the levels required to explain LDGRFs via the CME shock scenario, by ensuring that more particles enter the loss cone. We investigated the problem extensively using 3D test particle simulations with varying levels of scattering.

Particles accelerated at a CME-driven shock may back-precipitate via a number of different routes. There might be the possibility of almost scatter-free trajectories or propagation might be strongly influenced by the scattering behind the shock. In some cases back-precipitation from the flanks may be involved. We found that compared to the scatter-free case, scattering does enhance particle precipitation. For example, for injection at $r_i = 20$ R$_\odot$ it increases the instantaneous precipitation fraction P from 0.06% (scatter-free) to 0.21% for a mean free path $\lambda = 0.1$ au.

Increasing the level of scattering further improves the precipitation fraction, for example $\sim P$=1.63 % when λ = 0.0025 au. There is, however, a limit to this increase because when the scattering mean free path becomes very small outward convection with the solar wind becomes very efficient and particles can no longer back-precipitate (as shown in Figure 5.3). The value of the mean free path at which this effect becomes significant is dependent on injection height and solar wind speed. In our simulations the convection effect becomes important for mean free paths below 0.0072 au for r_i = 70 R$_\odot$ and below 0.0032 au for r_i = 20 R$_\odot$.

Some studies in the literature have assumed very strong scattering conditions behind the shock, for shock heights up to $\sim$ 10 R$_\odot$. For example, Afanasiev et al. (2018) used a model where λ increases from 0 at the shock front up to a maximum value λ_0 at the Sun, where λ_0 varies in the range $0.16 \leq \lambda_0 \leq 3.2$ R$_\odot$ ($\sim 0.0007 \leq \lambda_0 \leq\sim 0.015$ au) across different simulations. Jin et al. (2018) suggest that a mean free path of the order of 1 R$_\odot$ ($\sim$ 0.0047 au) is sufficient to overcome the strong magnetic mirroring that occurs close to the Sun. While this may be the case very close to the Sun, our results show that when the shock is further out very small mean free paths impede back-propagation via the outward convection effect. When shock locations further from the Sun are considered very low mean free path values are probably unrealistic. If the scattering were very strong all the way from the shock to the corona, many hours after CME liftoff, one would expect to observe a long lasting increase in SEP fluxes after the passage of the CME driven shock at a near-Sun spacecraft. To our knowledge this has never been seen, for instance in data from the Helios 1 and 2 spacecraft (e.g. Kallenrode 1993). It is hoped that new data from *Parker Solar Probe* and *Solar Orbiter* will provide additional information on this question. When studying total precipitation fractions (Section 5.5) we assumed λ=0.1 au, similar to typical mean free paths that have been derived by fits of GLE measurements, due to >500 MeV protons (e.g. λ = 0.27 au used by Bieber et al.

2002).

Overall, even in the presence of scattering, back-precipitation is generally highly inefficient, with instantaneous precipitation fractions being below 2% in our simulations. P decreases strongly with height of injection, r_i (Figure 5.4) because of this proton injection at large radial distances cannot meaningfully extend the precipitation on the solar surface.

It is also possible to use the results of our simulations, specifically the radial dependence of instantaneous precipitation, to estimate an upper limit $\overline{P}$ to the total precipitation fraction within the CME shock scenario. Using a variety of idealised injection functions we have shown that when the acceleration takes place over a broad range of radial distances, for example in the case of very fast shocks, lower values of $\overline{P}$ are obtained. When $\overline{P}$ was calculated for eight solar eruptive events that resulted in LDGRFs the values obtained range from $\sim 0.56\%$ to $\sim 0.93\%$, with the smallest values corresponding to events with the fastest shocks and longer durations. This is because the shocks for these events spend less time close to the solar surface, where the precipitation is efficient. The radial position of initial particle injection (r_{ini}) has a substantial effect on the total precipitation fraction. All the events analysed were associated with fast CME-driven shocks: a shock with the average speed of our subset of events could reach 70 $R_\odot$ in less than 6.7 hours. The fastest shock would cover this distance in ~ 5 hours.

de Nolfo et al. (2019) used observations to directly compare the number of protons interacting at the Sun, N_{LDGRF}, with the number of SEP protons at 1 au, N_{SEP} . From N_{LDGRF} and N_{SEP} they calculated a lower limit on the total precipitation fraction required for the validity of the CME shock scenario, in which the two populations have a common origin. They found that precipitation fractions greater than 10% were required in the majority of the 14 events considered, as shown by their Figure 8. For the 2011 March 7 and 2012 January 23 events they reported that a >90% precipitation fraction is required by the CME scenario. Our modelling of the same events found values more than two orders of magnitude smaller, with $\overline{P} \sim 0.60$ % and ~ 0.67 %, respectively. The small value ($\sim 2.9\%$) they obtained for the 2014 February 25 event is approximately a factor of 4.5 greater than our estimate ($\sim 0.64\%$). In the case of the 2012 March 7-10 events, since it was not possible to evaluate the individual contributions in terms of SEP intensities at 1 au, they provided a single precipitation fraction value of $\sim 18\%$, which exceeds by at least 19 times the values that we calculated for three CMEs on 2012 March 7 - 9 considered in this work (~ 0.56 - 0.93%); similar results are expected for the 2012 March 10 CME, characterised by an intermediate speed. Overall we conclude that while in many events the direct observational comparison between the interacting and SEP populations gives rise to a requirement of large precipitation fractions under the assumption of CME shock acceleration of both populations (de Nolfo et al. 2019), for the same events our modelling cannot produce them due to the strong effect of magnetic mirroring. This poses a problem for the CME shock hypothesis for LDGRFs.

The shock speeds used to calculate the $\overline{P}$ values were based on the plane-of-the-sky CME speeds averaged over the LASCO field of view (2-32 $R_\odot$). Therefore, they underestimate the CME velocities close to the Sun and, in general, the corresponding space (3D) speeds due to projection effects, especially for events originating far from the solar limb. Consequently, derived total precipitation fractions are expected to be overestimates. However, their values remain very small even with these assumptions.

In order to obtain larger precipitation fractions from our model for the eight LDGRF events we would have to choose the injection function with fastest rise and shortest decay phase (i.e. tending towards a delta function injection at the radial position of peak injection - an instantaneous injection), but the result of this would be a reduction in the overall duration of precipitation. Even with this choice of injection function $\overline{P}$ would overall still remain smaller than 1.5% (for our peak injection at 5.0 $R_\odot$, see Table 5.1).

Our simulations also show that with increasing radial distance of injection the emission region on the solar surface moves westwards. Particles that precipitate early in time after injection tend to follow Parker spiral magnetic field lines, but with increasing propagation time the protons deviate due to drifts and finite Larmor radius effects. This deviation becomes larger with increasing particle energy (Figure 5.5).

Our estimates of the proton precipitation count rate due to the first shock in the 2012 March 7 event (Figure 5.8) decays rapidly, and contributions towards the precipitation quickly fall orders of magnitude indicating that γ-ray production due to the back-precipitation of energetic protons from a CME driven-shock is inconsistent with the long duration of the observed γ-ray profiles for $\lambda = 0.1$ au.

In summary the above results present a challenge to the CME shock acceleration scenario for LDGRFs as follows:

- Long after the eruptive event, CME shocks are very far from the solar surface and back-precipitation is extremely difficult. A faster CME shock only exacerbates this problem.

- The total precipitation fraction, $\overline{P}$, values obtained in our study were typically smaller than 1.5%, while work by de Nolfo et al. (2019) has indicated that in several LDGRF events a much larger value of $\overline{P}$ is required for the validity of the CME shock scenario.

- Time-extended acceleration and large total precipitation fractions cannot be reconciled according to our simulations. A model of an event that makes the duration of the acceleration longer will result in smaller total precipitation fractions.

- The specific shape of the precipitation count rate versus time obtained from our simulations displays a much faster decay than that observed in LDGRF intensity profiles (Figure 5.8).

In our simulations 300 MeV protons were considered. However, we do not expect a significant difference in total precipitation fractions for higher-energy particles as scattering depends on energy only weakly and the magnetic mirror effect does not depend on particle energy.

Chapter 6

SEP intensity and anisotropy profiles for a shock-like particle injection

6.1 Introduction

In this chapter we present results from 3D test particle simulations in which, for the first time, particle injection is from a moving shock-like source. This means that it is spatially extended over a wide shock and temporally extended since particles keep being injected as the shock propagates though the heliosphere. This new injection considers the simple model of a shock described in chapter 4, similar to that developed by Heras et al. (1994) and Kallenrode & Wibberenz (1997), and provides a first step in accounting for temporally extended particle injections in 3D full-orbit test particle simulations.

We investigate the effect of choosing different radial and angular injection profiles on the intensity and anisotropy profiles at 1 au for different observers. We study the effect of a variety of IP scattering conditions on observables. We compare intensity and anisotropy profiles for observers at 0.3 and 1.0 au, to provide comparisons with *Parker Solar Probe* and *Solar Orbiter* observations.

The results in this chapter have been published in Hutchinson et al. (2023b).

6.2 Shock-like injection simulations

For this work we utilise a shock-like injection, as described in section 4.3, using the same parameters as those shown in Table 4.2, corresponding to a shock with a constant velocity $v_{sh} = 1500$ km/s propagating radially for two days, with a 70° angular width in both latitude and longitude.

We conducted simulations that inject a monoenergetic population of one million 5 MeV protons considering all three of the injection functions given by Equations 4.14, 4.15, and 4.17 (displayed in Figure 4.4). We have conducted simulations using both the uniform and Gaussian injection functions across the shock front (Figure 4.5), with a $\sigma = 17.5°$ in both latitude and longitude.

In this work we conduct simulations that consider particle propagation for 72 hours (24 hours after the shock reaches r_{max}) after the initial CME lift-off.

6.3 Geometry of observers

We derived observables for six observers (labelled A-F) located at 1 au, which can be seen in Figure 6.1, describing the observer-shock geometry at four snapshots in time. In Figure 6.1 the orange arrow gives the longitude of the shock nose, coincident with the AR longitude on the Sun, and the thin grey curved lines show the range of flux tubes that have been filled with particles by the shock up to time t. The solid green lines delimit the longitudinal range of IMF lines that are connected to the shock at the initial time (or an instantaneous injection at the Sun with the same angular width), and the red solid curved lines show the range of IMF lines connected to the shock front at the current time.

The AR is located at $(0°, 15°)$ longitude and latitude, respectively. As specified in Table 6.1, observers A, B, and C observe the AR as being western, while observers D, E, and F observe it as being eastern. Observers C and D are in the path of the shock and will observe it as it passes them, while the other observers will not experience the shock passage in situ. All observers are located at $\delta = 15°$ latitude to enable connection to the nose of the shock. We have examined the intensity profiles for observers at the same longitudes and at latitude $\delta = 0°$ and there are only very minor differences compared to the plots for $\delta = 15°$, shown in section 6.4.

We define the longitudinal separation between the AR and the observer footpoint, $\Delta\phi$, as

$$\Delta\phi = \phi_{AR} - \phi_{ftpt}, \tag{6.1}$$

where ϕ_{AR} is the longitudinal position of the source AR on the Sun and ϕ_{ftpt} is the longitude of the footpoint of the IMF line connected to the observer. Values of $\Delta\phi$ for our observers are given in Table 6.1.

An observer's connection to the shock evolves over time. The observer's cobpoint, where the observer's IMF line meets the shock, moves eastwards along the shock front as the shock propagates outwards (e.g. Heras et al. 1994; Kallenrode & Wibberenz 1997).

Observer	AR location	$\Delta\phi$ [°]
A	W79	30
B	W49	0
C	W19	-30
D	E11	-60
E	E41	-90
F	E71	-120

Table 6.1: Observers A-F shown in Figure 6.1. Columns are from left to right: Observer label, location of the AR source of the event with respect to the observer, and $\Delta\phi$ (see Equation 6.1). All observers are located at latitude $\delta = 15°$.

6.4 Intensity time profiles and anisotropies

From the output of our test particle simulations, we have calculated observables such as intensity profiles and anisotropies for our observers under a number of conditions. Particle counts at each observer were collected over a $10° \times 10°$ tile in longitude and latitude. Particle anisotropy, A, was calculated at each observer using the following equation (e.g. Kallenrode & Wibberenz 1997):

$$A = \frac{3\int_{-1}^{1} f(\mu)\,\mu\,d\mu}{\int_{-1}^{1} f(\mu)\,d\mu}, \tag{6.2}$$

where $f(\mu)$ is the pitch angle distribution and μ is the pitch angle cosine. We note that the sign of the anisotropy is dependent on the magnetic polarity: in

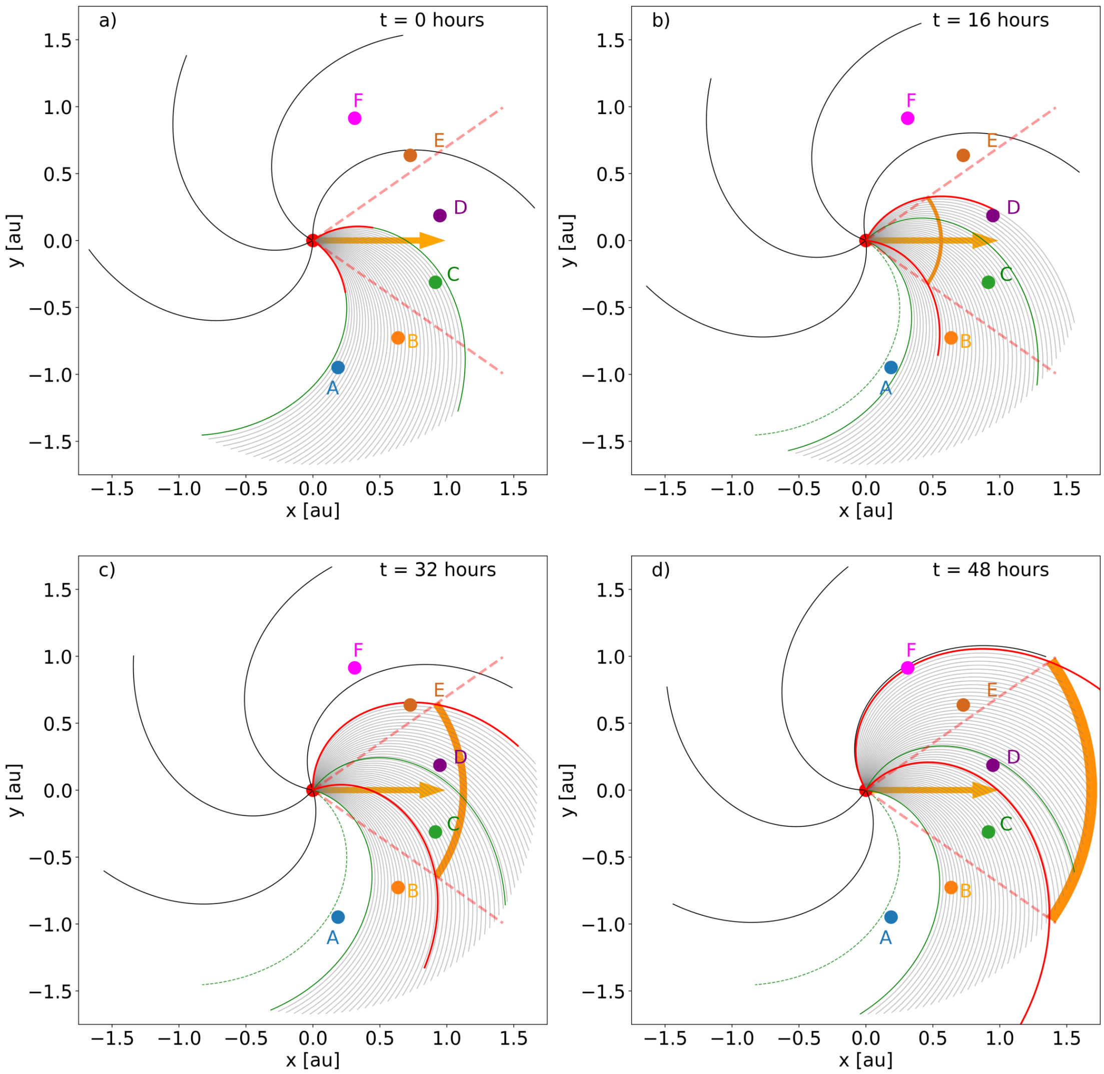

Figure 6.1: The shock position and observer geometry at t = 0 (top left), 16 (top right), 32 (bottom left), and 48 (bottom right) hours projected onto the solar equatorial plane. Here x and y are heliocentric Cartesian coordinates in the heliographic equatorial plane. The shock's projection onto the plane is displayed here as the orange shaded segments. Observers A-F are denoted by the coloured circles, and their exact positions are displayed in Table 6.1. The red radial dashed lines delimit the bounds of the shock, and the solid red curved lines show the IMF lines that are currently connected to the flanks of the shock front. The solid green curved lines show the bounds of the shock-like injection at the initial time (or equally an instantaneous injection at the Sun of the same angular width). The dashed green line shows the original position of the left most solid green line at the initial time. The grey IMF lines represent the range of IMF lines that have had particles injected onto them (the particle-filled flux tubes).

the following we use a unipolar antisunward magnetic field in which case positive anisotropy represents antisunward propagating particles. For this polarity according to Equation 6.2, an anisotropy of three corresponds to a fully beamed population travelling along the IMF antisunwards.

6.4.1 Effect of scattering mean free path on intensity and anisotropy profiles

We begin by analysing intensities and anisotropies at observers A - F under a variety of scattering conditions. Here we consider uniform injection in r, θ, and ϕ. In Figure 6.2 we display the intensity and anisotropy profiles for the six observers, for simulations with a mean free path spanning an order of magnitude from $\lambda = 0.1$ to 1.0 au.

In Figure 6.2 intensity profiles for different λ values at each observer appear remarkably similar to each other. In contrast to what has been derived from traditional 1D focussed transport models (e.g. Bieber et al. 1994), we do not see a significant change in the decay time constants with λ. SEPs in simulations with larger λ stream out more quickly. As expected for larger λ, we find smaller peak intensities and larger anisotropies, due to fewer scattering events.

The broad features of the intensity profiles at the six observers can be understood in terms of the geometry of the observers relative to the shock. As seen in Figure 6.1a, observers A, B, and C are connected to the shock at the initial time. As the shock propagates outwards, their cobpoints fall off the eastern edge of the shock, losing connection to the particle source (see Figure 6.1d for observer A). Over time, the shock connects to longitudes further west and allows observers D, E, and F to become connected to the shock source (e.g. Heras et al. 1994). This enables observers D, E, and F, which are not initial magnetically connected to the shock, to observe SEPs once connection is established. The intensity profiles in Figure 6.2

reflect the different timings of the observer-shock connection, with the onset of the event being delayed at observers *D*-*F*.

In Figure 6.2 the bottom panels display the anisotropy profiles observed at each of the six observers. The anisotropies clearly indicate the times of observer-shock connection. In Figure 6.2 the vertical green line shows the time of shock arrival at the observer's radial distance and the vertical black dotted line indicates the nominal time of observer-shock connection, for the observers not connected at the initial time. For observers *C* and *D,* sustained long-duration anisotropies are observed until the time of shock passage, in agreement with previous studies (e.g. Kallenrode & Wibberenz 1997; Kallenrode 2001). Observers *E* and *F* become connected to the shock when it is located beyond the observer radial position, and so they see negative anisotropies due to the sunward propagating particles from the shock.

Observers *C* and *D* see the peak intensity at the time of shock passage. Once the shock propagates past these observers, they are receiving sunward propagating particles injected at the shock and particles that were previously injected into the flux tube and have experienced scattering. As the shock propagates beyond the observer, the intensity of the former component diminishes with time as particles must overcome the magnetic mirror effect to reach the observer (e.g. Klein et al. 2018; Hutchinson et al. 2022). As a result, after shock passage, the anisotropies drop to zero, similar to the results of Kallenrode & Wibberenz (1997).

The peak intensities for observers *A* and *B* coincide with their loss of connection to the shock front due to corotation and shock radial motion (i.e. the observer's cobpoint falls off the eastern edge of the shock front). These geometric effects are highly dependent on parameters such as the shock longitudinal width, $w_{sh,\phi}$, the radial speed of the shock, and the observer longitudinal position relative to the edge of the shock front. In chapter 7 we compare observables for the cases with and without corotation included, and demonstrate that corotation plays a major role in the decay phase of the event.

6.4.2 Time-extended versus instantaneous injection

In previous work with our test-particle model, we only considered an instantaneous injection close to the Sun. We now compare observables for the cases of instantaneous injection and a radially uniform time-extended shock-like injection. We considered an instantaneous injection that has the same angular width as the extended injection ($70° \times 70°$). The intensity profiles for the two cases can be seen in Figure 6.3 for simulations considering $\lambda = 0.1$ au, where the solid black line is the radially uniform shock-like injection and the blue dashed line is the instantaneous injection. The same number of particles were injected into each simulation resulting in a significantly larger particle density close to the Sun for the instantaneous injection. This leads to systematically larger intensities for well-connected observers for the instantaneous injection (observers A-C). From the first panel (Observer A,) it can be seen that both the time-extended and instantaneous injection lead to the same event duration ($\sim$ 12 hours). This occurs as the corotation sweeps the particle-filled flux tubes westwards and away from the observer. Similarly, for observer B the intensity profile is cut short by the corotation. The corotation enables observer D to see a signal from the instantaneous injection as the particle-filled flux tubes corotate to this observer. In the shock-like simulations, observer D detects SEPs from the CME-driven shock approximately 10 hours earlier compared to the instantaneous injection, showing the clear timescale differences between the two cases. Observers E and F do not receive particles from the instantaneous injection over the timescales of our simulations as the corotation takes longer than 72 hours to rotate the particle-filled flux tubes to these observers. From Figure 6.3 it is clear that a temporally extended injection does not necessarily mean a longer duration SEP event, especially for western events.

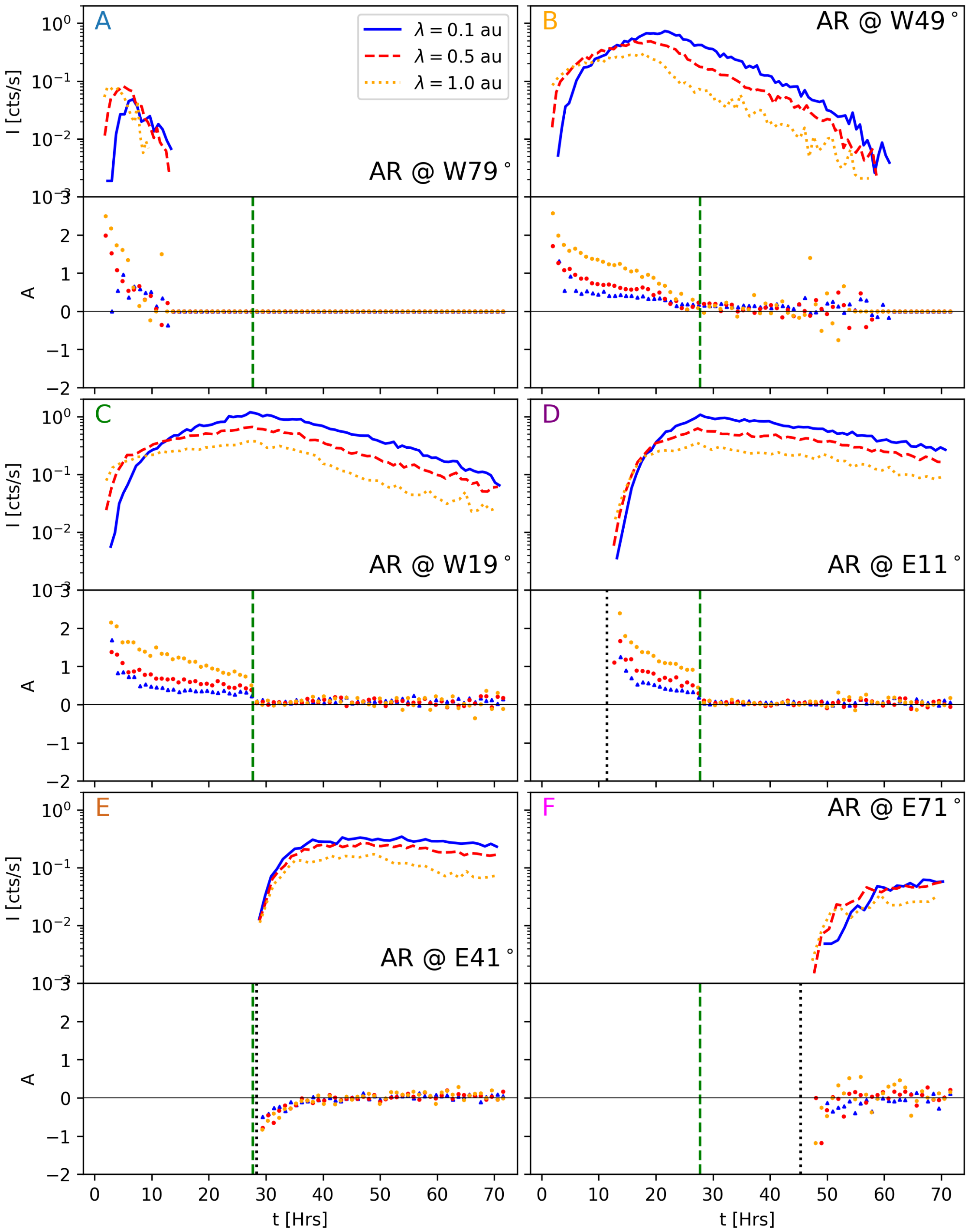

Figure 6.2: Intensity profiles of a monoenergetic population of 5 MeV protons for observers A-F at 1.0 au for a range of scattering conditions from $\lambda = 0.1$ au to $\lambda = 1.0$ au, for uniform injection in r, θ, and ϕ. The green dashed line indicates the time at which the shock reaches the observer radial distance, and the vertical dotted line shows the time when the observer establishes connection to the shock, for observers not connected at the initial time.

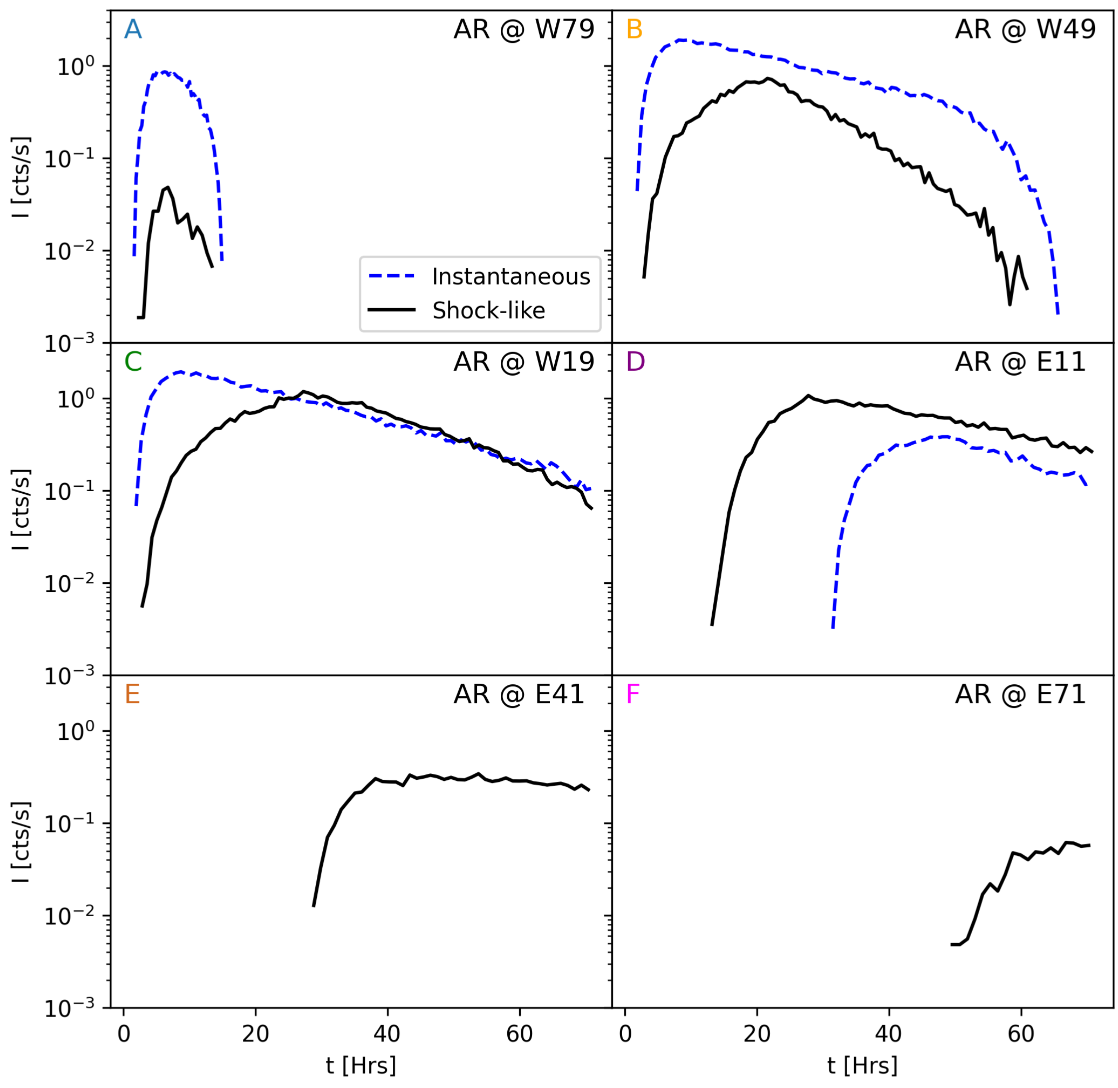

Figure 6.3: Intensity profiles for observers A-F considering an instantaneous injection (blue dashed lines) and an extended uniform injection (solid black lines) with respect to r, θ, and ϕ. The injection region is 70° in both cases. The simulations use $\lambda = 0.1$ au.

6.4.3 Dependence on the radial injection function

In Figure 6.4 we consider three radial injection functions (uniform, Weibull, and r^2, see Figure 4.4) and determine the intensity profiles at each of the six observers. The intensity profiles are surprisingly similar considering the very different radial injections. Comparing the uniform and Weibull function injections, it can be seen that there is little difference in the intensity profiles, which only show minor differences in the rise phase and peak intensities for western events (A, B, and C) due to the increased particle numbers injected close to the Sun for the Weibull injection. The very similar intensity profiles imply that the number of particles injected per unit area of the shock front, $Q(r)$, has a larger effect on intensity profiles than $R(r)$. The very low particle numbers for the r^2 injection close to the Sun results in no observable signal at observer A for this injection. This is also the reason for the smaller intensities observed at observers B and C.

For observer D all three injections are very similar, with the r^2 injection having slightly lower intensities during the rise phase. For more eastern events (observers E and F), the r^2 injection shows the largest intensities due to these observers connecting to the shock at larger radial distances where larger numbers of particles are injected. It is clear from these plots that geometric effects such as the time of observer-shock connection or disconnection as well as the corotation of particle-filled flux tubes towards or away from the observer have a much more significant effect on the intensity profile than the radial injection function. The role of corotation is discussed further in chapter 7.

The peak intensity, I_{peak}, is plotted in Figure 6.5 versus $\Delta\phi$ (defined in Equation 6.1) for the three shock-like radial injection functions. Each set of points is fit with a Gaussian of the form $I = I_0 \exp(-(\phi - \phi_0)^2/2\sigma^2)$. Table 6.2 shows the values of ϕ_0, σ, and I_0 for the fits shown in Figure 6.5. The largest intensities are obtained for the Weibull $R(r)$, which injects most particles close to the Sun, while the r^2

injection function results in much lower I_{peak} values. The standard deviations of the uniform and Weibull function injections are similar, while the r^2 injection has a larger standard deviation. The peak intensities at observers B and C are lower for the r^2 injection compared to the other injection functions as the number of particles injected close to the Sun is smaller. However, at observers D, E, and F, larger intensities are seen because the shock continues to inject particles late into the event. Figure 6.5 also shows that the broadness of the Gaussian is more closely related to the number of particles injected per unit area of the shock front, $Q(r)$, rather than $R(r)$. The centre of the Gaussian, ϕ_0, is shifted towards more negative values as one goes from Weibull to uniform to r^2 $R(r)$.

$R(r)$	$\Phi(\phi)$ $\Theta(\theta)$	I_0	ϕ_0 [°]	σ [°]
Uniform	Uniform	1.28	-36.4	33.4
Weibull	Uniform	1.39	-28.8	33.6
r^2	Uniform	0.71	-53.5	37.6
Uniform	Gaussian	2.55	-38.1	25.6

Table 6.2: Parameter values of the Gaussians fitted to the peak intensities versus $\Delta\phi$ plots in Figures 6.5 and 6.7.

6.4.4 Dependence on varying injection efficiency across the shock

In Figure 6.6 intensity profiles are shown when considering injection efficiencies across the shock in longitude and colatitude ($\Phi(\phi)$, $\Theta(\theta)$) that are a) uniform (solid black line) and b) Gaussian (red dashed line) with $\sigma = 17.5°$ centred on the shock nose (see Figure 4.5). It is apparent that changing the injection efficiency across the shock produces only small changes in the intensity profiles. For the Gaussian injection function at times when the observer's cobpoint lies near the shock nose

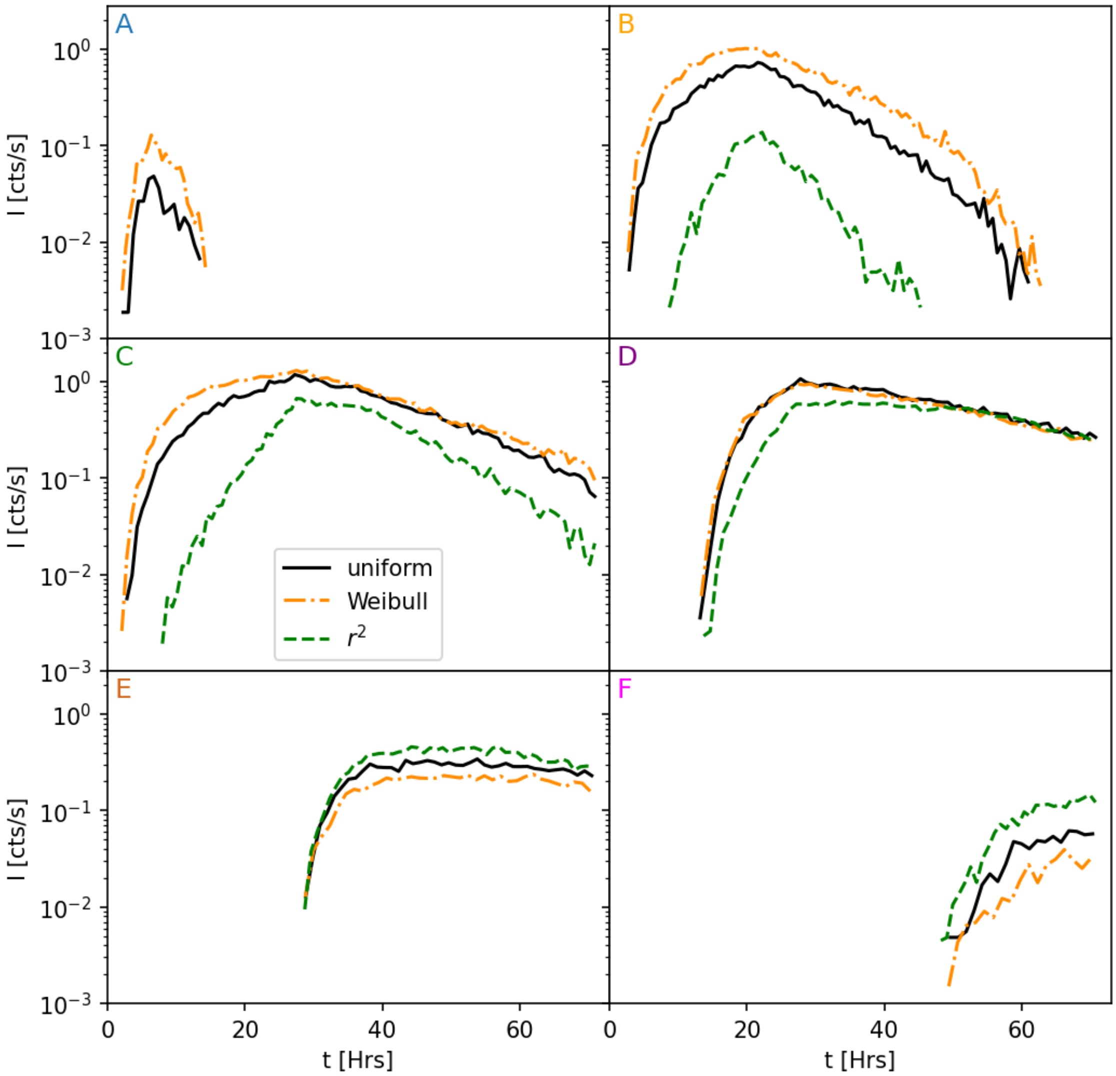

Figure 6.4: Intensity profiles for the three radial injection functions of Figure 4.4 at each of the six observers in Table 6.1 with scattering conditions described by $\lambda = 0.1$ au. Injection is uniform in θ, ϕ.

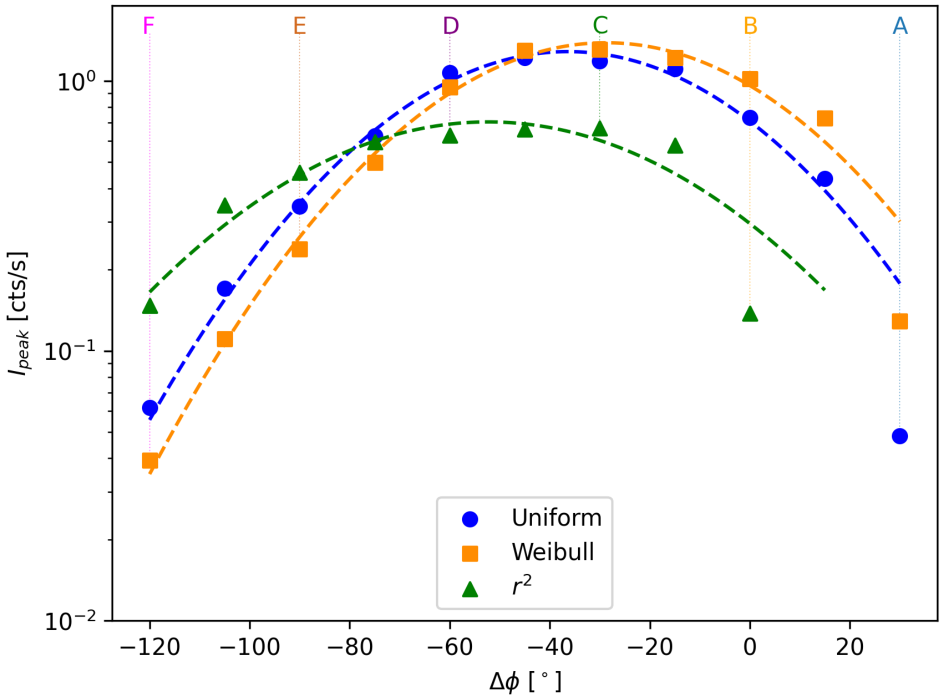

Figure 6.5: Peak intensity versus $\Delta\phi$ for the three radial injection functions.

(observers B and C), there is a faster increase compared to the uniform case during the rise phase and a larger peak intensity. Observers A and F, which experience connection to the flanks of the shock, have smaller intensities compared to the uniform injection case, but the differences are small. Changing the injection profiles across the shock does not have a big influence on the overall features of the intensity profiles.

In Figure 6.7 we plotted the peak intensity versus $\Delta\phi$ for uniform and Gaussian injection efficiency across the shock. Both sets of points are fitted with a Gaussian and the corresponding fit parameters are given in Table 6.2. As expected, having a Gaussian injection reduces the standard deviation of the fit due to the more spatially confined injected population.

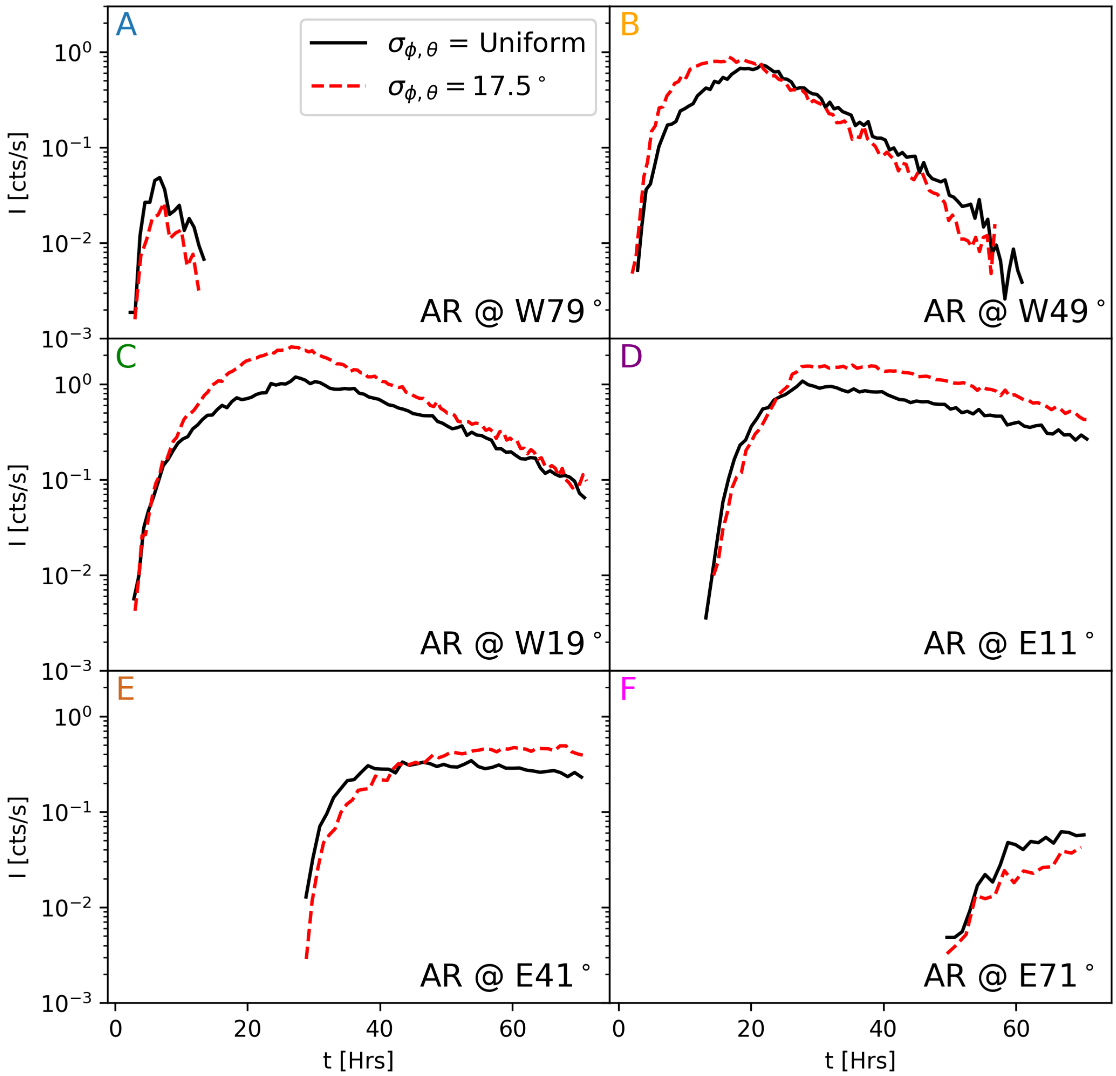

Figure 6.6: Intensity profiles for observers A-F at 1 au considering uniform and Gaussian longitudinal and latitudinal injection functions, with $\lambda = 0.1$ au. Injection is uniform in r.

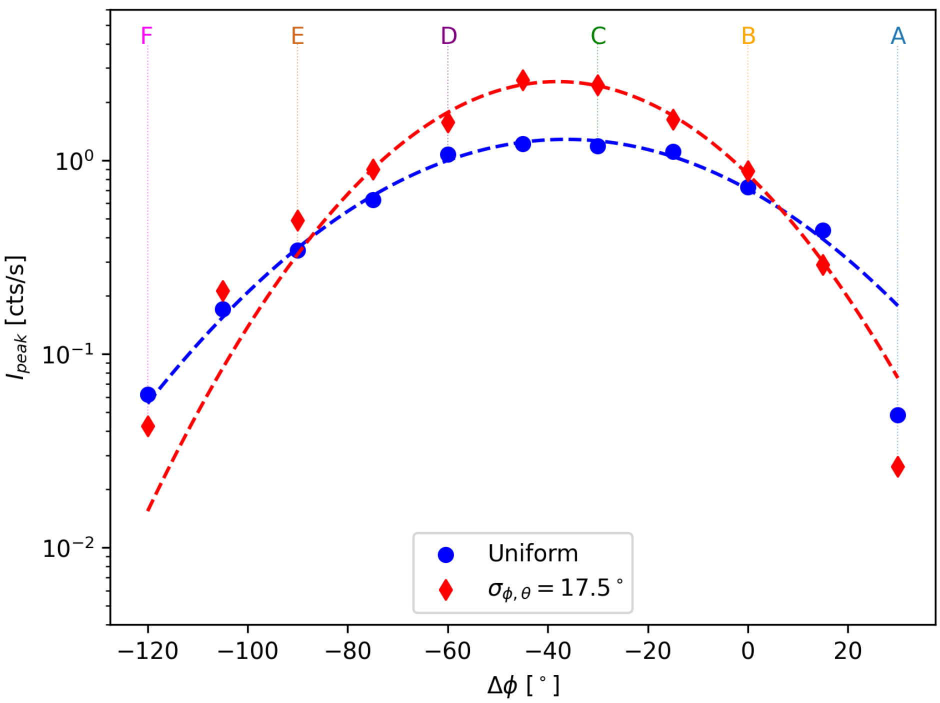

Figure 6.7: Peak intensity versus $\Delta\phi$ for shocks with uniform (blue circles) or Gaussian (red diamonds, $\sigma = 17.5°$) longitudinal and latitudinal injection efficiency. The shocks have an angular width of 70°. Both sets of points are fitted with Gaussians (dashed lines).

6.4.5 Role of shock width

We have considered shocks of different angular widths. In Figure 6.8 we compare intensity profiles at the six observers for shocks with $w_{sh,\phi} = w_{sh,\theta} = 70°$ (black line) and 120° (orange dashed line).

One effect of a wider shock is that an observer can remain magnetically connected to the shock front for a longer period of time. This factor changes the rise times for western events because the peak position in the intensity profiles is determined by the loss of connection to the shock front. This can be seen in Figure 6.8 for observers A and B where the rise times are extended and peak intensities occur later. Observations at C are similar in the two cases as the peak intensity occurs as the shock passes directly over the observer. We note that the exact values of the intensities are not directly comparable in these simulations as the same number of particles are injected over a larger volume for the wider shock (i.e. different $Q(r)$). For a wider shock at observers that see the event as being eastern, onsets take place earlier as the observer-shock connection is established more quickly when the shock is closer to the Sun, as can be seen in Figure 6.8 for observers D, E, and F.

6.4.6 Observers at 0.3 au

We used our simulations to obtain observables close to the Sun and compare them with 1 au observables. This is important now that *Parker Solar Probe* and *Solar Orbiter* are obtaining in situ data in the inner heliosphere.

Having fixed an observer at 1 au, in Figure 6.9, intensity and anisotropy profiles are plotted for two 0.3 au observers: the first radially in line with the 1 au observer (left column) and the second on the same IMF line (right column). Profiles at the 1 au observer are indicated by the dash-dotted lines for comparison. A uniform $R(r)$ was used.

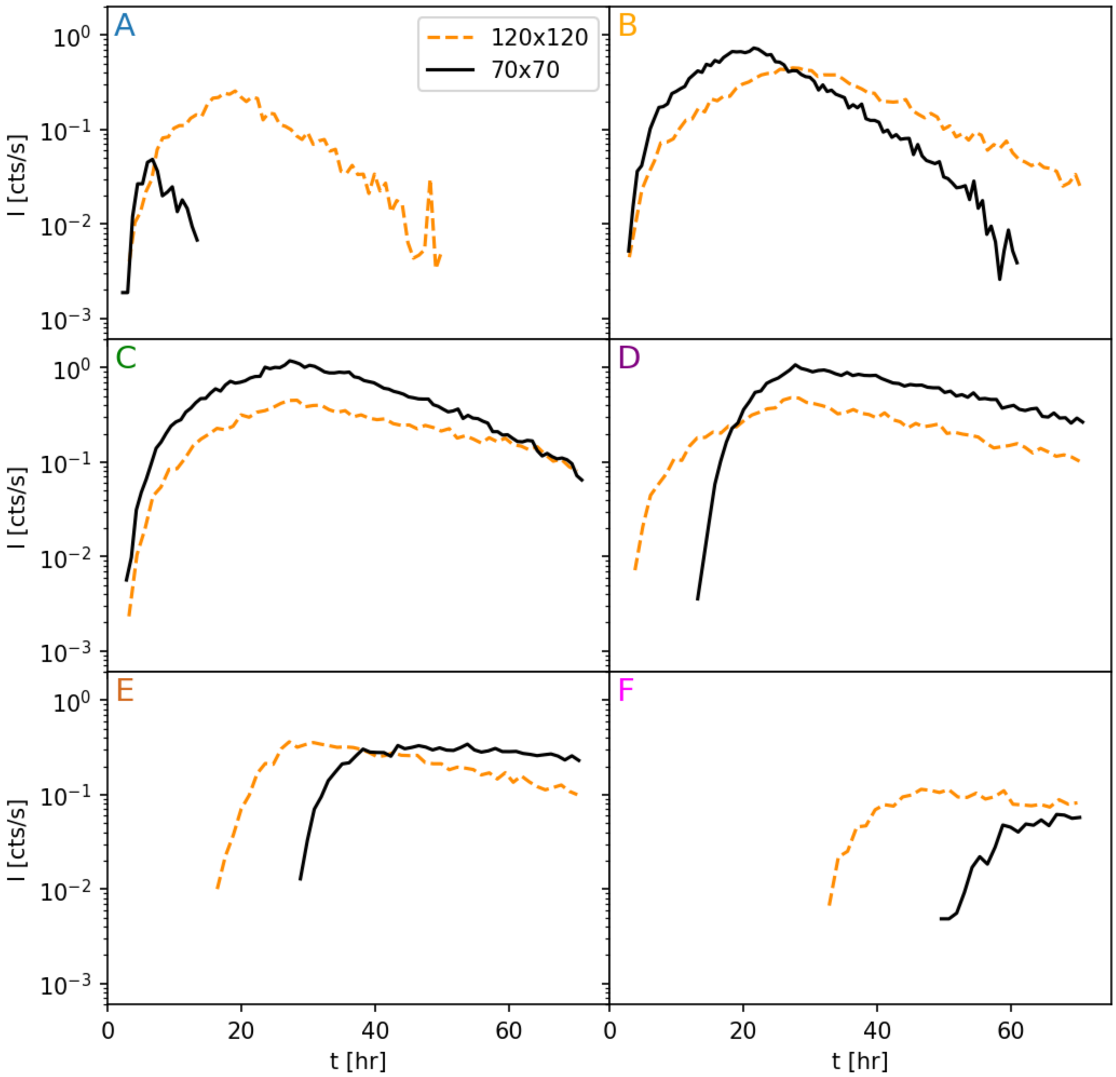

Figure 6.8: Intensity profiles at the six observers considering a shock 70° (solid black line) and 120° (orange dashed line) in both longitude and latitude.

Compared to the 1 au profiles, the 0.3 au profiles are characterised by the following: faster rise times, due to faster shock passage times at 0.3 au, and larger anisotropies (1 au anisotropies not shown) as there is reduced isotropisation due to fewer pitch-angle scattering events.

Generally the profiles at 0.3 and 1.0 au appear more similar for the case of observers on the same IMF line (right column), than for the radially in-line observers (left column). In the former case, both observers establish magnetic connection to the shock at similar times, with some difference due to propagation times. For the case of radially in-line 0.3 and 1.0 observers (left column), there are stronger differences between the profiles compared to the previous case. For observers *D*, *E,* and *F,* the onset at 0.3 au is more than 10 hours earlier than at 1 au. This is due to the fact that the radially aligned 0.3 au observers have footpoints located eastwards of the 1 au observer, meaning that for eastern events they will connect to the shock earlier. The decay time constants of the event appear significantly different at 0.3 and 1.0 au.

Considering peak intensities for the same IMF line case, for observers *B* - *F* the peak intensity at 1.0 au is larger than at 0.3 au. This is because particle injection before shock arrival is more extended for the 1 au observer. After shock passage, although particles can propagate sunwards to the observer, this becomes difficult due to magnetic mirroring (Hutchinson et al. 2022). For the observer *A* panel, the 0.3 au intensity is larger because both 0.3 and 1 au observers lose connection early in the event and scattering and propagation delay result in lower peak intensity at 1 au. The intensity profiles observed at 0.3 au have a weak dependence on λ (not shown). Eastern events show much slower decay phases compared to western events, similar to the 1.0 au observers.

We note that when close to the Sun, *Parker Solar Probe* and *Solar Orbiter* are moving in longitude at a high speed so that the intensity profiles shown in Figure

6.9, where the 0.3 au observer is stationary, do not correspond exactly to those measured by these spacecraft. In some phases of the mission, *Solar Orbiter* will be corotating with the Sun.

We have analysed the intensity profiles (not shown) at 0.3 au for the three radial injection profiles considered earlier (see Figure 4.4) and they display a behaviour similar to that in Figure 6.4, that is to say not a strong dependence on $R(r)$.

6.5 Discussion and conclusions

In this chapter we have presented the first 3D test particle simulations of SEPs with a temporally extended shock-like particle injection. Previously, in our modelling we had only considered an instantaneous injection near the Sun. By deriving the intensity and anisotropy profiles for observers at 0.3 and 1.0 au, we have reached the following main conclusions:

1. The main difference between an instantaneous and time-extended injection is that, in the former case, the spatial extent of the accelerated particle population is smaller (Figure 6.3). For initially well-connected observers (A-C), the duration of the SEP event is not significantly shorter for an instantaneous injection compared to an extended one.

2. The radial profile of injection (radial injection function, $R(r)$, Figure 4.4) plays a surprisingly small role in determining the intensity profiles at 1 au (Figure 6.4). However, $R(r)$ has a strong effect on the heliolongitudinal distribution of peak intensity (Figure 6.5) with injections that continue over larger radial distances leading to more negative ϕ_0 values and larger standard deviations.

3. Varying the injection efficiency across the shock (longitudinal and latitudinal injection functions, $\Phi(\phi)$, $\Theta(\theta)$, Figure 4.5) also plays a minor role in shaping intensity profiles (Figure 6.6).

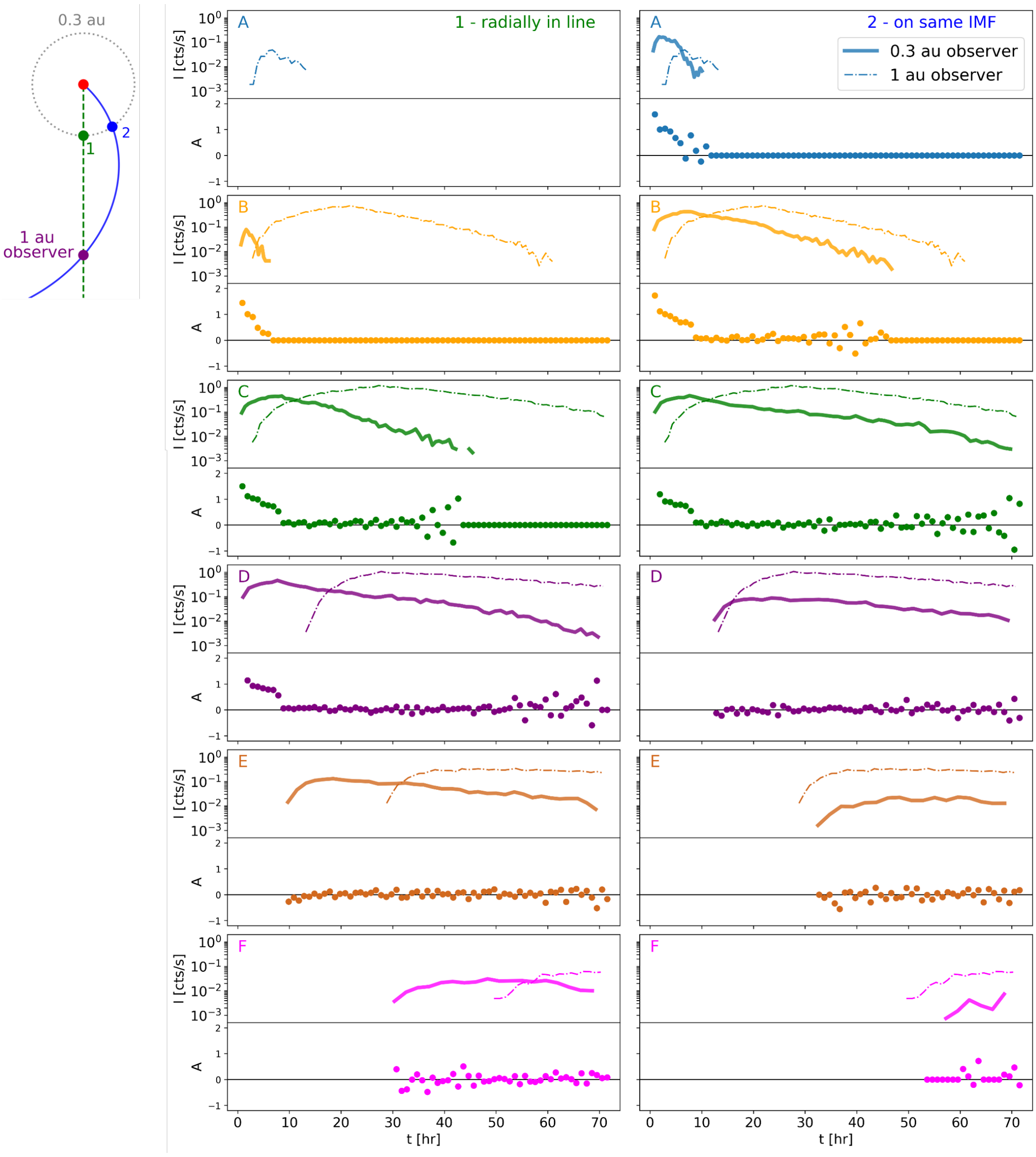

Figure 6.9: Schematic of observer geometry (left), with observer 1 located at 0.3 au, radially aligned with the 1 au observers, and with 2 located at 0.3 au along the same IMF line as the 1 au observer. Intensity and anisotropy profiles (right) for observers 1 and 2 (solid curves) and 1.0 au observer (dash-dotted curves).

4. In most cases simulations show large persistent anisotropies prior to shock passage and they decay sharply at shock arrival, becoming very close to zero following shock passage (Figure 6.2, observers *A*-*D*). For observers that see the event far in the east, the first arriving particles are propagating sunwards once connection to the shock is established.

5. Larger shock widths lead to longer duration SEP events because the observers remain connected to the shock for a longer time.

6. Intensity profiles at 0.3 au are similar to those at 1.0 au for two observers on the same IMF line, but they show faster rise times and larger anisotropies.

Our simulations show that the link between the duration of injection and the duration of the SEP event is very weak, unlike what is commonly assumed. Also from our simulations it is not clear that differences in the acceleration efficiencies at the flanks of the shock would leave a signature in the observed intensity profiles, as is often postulated (e.g. Tylka & Lee 2006). Spatial and geometric factors such as the establishment and loss of the observer-shock connection and the corotation of the particle-filled flux tubes towards and away from the observer are the dominant factors in determining the shapes and properties of SEP intensity profiles. Intensity profiles show little dependence on the mean free path, λ. In particular the decay phase constant is weakly dependent on λ, unlike what is derived from 1D focussed transport models (e.g. Bieber et al. 1994).

A number of studies of SEP observations have derived plots of peak intensity versus the separation $\Delta\phi$ between the source AR and observer footpoint (e.g. Wiedenbeck et al. 2013; Lario et al. 2013; Cohen et al. 2014; Richardson et al. 2014). Our work shows that these plots are sensitive to the radial injection profile and longitudinal and latitudinal injection efficiency. When a lot of acceleration takes place in IP space, the centre ϕ_0 of the Gaussian fit to the I_{peak} versus $\Delta\phi$ plot is shifted towards more negative values compared to cases where most of the acceleration takes place close to the Sun. For the shock width considered in our study, which is 70°, standard deviations between 26° and 38° are found.

In this chapter we have presented results for a monoenergetic proton population injected with energy of 5 MeV, which is a representative SEP energy. The difficulty in considering multiple energies lies in the need to specify how the radial injection function, $R(r)$, varies with energy. In addition, because of particle deceleration, the final particle energy in our simulations is smaller than 5 MeV for some particles. In constructing the intensity profiles in this chapter, we have chosen to include all particles >1 MeV. In actual SEP events, a spectrum of energies would actually be injected and particles of higher energy would decelerate into the 5 MeV range. Limiting the range of energies in the plot to a smaller energy range near 5 MeV produces some modifications in the profiles, but it does not change the qualitative trends we have found. For particle energies much higher than 5 MeV, injections are thought to take place only close to the Sun, limiting the range of longitudes of the shock source. For these higher energy particles, drift effects may be important in determining the range of accessible longitudes during an SEP event (Dalla et al. 2013).

The anisotropy characteristics shown in Figure 6.2, namely the large persistent anisotropies and the sunward anisotropies for far eastern events, are not routinely detected in SEP events to our knowledge. It is possible that this may be due to perpendicular transport effects.

Chapter 7

The effect of corotation on time-intensity profiles for a shock-like injection

7.1 Introduction

Magnetic flux tubes that guide energetic particle propagation corotate with the Sun. Depending on the location of an observing spacecraft, corotation may carry SEP-filled flux tubes either towards or away from the observer.

In this chapter we study the role of corotation effects in SEP events by means of 3D test particle simulations, with time-extended particle injection, describing continuous acceleration at a CME shock-like source. The test particle approach provides a natural way to describe corotation via the presence of a solar wind electric field, as described in section 4.2.3. It is also easy to remove corotation by switching off the electric field.

The results of this chapter have been published in Hutchinson et al. (2023a).

7.2 Corotation and SEP events

Several authors have pointed out the importance of corotation on SEP intensity profiles for the case of an instantaneous injection at the Sun (Dröge et al. 2010; Giacalone & Jokipii 2012; He & Wan 2015; Marsh et al. 2015). Corotation of steady state and quasi-steady state solar wind structures is the basis of empirical solar wind forecast models (e.g. Owens et al. 2013). Relatively few studies have commented on the effects of corotation on SEP intensity profiles for the case of time-extended injection at a CME-driven shock. Using an approximate methodology for including corotation within a focussed transport model, Kallenrode & Wibberenz (1997) concluded that it is not very important for events with an injection that is extended in time. Lario et al. (1998) also studied the effect of corotation in a focussed transport model by considering particle injection into a discrete number of flux tubes that sequentially pass over the observer. They noted that for certain periods corotation could affect their derived injection rate by up to a factor of 1.4. However, they concluded that corotation is not relevant in most situations within 1 au.

Overall, corotation is not thought to play a major role in large, gradual SEP events. Possibly as a result, many studies modelling extended SEP shock-like injections solve the relevant equations (usually focussed transport equations) in the corotating frame (e.g. Wang et al. 2012; He & Wan 2017; Hu et al. 2018). This assumes that observers are corotating, while in reality, spacecraft with SEP instrumentation do not corotate. Hence, the effects of corotation are not considered.

Although corotation is largely neglected in modelling SEP events it is natural to assume it may play a role in the east-west asymmetries found for a number of SEP intensity profile parameters. For example, several studies have plotted SEP peak intensity, I_{peak} versus the flare - observer footpoint separation, $\Delta\phi$, given by Equation 6.1. It is typical to fit a Gaussian to the I_{peak} vs $\Delta\phi$ plot where the Gaussian centre, ϕ_0 and the standard deviation, σ are determined, to try to better understand the longitudinal distributions of SEPs.

A number of studies have considered the east-west asymmetries in observed peak intensity versus $\Delta\phi$ plots, for protons with energies of tens of MeV, finding that in general the longitudinal distributions are consistent with a Gaussian centred at $\phi_0 \sim -15°$ and a standard deviation $\sigma \sim 40°$ (e.g. Lario et al. 2006, 2013; Richardson et al. 2014; Xie et al. 2019; He & Wan 2017). There is currently a debate about what exactly causes this asymmetry with some studies favouring transport effects in the asymmetric IMF (e.g. He & Wan 2015, 2017), while others have shown that injection by a shock-like source can produce the asymmetry (e.g. Lario et al. 2014; Ding et al. 2022). However, the role of corotation on these parameters has not been considered.

Our simulations show that although the role of corotation is generally ignored in the interpretation of gradual SEP events, it plays a major role in shaping observables, and can impact the east-west asymmetries in a variety of parameters.

7.3 Simulations

We use our 3D full-orbit test particle code, modified to describe a temporally extended injection of particles by a moving shock-like source, as described in chapter 4. Particles are injected at time t_{inj} at radial distance $r_{inj} = r_0 + v_{sh}\, t_{inj}$, where r_0 is the shock position at $t = 0$, and v_{sh} is its velocity, assumed constant. In this work particles are injected uniformly across the shock front in both longitude and latitude. The number of particles injected by the shock at distance r (radial injection profile, $R(r)$) is constant with r for $r < r_{max}$, where we assume injection stops.

In these simulations we follow a 5 MeV mono-energetic proton population, consisting of $N_p = 10^6$ particles. The particle crossing times at 1 au are collected to form intensity-time profiles at energy >1 MeV. The parameters of the shock front are as follows: shock speed $v_{sh} = 1500$ km s^{-1}, longitudinal and latitudinal width of the shock, $w_\phi = w_\delta = 70°$. The shock nose is located at heliolongitude $\phi_{nose} = 0°$ and heliolatitude $\delta_{nose} = 15°$. Injection at the shock ends at $t = 48$ hr, corresponding to $r_{max} = 1.73$ au, and we propagate SEPs until $t = 72$ hr.

Particles propagate in a unipolar Parker spiral IMF (e.g. Equation 4.3), with constant solar wind speed $v_{sw} = 500$ km/s. The shock does not disturb the Parker spiral and is not a magnetic enhancement. After injection the shock is transparent to particles. Unless otherwise stated, we use a mean free path $\lambda = 0.1$ au. The model does not include any perpendicular diffusion associated with turbulence, allowing us to investigate the corotation effects on SEP observables isolated from effects caused by cross-field diffusion (He & Wan 2017).

In the test-particle code, corotation is accounted for by including the solar wind electric field, $\mathbf{E}$, into the equation of motion of the particle (see section 4.2.3). The resulting electric field drift is a corotation drift (see Equation 4.7 and Equations 7-9 of Dalla et al. 2013), moving the particle's guiding centre by $\sim 14.2°$ per day in the direction of solar rotation. Setting $\mathbf{E} = 0$ in the test particle code switches off the corotation drift and allows one to study SEP propagation when corotation is neglected.

7.4 Intensity profiles at different observers

We study time-intensity profiles at six observers (labelled A - F, see Figure 7.1). All observers are located at the same latitude as the shock nose ($\delta = 15°$). We define the longitudinal separation, $\Delta\phi$, between the source AR and the observer's magnetic footpoint as by Equation 6.1. AR locations and corresponding $\Delta\phi$ values are given in Table 7.1. A Parker spiral magnetic connection is assumed when calculating ϕ_{ftpt}.

Figure 7.1 shows a schematic of the shock, observers and particle-filled magnetic flux tubes when corotation is excluded (*left*) and included (*right*) at $t = 48$ hr. The grey lines show the range of particle-filled flux tubes (i.e. IMF lines connected to the shock at $t \leq 48$ hr). The insets shows the range of longitudes filled with particles versus shock height.

Figure 7.2 shows intensity profiles for observers A - F, without and with corotation (top and bottom rows respectively). Intensity profiles are obtained by collecting counts within $10° \times 10°$ tiles on the 1 au sphere. Features of the profiles such as the onset time and peak time relate to the establishment/loss of connection to the shock and its arrival at the spacecraft, as was noted in a number of previous studies (e.g., Heras et al. 1994). Here the inclusion/non-inclusion of corotation has a very significant effect on intensity profiles, in particular for observers A-C, which see the source AR as western.

Comparing top and bottom rows in Figure 7.2, corotation has two main effects on the intensity profiles. Firstly, because the flux tubes are swept westward, the far western events are cut short (observers A and B). For example, with corotation the duration for observer A drops significantly from ~ 65 hr to ~ 12 hr. Secondly corotation increases the intensity during eastern events (observers D, E and F). For

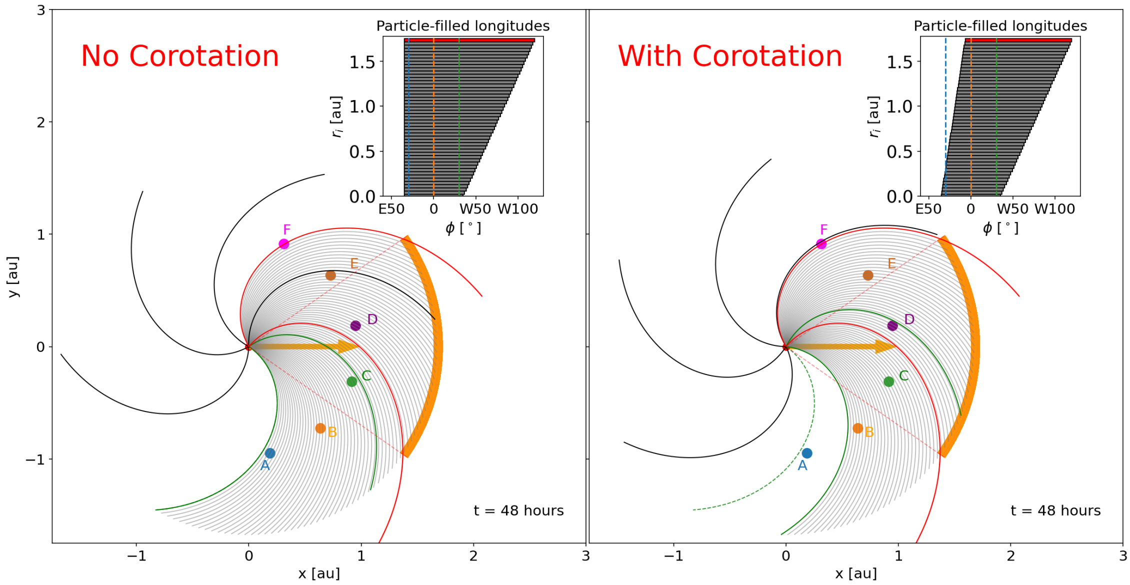

Figure 7.1: Schematic showing the geometry of the shock, observers, and particle-filled flux tubes, for the cases with (right panel) and without (left panel) corotation after 48 hours of shock propagation. Here x and y are heliocentric cartesian co-ordinates in the heliographic equatorial plane. Observers A-F are denoted by the coloured circles. The shock's projection onto the plane is displayed here as the orange shaded segments. The grey IMF lines represent the range of particle-filled flux tubes. The inset shows the range of longitudes that are filled with particles. The solid red curved lines show the IMF lines that are currently connected to the edges of shock. The solid green curved lines show the magnetic flux tubes at the edges of the shock at the initial time. In the corotation case these have rotated with respect to their initial location, shown by the dashed green line.

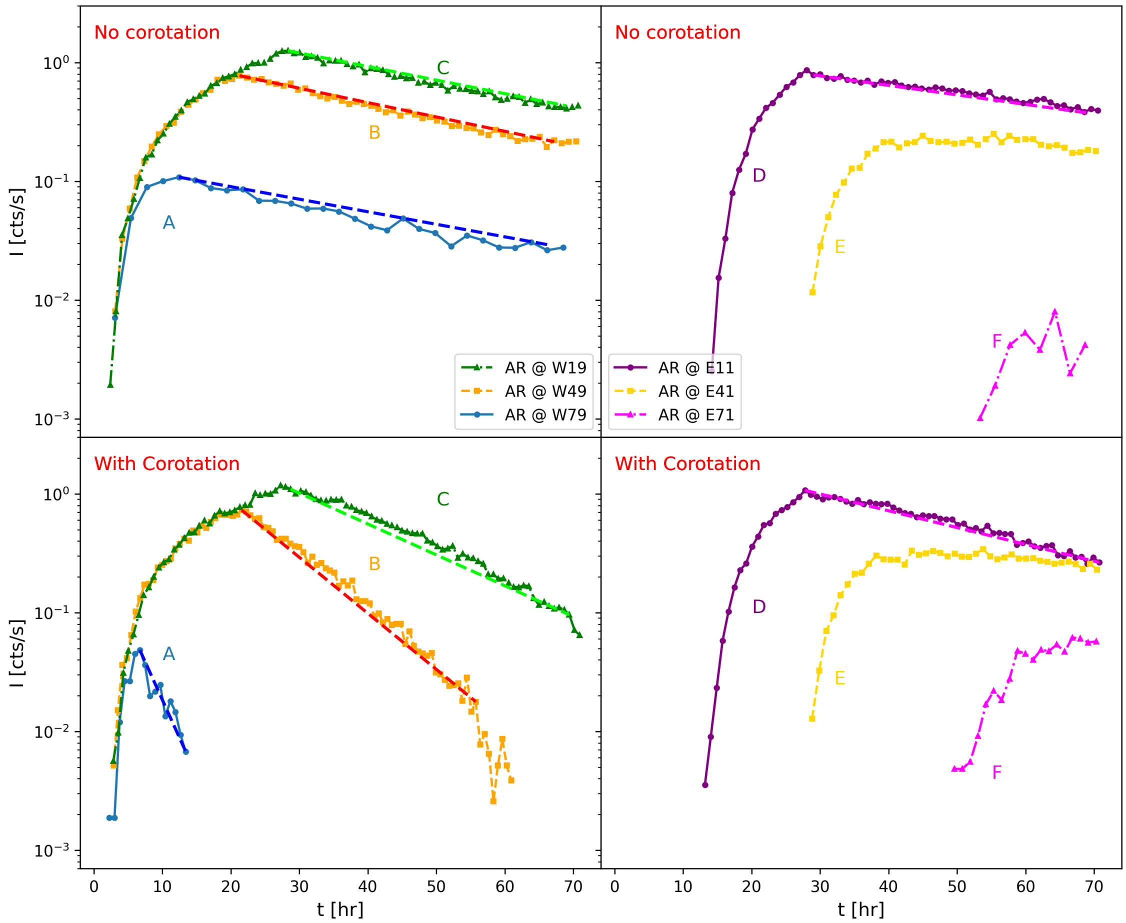

Figure 7.2: Intensity profiles for the six observers in Figure 7.1 without (top panels) and with (bottom panels) corotation for scattering conditions described by $\lambda = 0.1$ au. The dashed lines display the exponential decay fit for observers A-D. The shock reaches the 1 au distance at $t \sim 28$ hr.

Observer	AR location	$\Delta\phi$ [°]	$\tau_{\text{no\_corot}}$ [hr]	τ_{corot} [hr]
A	W79	30	41.1	3.4
B	W49	0	35.9	9.2
C	W19	-30	38.0	16.7
D	E11	-60	54.3	30.7
E	E41	-90	-	-
F	E71	-120	-	-

Table 7.1: Geometry of A-F observers and associated decay time constant of 5 MeV intensity profiles for $\lambda = 0.1$ au. Columns are from left to right: observer name, AR location with respect to the observer, $\Delta\phi$ as defined by Equation (6.1), decay time constant without corotation $\tau_{\text{no\_corot}}$, decay time constant with corotation τ_{corot} for $\lambda = 0.1$ au.

the observers located directly in the path of the shock (C and D) the effects of corotation are mainly seen after shock passage ($t \sim 28$ hr). We quantify the effect of corotation on profiles for observers A-D by determining the decay time constant, τ, by fitting an exponential between the peak intensity and a second point near the end of the profile, chosen by eye to avoid regions that fluctuate due to low counts. The decay time constants are given in Table 7.1 for the simulations in Figure 7.2, and are plotted versus $\Delta\phi$ in Figure 7.3, where data points corresponding to $\lambda = 0.5$ and 1.0 au are also shown, for simulations with (dashed lines) and without (dotted lines) corotation. There are no data points for observers E and F as there are no clearly defined decay phases in the intensity profiles. Figure 7.3 shows a systematic shift to low τ for simulations with corotation, corresponding to faster decay phases for all observers. When corotation is included there is little dependence on the scattering conditions as corotation dominates the decay phase. When corotation is neglected τ is a measure of the degree of scattering, with smaller λ leading to extended decay phases.

The peak intensity, I_{peak}, is plotted versus $\Delta\phi$ in Figure 7.4. I_{peak} is largest for observers C and D, which are directly in the path of the shock. We fitted both sets of points with a Gaussian centred at $\Delta\phi = \phi_0$. Figure 7.4 shows that ϕ_0 is shifted with respect to the well-connected location ($\Delta\phi = 0$), with $\phi_0 = -36.4°$ for the corotation fit and $\phi_0 = -31.2°$ for no corotation. The corotation fit has a standard deviation $\sigma = 33.4°$ and the no corotation $\sigma = 31.3°$. This east-west asymmetry has been noted observationally by several authors (e.g. Ding et al. 2022; Lario et al. 2013; He & Wan 2017). Figure 7.4 shows that corotation enhances the asymmetry.

Figure 7.5 shows the median longitude, ϕ_{SEP}, of all the test particles in our simulation versus time. The geometry of the shock connection to the observer already naturally produces a westward shift of ϕ_{SEP} with time, as shown by the blue triangles (Ding et al. 2022). When corotation is taken into account, the latter effect becomes more pronounced (red points), resulting in the larger σ for the corotation points in Figure 7.4. We note that the discontinuity at $t = 48$ hr is due to injection by the shock ending at this time.

7.5 Discussion and conclusions

In this chapter we simulated particle injection from a shock-like source using 3D test particle simulations and compared intensity profiles over a wide range of observer longitudes with and without corotation.

The main conclusions of our work are as follows:

1. Corotation of particle-filled flux tubes has a strong effect on SEP intensity profiles for the case of time-extended acceleration at a propagating CME-shock (Figure 7.2). Its main influence is on the decay phase of the event: e.g. it reduces the decay time constant compared to the case when corotation is not included. The strongest corotation effects are on observers that see the

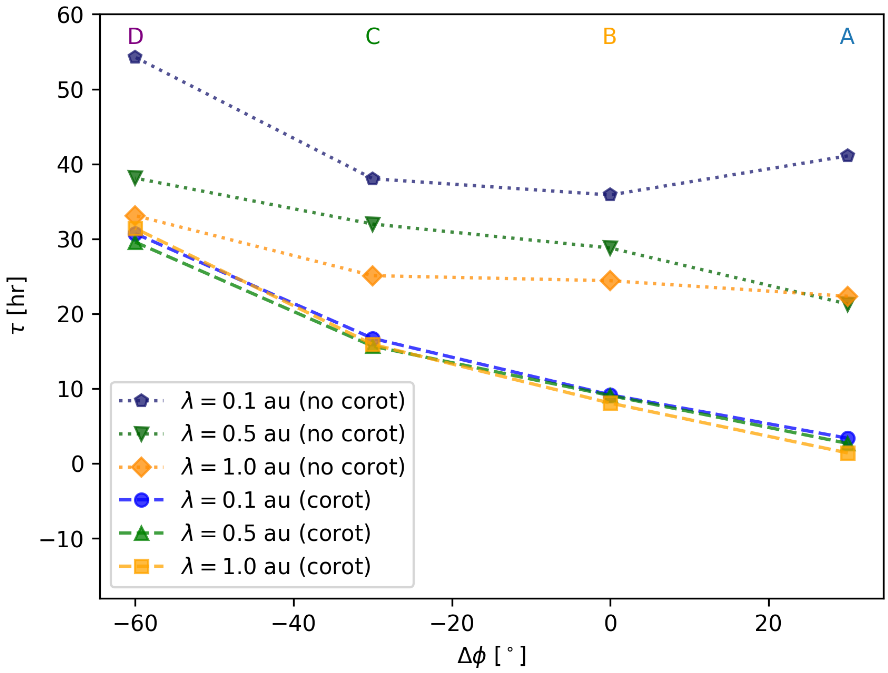

Figure 7.3: Decay time constant (τ) for four of our observers with (dashed lines) and without (dotted lines) corotation and scattering conditions in the range $\lambda = 0.1$ au to $\lambda = 1.0$ au.

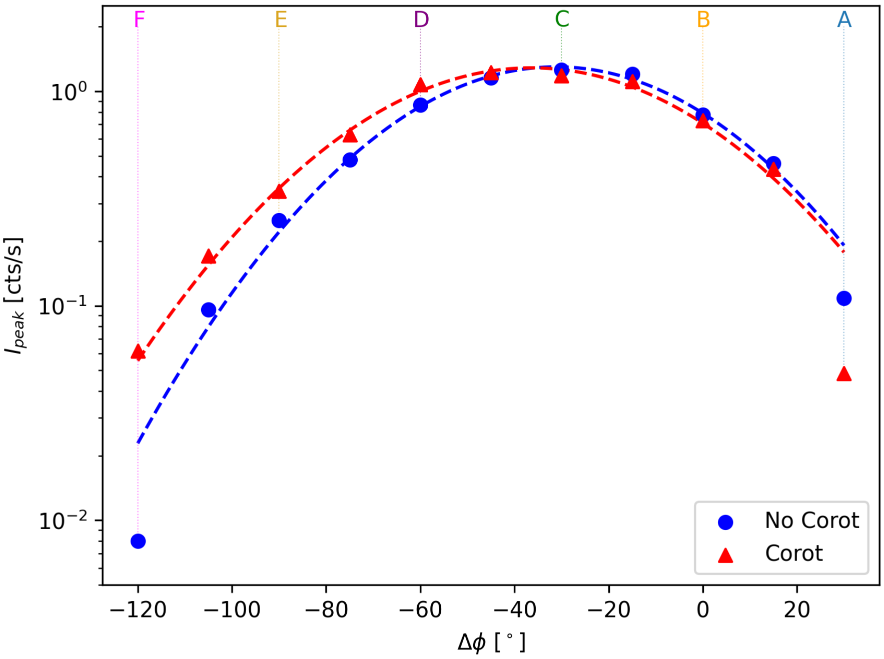

Figure 7.4: Peak intensity versus $\Delta\phi$ for the six observers A-F with (red triangles) and without (blue circles) the effects of corotation for scattering conditions described by $\lambda = 0.1$ au. The points are fit with Gaussian functions shown as the dashed lines.

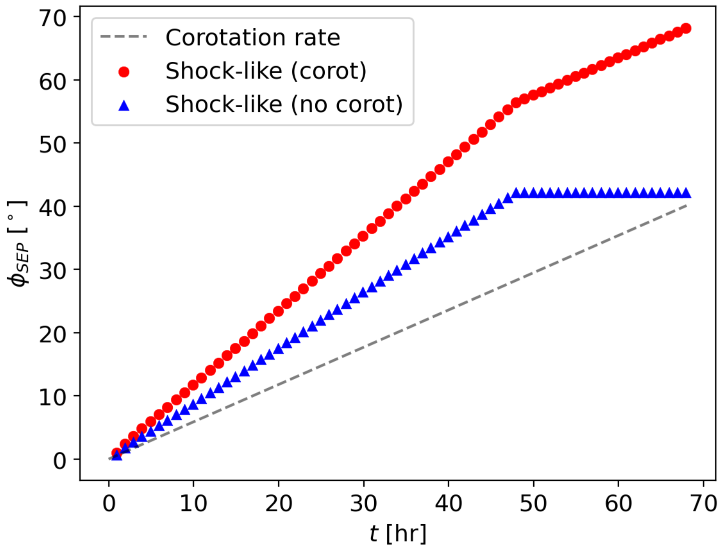

Figure 7.5: Median longitudinal position of the SEP population, ϕ_{SEP}, for the shock-like injection with corotation (red circles), without corotation (blue triangles). The grey dashed line shows the corotation of the flux tube connected to the source region at $t = 0$.

source AR in the west: both the event duration and decay time constant are significantly reduced (Table 7.1 and Figure 7.3).

2. Corotation enhances maximum intensities during eastern events and makes the east-west asymmetry in peak intensity versus $\Delta\phi$ stronger (Figure 7.4).

3. Deriving intensity profiles without including the effects of corotation (by solving particle transport equation in the corotating frame or using a 1D approach that models propagation along a single flux tube) artificially extends the decay phase, especially for western events.

4. Varying the scattering mean free path between $\lambda = 0.1$ and 1.0 au has very little influence on the decay phase (negligible difference in the value of τ) when corotation is included, indicating that corotation is a dominant process during the decay phase of SEP events.

Our simulations show that, unlike previously thought (e.g. Kallenrode & Wibberenz 1997; Lario et al. 1998), corotation is a key influence on the decay phase of SEP events at 1 au and it also affects the peak intensity phase (excluding possible Energetic Storm Particle (ESP) enhancements, e.g. Wijsen et al. 2022). Within the large variability in the properties of SEP events, there is some indication that corotation plays a role. Dalla (2003) analysed the duration of 52 events and showed that there is a tendency for eastern events to have longer durations compared to western ones. The longitudinal dependence of the SEP spectral index, first reported by Van Hollebeke et al. (1975), can be explained by corotation effects: eastern events take a long time to corotate to an Earth observer and for this reason their spectral index is larger as the high energy particles have escaped the inner heliosphere by the time the flux tube corotates over the observer.

In the work presented here we have used a uniform rate of injection from the shock with radial distance and longitude/latitude across the shock. In chapter 6 we have also considered two other radial injection functions: we verified that corotation plays an important role regardless of the details of the injection function. Similarly, we showed that varying the spatial profile of injection along the shock front has a minor effect on the intensity profiles.

We note that when constructing time-intensity profiles as shown in Figure 7.2, we used all particles (> 1 MeV), although some of them have an energy lower than the initial 5 MeV, due to adiabatic deceleration. We have determined intensity profiles for particles in the energy range 4.5-5.0 MeV (not shown), which show very similar behaviour to those in Figure 7.2, displaying even smaller decay time constants in the corotation case. During an SEP event, particles over a range of energies will be injected and those produced with initial energy higher than 5 MeV will decelerate into the latter energy band.

A number of studies have used focussed transport or Fokker-Planck equations to determine intensity profiles after injections from a CME-driven shock-like source (e.g. He & Wan 2015; Wang et al. 2012). In contrast to our results their intensity profiles look very similar across a range of longitudinal positions for the observer, and this may be due to neglecting corotation.

We have derived other observables such as the onset time and time of peak intensity from our simulations. However, corotation does not have a significant effect on these quantities as they are primarily determined by geometric factors, such as times of observer-shock connection and time of shock passage at the observer.

Chapter 8

Conclusions

CHAPTER 8

8.1 Overview

In this thesis we have simulated the propagation of SEPs injected into the interplanetary medium by a shock-like source, using test particle simulations.

We have applied our simulations to the study of two main problems: the energetic proton back-precipitation onto the solar atmosphere in relation to LDGRFs (chapter 5), and the modelling of SEP propagation to 1 au observers at different positions in space (chapters 6 and 7).

There has been a lot of scientific debate over the origin of prolonged γ-ray emission observed during LDGRFs due to new observations from the *Fermi* LAT. These γ-rays are thought to originate from proton and alpha particle interactions with the photospheric plasma resulting in neutral pion production and subsequent decay to γ-rays (Share et al. 2018). The emission has been observed to last for hours during LDGRFs. Hence, a mechanism for the γ-ray production needs to sustain high energy protons and alpha particles striking the solar surface over long periods of time. One hypothesis is that particle acceleration occurs over extended times at a CME-driven shock and these particles back-precipitate onto the solar atmosphere over extended time scales. Here we modelled the back-precipitation process considering instantaneous injections at CME-shock heights. Our simulations include scattering and the magnetic mirroring process (e.g. Klein et al. 2018; Hutchinson et al. 2022) that impedes the particles' journey back to the solar surface.

We have also developed the first shock-like injection for a 3D full-orbit test particle code, and used this new model to investigate the role of an extended SEP injection on intensity and anisotropy profiles. Typically, long-lasting gradual SEP events are thought to be associated with injection at a CME-driven shock over extended times, with this supposedly causing the long duration of the event (Reames et al. 1997). We compared the temporally extended shock-like injection and the previously used instantaneous injection to determine whether this is the case. We also investigated the effect of using different radial, longitudinal and latitudinal injection functions on intensity profiles at 1 au. The corotation of magnetic flux tubes with the Sun had been thought to be negligible for particles originating at a CME-driven shock for observations at 1 au (Kallenrode & Wibberenz 1997; Lario et al. 1998). Our test particle code allowed us to assess the importance of this process on intensity profiles at 1 au by comparing simulations with and without the effects of corotation.

8.2 Results summary

Regarding LDGRFs and the possible role of energetic proton back-precipitation onto the solar atmosphere within the CME-shock scenario, we found that long after the eruptive event, when CME shocks are very far from the solar surface, back-precipitation is extremely difficult. A faster CME shock only exacerbates this problem. The large precipitation fractions that are required to explain LDGRF events in terms of the CME-shock scenario do not appear possible within simulations that include scattering and magnetic mirroring. For an individual event, a model that makes the duration of the acceleration longer will result in smaller total precipitation fractions. We modelled the specific shape of the precipitation count rate versus time with our simulations and found that it displays a much faster decay than that observed in LDGRF intensity profiles.

Overall, our results show that acceleration at a CME-driven shock and subsequent back-precipitation to the photosphere cannot explain the observed γ-ray emission during LDGRFs. It is possible that particles of shock-origin may contribute significantly when the shock is close to the Sun. However, magnetic mirroring provides a significant challenge to this process which becomes increasingly tough to overcome as the event goes on and the shock reaches large radial distances from the Sun.

Regarding the injection and propagation of SEPs to 1 au, surprisingly we found that the details of the injection function, in particular the overall duration of injection from the shock source, do not have a strong effect on intensity and anisotropy profiles at 1 au. In particular, for initially well-connected observers (A-C) the duration of the SEP event is not significantly shorter for an instantaneous injection compared to an extended one. We found that varying the injection efficiency across the shock (i.e. varying the longitudinal and latitudinal injection functions) also plays a minor role in shaping intensity profiles. Intensity profiles at 0.3 au are similar to those at 1.0 au for two observers on the same IMF line, but show faster rise times, and larger anisotropies.

Our results showed that the overall duration and decay phase of SEP events are strongly affected by corotation. Corotation was found to reduce the decay time constant compared to the case when corotation is not included. The strongest corotation effects are on observers that see the source AR in the west: both the event duration and decay time constant are significantly reduced. We found that corotation enhances maximum intensities during eastern events and makes the east-west asymmetry in peak intensity versus $\Delta\phi$ stronger. These findings are important because majority of SEP models derive intensity profiles without including the effects of corotation (by solving the particle transport equation in the corotating frame or using a 1D approach that models propagation along a single flux tube). As a result they artificially extend the decay phase, especially for western events. We demonstrated that varying the scattering mean free path between $\lambda = 0.1$ and 1.0 au has very little influence on the decay phase (negligible difference in the value of the decay time constant, τ) when corotation is included. Thus the decay phase does not depend strongly on the scattering mean free path: in this sense the results from our 3D test particle model differ from traditional 1D focussed transport approaches. Hence, including the effects of corotation is required to ensure accurate

SEP modelling.

8.3 Future work

Over the PhD we have conducted many simulations of SEP propagation using our test particle code. There are certainly improvements that could be made and other important aspects to consider in the future. Below we detail possible future work that will enable more realistic investigations into the above mentioned phenomena.

8.3.1 Back-precipitation relating to LDGRFs

In our work we did not consider a detailed model of the magnetic field in the corona and near the photosphere and their effects on particle back-precipitation. The coronal magnetic field is complex and modelling it accurately can be done in a number of ways ranging from using a potential field source surface model (simplest) to using an MHD simulation (most complex). These types of simulations show significant expansion of the magnetic field, which provides an increased challenge to charged particles that attempt to propagate deep into the solar atmosphere. Below the corona the magnetic field penetrates the photosphere at the edges of the convective cells and forms a 'canopy' at the base of the corona, where magnetic pressure dominates (Seckel et al. 1991, 1992). The result of the magnetic field being swept to the edges of convective cells is an inhomogeneous magnetic field, with flux 'bundles' having magnetic field strengths of the order of 10^3 Gauss, while the average magnetic field strength of the photosphere is of the order of a few Gauss (Seckel et al. 1991). Therefore, particles propagating through coronal and photospheric magnetic fields will experience increased mirroring, not considered in this study. Including these effects is likely to reduce the precipitation fractions further due to the large mirror ratio associated with the inhomogeneous magnetic field structure.

In addition modelling of more events in detail, especially the complex events that are difficult to explain using the shock source scenario, such as the 2012 March 7 event, would likely provide interesting information. In further work it would be useful to also model the effects of including the heliospheric current sheet and current sheets in the vicinity of the CME.

8.3.2 Shock-like injection effects on intensity profiles

In this thesis (chapter 6) we presented results for a monoenergetic proton population injected by a shock-like source with energy of 5 MeV. Ideally in future work a population with a distribution of energies will be considered. The difficulty in considering multiple energies lies in the need to specify how the radial injection function, $R(r)$, varies with energy.

Our model did not include magnetic field line meandering (Laitinen et al. 2016), which would lead to significant motion of the particles perpendicular to the mean magnetic field. This effect could potentially explain some features of our modelled intensity profiles that do not agree with SEP observations: for eastern events our simulations do not show the slow rise phase found in observations (e.g. Cane et al. 1988; Kahler 2016), displaying instead very delayed onsets and relatively fast rises. Inclusion of perpendicular transport may produce the observed long rise times as long as the process is slow. It might be possible to determine a limit to the strength of perpendicular transport by modelling the slow rise times during eastern events. One would expect perpendicular diffusion to produce earlier SEP onsets for eastern events and to help SEP intensities reach similar values at far away locations faster. Considering the plots of I_{peak} versus $\Delta\phi$ (Figures 6.5 and 6.7) perpendicular diffusion would increase the peak intensity at the less well-connected observers, resulting in a larger standard deviation of the Gaussian fits. It is expected that with the inclusion of perpendicular diffusion intensity profiles at widely separated locations will become more similar to each other. We hope to include the effects of turbulence-induced perpendicular transport in future work.

While our model of shock-like injection has allowed us to derive the qualitative patterns described above, it contains several simplifications that will need to be improved upon in future work. Our simulation does not model shock acceleration, nor the interaction of energetic particles with the shock. We have not considered how the shock decelerates with time: this would affect the extent of the event since IMF field lines towards the west would only be reached at later times. We hope to include shock deceleration in the future. In addition downstream features, such as a flux rope and non-Parker field lines, are not described. We note that MHD simulations of shock propagation show that the magnetic field lines in the downstream can connect back to the shock. In 3D the magnetic field lines are known to wrap over/under the ejecta (Lario et al. 1998): we expect that there are many cases where an observer behind the shock would be connected to it. Our study applies directly to these cases. With a more accurate model of the downstream region intensities may differ from those in Figure 7.2 behind the shock, however they would still be influenced by corotation of the magnetic flux tubes. We hope to include such a model in future studies.

The simulations in the present study do not include the HCS, which has been shown to have significant effects for SEP propagation when the source region is located close to it (Battarbee et al. 2017, 2018; Waterfall et al. 2022). Individual events, depending on the magnetic configuration, may be significantly influenced by the HCS due to strong HCS drift motions, especially for high energy SEPs (Waterfall et al. 2022).

Another factor which may influence intensity profiles are complex local magnetic field and solar wind structures, not included in our model at present. Any perturbations to the Parker spiral will affect the times of observer-shock connection and so will affect observable parameters such as onset times and peak times. Some structures like corotating interaction regions (Wijsen et al. 2019) or magnetic clouds (Kallenrode 2002) may significantly affect SEP transport affecting intensity profiles.

Future work will also include using the model to analyse specific SEP events observed by multiple spacecraft. Our work with a CME-driven shock-like injection in test particle simulations marks one step toward understanding the complex process of SEP propagation that is necessary in order to confidently forecast potentially devastating SEP events in the future.

Bibliography

Ackermann, M., Allafort, A., Baldini, L., et al. 2017, ApJ, 835, 219

Afanasiev, A., Aran, A., Vainio, R., et al. 2018, in Solar Particle Radiation Storms Forecasting and Analysis, ed. O. E. Malandraki & N. B. Crosby, Vol. 444, 157–177

Ajello, M., Albert, A., Allafort, A., et al. 2014, ApJ, 789, 20

Baring, M. G. 1997, in Very High Energy Phenomena in the Universe; Moriond Workshop, ed. Y. Giraud-Heraud & J. Tran Thanh van, 97

Battarbee, M., Dalla, S., & Marsh, M. S. 2017, ApJ, 836, 138

Battarbee, M., Dalla, S., & Marsh, M. S. 2018, ApJ, 854, 23

Bieber, J. W., Droge, W., Evenson, P. A., et al. 2002, ApJ, 567, 622

Bieber, J. W., Matthaeus, W. H., Smith, C. W., et al. 1994, ApJ, 420, 294

Bruno, A., Bazilevskaya, G. A., Boezio, M., et al. 2018, ApJ, 862, 97

Burns, J. A. & Halpern, G. 1968, Journal of Geophysical Research (1896-1977), 73, 7377

Cane, H. V. 1988, Journal of Geophysical Research: Space Physics, 93, 1

Cane, H. V., Reames, D. V., & von Rosenvinge, T. T. 1988, Journal of Geophysical Research: Space Physics, 93, 9555

Cid, C., Palacios, J., Saiz, E., Guerrero, A., & Cerrato, Y. 2014, J. Space Weather Space Clim., 4, A28

Cliver, E. W., Kahler, S. W., & Vestrand, W. T. 1993, in International Cosmic Ray Conference, Vol. 3, 23rd International Cosmic Ray Conference (ICRC23), Volume 3, 91

Cohen, C. M. S., Christian, E. R., Cummings, A. C., et al. 2021, A&A, 650, A23

Cohen, C. M. S., Mason, G. M., Mewaldt, R. A., & Wiedenbeck, M. E. 2014, ApJ, 793, 35

Dalla, S. 2003, in American Institute of Physics Conference Series, Vol. 679, Solar Wind Ten, ed. M. Velli, R. Bruno, F. Malara, & B. Bucci, 660–663

Dalla, S. & Browning, P. K. 2005, A&A, 436, 1103

Dalla, S., de Nolfo, G. A., Bruno, A., et al. 2020, A&A, 639, A105

Dalla, S., Marsh, M., Kelly, J., & Laitinen, T. 2013, Journal of Geophysical Research: Space Physics,, 118, 5979

Dalla, S., Marsh, M. S., & Laitinen, T. 2015, ApJ, 808, 62

de Nolfo, G. A., Bruno, A., Ryan, J. M., et al. 2019, ApJ, 879, 90

Desai, M. & Giacalone, J. 2016, Living Reviews in Solar Physics, 13

Ding, Z., Li, G., Ebert, R. W., et al. 2022, Journal of Geophysical Research: Space Physics, 127, e2022JA030343

Dresing, N., Kouloumvakos, A., Vainio, R., & Rouillard, A. 2022, ApJL, 925, L21

Dröge, W., Kartavykh, Y. Y., Klecker, B., & Kovaltsov, G. A. 2010, ApJ, 709, 912

Earl, J. A. 1974, ApJ, 193, 231

Giacalone, J. & Jokipii, J. R. 2012, ApJ, 751, L33

Giuliani, P., Neukirch, T., & Wood, P. 2005, ApJ, 635, 636

Gómez-Herrero, R., Dresing, N., Klassen, A., et al. 2015, ApJ, 799, 55

Gopalswamy, N., Lara, A., Yashiro, S., Kaiser, M. L., & Howard, R. A. 2001, Journal of Geophysical Research: Space Physics, 106, 29207

Gopalswamy, N., Xie, H., Akiyama, S., et al. 2013a, ApJ, 765, L30

Gopalswamy, N. et al. 2013b, Adv. Space Res., 51, 1981

Grady, K. J. & Neukirch, T. 2009, A&A, 508, 1461

Grechnev, V. V., Kiselev, V. I., Kashapova, L. K., et al. 2018, Sol. Phys., 293, 133

He, H. Q. 2021, MNRAS, 508, L1

He, H.-Q. & Wan, W. 2015, The Astrophysical Journal Supplement Series, 218, 17

He, H.-Q. & Wan, W. 2017, MNRAS, 464, 85

Heras, A. M., Sanahuja, B., Lario, D., et al. 1995, ApJ, 445, 497

Heras, A. M., Sanahuja, B., Sanderson, T. R., Marsden, R. G., & Wenzel, K. P. 1994, Journal of Geophysical Research: Space Physics, 99, 43

Hu, J., Li, G., Ao, X., Zank, G. P., & Verkhoglyadova, O. 2017, Journal of Geophysical Research: Space Physics, 122, 10,938

Hu, J., Li, G., Fu, S., Zank, G., & Ao, X. 2018, ApJ, 854, L19

Hudson, H. S. 2018, in IAU Symposium, Vol. 335, Space Weather of the Heliosphere: Processes and Forecasts, ed. C. Foullon & O. E. Malandraki, 49–53

Hutchinson, A. 2019, MPhys Dissertation, University of Central Lancashire

Hutchinson, A., Dalla, S., Laitinen, T., et al. 2022, A&A, 658, A23

Hutchinson, A., Dalla, S., Laitinen, T., & Waterfall, C. O. G. 2023a, A&A Lett, 670, L24

Hutchinson, A., Dalla, S., Laitinen, T., & Waterfall, C. O. G. 2023b, A&A, 670, A178

Jin, M., Petrosian, V., Liu, W., et al. 2018, ApJ, 867, 122

Kahler, S. W. 2016, ApJ, 819, 105

Kahler, S. W., Cliver, E. W., & Kazachenko, M. 2018, ApJ, 868, 81

Kahler, S. W. & Ling, A. G. 2018, Sol. Phys., 293, 30

Kallenrode, M.-B. 1993, J. Geophys. Res., 98, 19037

Kallenrode, M.-B. 2001, Journal of Geophysical Research: Space Physics, 106, 24989

Kallenrode, M.-B. 2002, Journal of Atmospheric and Solar-Terrestrial Physics, 64, 1973

Kallenrode, M.-B. 2003, Space Physics An Introduction to Plasmas and Particles in the Heliosphere and Magnetosphere, 3rd edn. (Springer)

Kallenrode, M.-B. & Wibberenz, G. 1997, Journal of Geophysical Research: Space Physics, 102, 22311

Kelly, J., Dalla, S., & Laitinen, T. 2012, ApJ, 750, 47

Klein, K.-L. & Dalla, S. 2017, Space Science Reviews, 212, 1107

Klein, K.-L., Tziotziou, K., Zucca, P., et al. 2018, in Solar Particle Radiation Storms Forecasting and Analysis, ed. O. E. Malandraki & N. B. Crosby, Vol. 444, 133–155

Kocharov, L., Laitinen, T., Vainio, R., et al. 2015, ApJ, 806, 80

Kong, X., Guo, F., Chen, Y., & Giacalone, J. 2019, ApJ, 883, 49

Kouloumvakos, A., Rouillard, A. P., Share, G. H., et al. 2020, ApJ, 893, 76

Laitinen, T., Kopp, A., Effenberger, F., Dalla, S., & Marsh, M. S. 2016, A&A, 591, A18

Lario, D., Aran, A., Gómez-Herrero, R., et al. 2013, ApJ, 767, 41

Lario, D., Kallenrode, M.-B., Decker, R. B., et al. 2006, ApJ, 653, 1531

Lario, D., Roelof, E. C., & Decker, R. B. 2014, in Astronomical Society of the Pacific Conference Series, Vol. 484, Outstanding Problems in Heliophysics: From Coronal Heating to the Edge of the Heliosphere, ed. Q. Hu & G. P. Zank, 98

Lario, D., Sanahuja, B., & Heras, A. M. 1998, ApJ, 509, 415

Mandzhavidze, N. & Ramaty, R. 1992, ApJ, 396, L111

Marsh, M. S., Dalla, S., Dierckxsens, M., Laitinen, T., & Crosby, N. B. 2015, Space Weather, 13, 386

Marsh, M. S., Dalla, S., Kelly, J., & Laitinen, T. 2013, ApJ, 774, 4

Mason, G. M., Li, G., Cohen, C. M. S., et al. 2012, ApJ, 761, 104

Masson, S., Démoulin, P., Dasso, S., & Klein, K. L. 2012, A&A, 538, A32

Meyer-Vernet, N. 2007, Basics of the Solar Wind (Cambridge University Press)

Miller, J. A. 1998, Space Science Reviews, 86, 79

Omodei, N., Pesce-Rollins, M., Longo, F., Allafort, A., & Krucker, S. 2018, ApJL, 865, L7

Owens, M. J., Challen, R., Methven, J., Henley, E., & Jackson, D. R. 2013, Space Weather, 11, 225

Owens, M. J. & Forsyth, R. J. 2013, Living Reviews in Solar Physics, 10

Parker, E. N. 1958, ApJ, 128, 664

Pesce-Rollins, M., Omodei, N., Petrosian, V., et al. 2015, ApJL, 805, L15

Pesce-Rollins, M., Omodei, N., Petrosian, V., & Longo, F. 2022, in 37th International Cosmic Ray Conference. 12-23 July 2021. Berlin, 34

Qin, G., Wang, Y., Zhang, M., & Dalla, S. 2013, ApJ, 766, 74

Reames, D. V. 1999, Space Science Reviews, 90, 413

Reames, D. V. 2009, The Astrophysical Journal, 706, 844

Reames, D. V., Barbier, L. M., & Ng, C. K. 1996, ApJ, 466, 473

Reames, D. V., Kahler, S. W., & Ng, C. K. 1997, ApJ, 491, 414

Richardson, I. G., von Rosenvinge, T. T., Cane, H. V., et al. 2014, Solar Physics, 289, 48

Ryan, J. M. 2000, Space Sci. Rev., 93, 581

Ryan, J. M. & Lee, M. A. 1991, ApJ, 368, 316

Ryan, J. M., Lockwood, J. A., & Debrunner, H. 2000, Space Science Reviews, 93, 35

Schatten, K. H., Wilcox, J. M., & Ness, N. F. 1969, Solar Physics, 6, 442

Seckel, D., Stanev, T., & Gaisser, T. K. 1991, ApJ, 382, 652

Seckel, D., Stanev, T., & Gaisser, T. K. 1992, in NASA Conference Publication, Vol. 3137, NASA Conference Publication, 542–549

Share, G. H., Murphy, R. J., White, S. M., et al. 2018, ApJ, 869, 182

Shea, M. A. & Smart, D. F. 2012, Space Science Reviews, 171, 161

Somov, B. & Bogachev, S. A. 2003, Astronomy Letters, 29, 621

Swalwell, B. 2018, PhD Thesis, University of Central Lancashire

Tylka, A. J. & Lee, M. A. 2006, ApJ, 646, 1319

Van Hollebeke, M. A. I., Ma Sung, L. S., & McDonald, F. B. 1975, Sol. Phys., 41, 189

Wang, Y., Qin, G., & Zhang, M. 2012, ApJ, 752, 37

Waterfall, C. O. G., Dalla, S., Laitinen, T., Hutchinson, A., & Marsh, M. 2022, ApJ, 934, 82

Wiedenbeck, M. E., Mason, G. M., Cohen, C. M. S., et al. 2013, ApJ, 762, 54

Wijsen, N., Aran, A., Pomoell, J., & Poedts, S. 2019, A&A, 622, A28

Wijsen, N., Aran, A., Scolini, C., et al. 2022, A&A, 659, A187

Winter, L. M., Bernstein, V., Omodei, N., & Pesce-Rollins, M. 2018, ApJ, 864, 39

Xie, H., St. Cyr, O. C., Mäkelä, P., & Gopalswamy, N. 2019, Journal of Geophysical Research: Space Physics, 124, 6384

Zank, G. P., Li, G., Florinski, V., et al. 2006, Journal of Geophysical Research: Space Physics, 111

Zhang, M., Qin, G., & Rassoul, H. 2009, ApJ, 692, 109

Zurbuchen, T. H. & Richardson, I. G. 2006, In-Situ Solar Wind and Magnetic Field Signatures of Interplanetary Coronal Mass Ejections (New York, NY: Springer New York), 31–43